2013

Magnetocardiography in unshielded environment based on optical magnetometry and adaptive noise cancellation

Valentina Tiporlini
Edith Cowan University

Magnetocardiography in unshielded environment based on optical magnetometry and adaptive noise cancellation

Valentina Tiporlini
Edith Cowan University, vtiporl0@our.ecu.edu.au

Edith Cowan University

Copyright Warning

Magnetocardiography in unshielded environment based on optical magnetometry and adaptive noise cancellation

By

Valentina Tiporlini

A thesis submitted in fulfilment of the requirements for the degree of

Doctor of Philosophy

at

Electron Science Research Institute
Faculty of Computing, Health and Science

EDITH COWAN UNIVERSITY

Principal Supervisor: Prof. Kamal Alameh
Principal Co-Supervisor: Prof. Di Twigg

December 2013

USE OF THESIS

The Use of Thesis statement is not included in this version of the thesis.

Declaration

Hereby I, Valentina Tiporlini, declare that the thesis “Magnetocardiography in unshielded environment based on optical magnetometry and adaptive noise cancellation” is my own original work and that all sources have been accurately reported and acknowledged, and that this document has not previously in its entirety or in part been submitted at any university in order to obtain an academic qualification.

Valentina Tiporlini December 2013

Acknowledgments

Foremost, I would like to express my sincere gratitude to my supervisor Prof. Kamal Alameh for the continuous support during my PhD journey, for his patience, motivation, enthusiasm, and immense knowledge. His guidance helped me in all the time of research and writing of this thesis.

Special thanks to Prof. Kiwoong Kim, in the Korean Research Institute of Standard and Science (KRISS), for give me the chance to visit his group and spend time in their laboratories. The time I spent in KRISS was very intense and of great benefit to my knowledge.

I would like to thank the ECU Graduate Research School for giving me an opportunity to commence my PhD study program and support me during my journey. Special thanks to the School of Nursing and Midwifery, in particular to my co-supervisor Professor Di Twigg, to accept and support me as a student.

I am indebted to all my colleagues and friends who have helped me in many ways. Special thanks to Dr. Feng Xiao who helped me to get started on the optical bench and for all the discussion and suggestion about this project. I also express my gratitude to Dr. Hoang Nguyen for great helping and discussion at the beginning of this project. Thanks are also due to Dr. Sreten Askraba and Dr. Mikhail Vasiliev for the many suggestions and pleasant chats through which I learned a lot both professionally and personally. I would like also to thank Dr. Arie Paap, Dr. Baofu Ding and Mr. Devendra Maury for great help, discussion and jokes.

The most special thanks goes to my friends and roommates, David, Yamna, Ramzi, Ali, Nur, Nazmi, Samarth, Praveen, Paul, with whom I shared hard work, concerns and successes. I will never forget the conversations, confidences and laughter shared with my partner desk Kavitha, with whom I have built a friendship that will last for life. I will be forever grateful to my friend Ayman for having listened to my outbursts and always encouraged me not to give up. I am very happy and fortunate to have shared the PhD journey from the very beginning

with Haithem; we shared many misadventures but also many successes and I am proud to have reached the finish line with him.

My sincere thanks to Mrs. Linda Arthur, Mrs. Beverley McKinnon, Mrs. Tiella Turkovic & Mr. Paul Roach for all their administrative support and help rendered to me, especially to Linda and Paul for editing my thesis.

I warmly thank my parents, my brother and my sister in law, for their encouragement and continued support throughout my studies. I would like to express my sincere gratitude to my aunt, my uncle and my beautiful cousins who welcomed me on my arrival in Australia and always made me feel the warmth of a family.

I lovingly express thanks to my partner Alessandro for being a constant source of support and encouragement during this PhD journey and to my gorgeous stepson Cristian for all the happiness he brought into my life.

« "O frati," dissi, "che per cento milia
perigli siete giunti a l'occidente,
a questa tanto picciola vigilia

d'i nostri sensi ch'è del rimanente
non vogliate negar l'esperïenza,
di retro al sol, del mondo sanza gente.

Considerate la vostra semenza:
fatti non foste a viver come bruti,
ma per seguir virtute e canoscenza". »

Dante Alighieri, "La Divina Commedia"
"Inferno", canto XXVI, vv 112-120

Abstract

This thesis proposes and demonstrates the concept of a magnetocardiographic system employing an array of optically-pumped quantum magnetometers and an adaptive noise cancellation for heart magnetic field measurement within a magnetically-unshielded environment.

Optically-pumped quantum magnetometers are based on the use of the atomic-spin-dependent optical properties of an atomic medium. An Mx-configuration-based optically-pumped quantum magnetometer employing two sensing cells containing caesium vapour is theoretically described and experimentally developed, and the dependence of its sensitivity and frequency bandwidth upon the light power and the alkali vapour temperature is experimentally demonstrated. Furthermore, the capability of the developed magnetometer of measuring very weak magnetic fields is experimentally demonstrated in a magnetically-unshielded environment

The adaptive noise canceller is based on standard Least-Mean-Squares (LMS) algorithms and on two heuristic optimization techniques, namely, Genetic Algorithms (GA) and Particle Swarm Optimization (PSO). The use of these algorithms is investigated for suppressing the power line generated 50Hz interference and recovering of the weak magnetic heart signals from a much higher electromagnetic environmental noise. Experimental results show that all the algorithms can extract a weak heart signal from a much-stronger magnetic noise, detect the P, QRS, and T heart features and highly suppress the common power line noise component at 50 Hz. Moreover, adaptive noise cancellation based on heuristic algorithms is shown to be more efficient than adaptive noise canceller based on standard or normalised LMS algorithm in heart features detection.

Contents

List of figure

Chapter 1

Magnetocardiography Significance

In this chapter we introduce the existing techniques for heart activity monitoring, focusing on their advantages and disadvantages and we give a brief overview of the anatomy and the electrophysiology of a human heart. The motivation and significance of this PhD project are then discussed and the chapter ends with the description of the layout of this thesis.

1.1 Historical background

The act of monitoring heart sounds for diagnostic purposes has its origin in historical times. The first description of cardiac sounds was provided by Hippocrates (between the 5th and the 4th century BC) who used to listen to the heart sounds by the direct application of the ear to the patient's chest and abdomen [1]. This process, known as immediate auscultation was practiced until the 19th century when in 1816 Rene Theophile Hyacinthe Laënnec, a French physician, invented an instrument, named a stethoscope (from the Greek words stethos, meaning chest, and skopein, meaning to explore), to be interposed between the ear of the examiner and the body of the patient [2]. This technique is called mediate auscultation and is still used by medical practitioners to listen to the heart sounds. In 1834 James Hope first hypothesized that the heart sounds were caused by the mechanical opening and closing of the cardiac valves [3]; while in 1835 C.J.B. Williams associated the origin of the heart sounds to the cardiac muscle contraction and to the mass of blood which moves inside the heart chambers [4]. This mechanical energy can also be detected indirectly by utilizing the concept of Doppler ultrasound effect. The first Doppler device for monitoring heart sounds was described by Hertz and Edler in 1954 [5].

The first to associate an electric force to the heart activity was Augustus Waller in 1887 [6]. However, the first accurate electrocardiographic recording was made in 1902 by William Einthoven using a string galvanometer [7]. Einthoven is considered to be the inventor of the electrocardiography and he named the different heart features with the letters P, Q, R, S and T [8], a discovery for which he won the Nobel prize in 1924 [9]. At present, electrocardiography is widely used as a diagnostic tool for cardiac dysfunction [10] and is also used for long time monitoring of cardiac activity (holter) [11].

A magnetocardiographic signal was recorded for the first time in 1963 by Bauble and McFee [12], who measured the heart's magnetic field using induction coils and reported a peak with intensity of 100pT at the chest's surface [13], one million times weaker than the geomagnetic field. This result was confirmed in 1967 by Safonov et al. using the same technique as Baule and McFee with the addition of a magnetically shielded chamber to suppress environmental

electromagnetic noise [14]. The first to use Superconducting Quantum Interference Device (SQUID) magnetometers to detect the cardiac magnetic signal was Cohen et al. in 1970 [15]. To date, SQUID magnetometers have the highest reported sensitivity [16, 17], and they are the sensors most widely used in magnetocardiography [18-23] and foetal magnetocardiography [24-26]. Magnetocardiography based on an optical pumped magnetometer, employing a discharge-lamp as the light source, was demonstrated in 1981 by Livanov et al. [27], but optical magnetometry has not been utilised in magnetocardiography for many years. Recently, optical magnetometers have demonstrated sensitivities as high as those of SQUID [28] and are becoming popular for magnetocardiography [29, 30]. Furthermore, SQUID magnetometers must be operated at very low temperatures, thus requiring expensive and cumbersome cooling mechanisms. Conversely, optical magnetometers not only work at room temperature but also have the potential for miniaturization, making them more practical for many applications [31, 32].

1.2 Capability and limitations of techniques for heart activity monitoring

A cardiac muscle generates both a mechanical energy and an electrical energy in relation to its pumping activity. As shown in Fig.1.1, the heart-generated mechanical energy can be measured by means of auscultation or using ultrasound. Electrical energy can also be measured by electrocardiography, by detecting the potential difference trough electrodes placed on the surface of the human body, or by magnetocardiography, which senses the magnetic field that surrounds the human body.

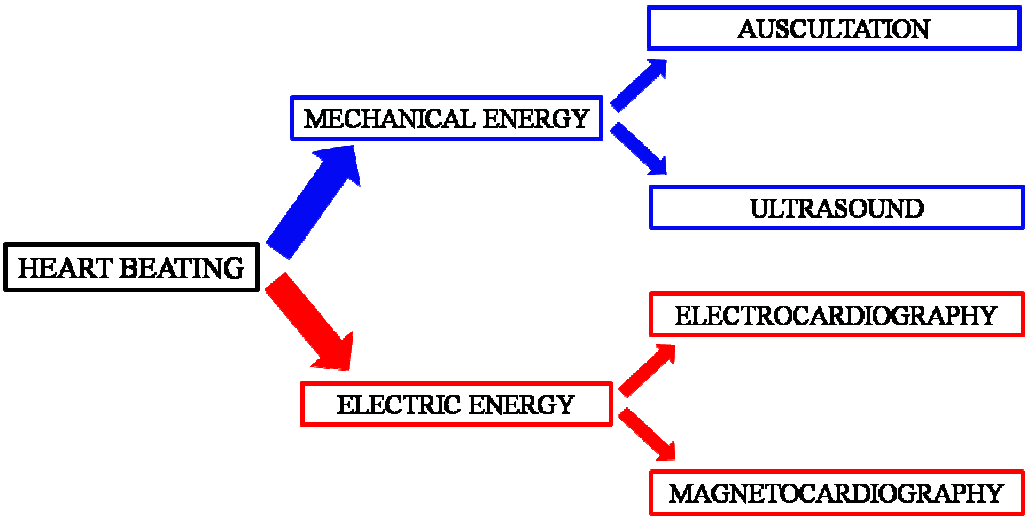

Fig.1.1: Synthesizing of energies produced by the activity of the heart together with the related sensing techniques.

The main limitation of mediate auscultation and ultrasound is that they are operator-dependent, i.e., a high level of skill and experience is needed to acquire good-quality data and make accurate diagnoses. This is particularly the case for mediate auscultation which does not release a trace or a record of heart activity. Furthermore, these techniques are not suitable for observation over an extended period, such as over night.

Electrocardiography is completely harmless and non-invasive, requires lower power, can be used over extended periods and has the advantage of being portable. In order to capture the heart's electrical signals, electrodes are placed on the human body and the detected signals are affected solely by the electric currents which flow through body tissue. These currents are affected by local inhomogeneities due to discontinuities of the electric conductivity in body tissue, such as fat layers or bones which act as spatial low-pass filters. Furthermore, the results from this technique are adversely affected by skin-electrode contact, including: (i) dependence upon the position of the electrodes, (ii) electrode contact noise due to loss of adherence between the electrode and the skin, (iii) motion artefacts caused by the skin and electrode interface and electrode cable and (iv) it is not suitable for patients with damaged skin, such as acute burns. Techniques based on magnetic fields measurements offer a simple non-invasive and risk-free

method for the acquisition of a cardiac waveform without any physical contact between the patient and the instrument, and so avoiding problems caused by skin-electrode contact.

The main limitation of magnetocardiography is due to the environmental electromagnetic noise, which is composed essentially of two parts: a constant component caused by the geomagnetic field and a variable field that depends on particular sources, such as power lines, electronic instruments and wireless devices. The geomagnetic field is stable and has an intensity variable of between 25 to 70 μT [33] depending on the geographic location. The magnetic field generated by a human adult heart has a peak intensity of 100pT, one million times less than the earth's magnetic field, and the magnetic field generated by a foetal heart is even weaker, about 1pT to 10pT resulting in a very poor signal to noise ratio which can be increased by improving the sensitivity of the magnetometer or by reduction of noise that can be obtained by means of shielding, or applying noise cancellation techniques based on signal processing.

Electrocardiography and magnetocardiography have been compared in many studies highlighting their capabilities and their limitations [34, 35]. Magnetocardiography has been demonstrated to be more efficient than electrocardiography in the diagnosis of certain cardiac pathology, such as acute coronary syndrome [36]. Also, magnetocardiography has been shown to be more accurate than electrocardiography for the (i) diagnosis of atrial and ventricular hypertrophy, (ii) non-invasive location of the heart's conduction pathways, (iii) the identification of spatial current dispersion patterns, and (iv) the detection of circular vortex currents which do not provide any ECG signals [37].

1.3 Problem formulation

A brief overview of cardiac anatomy and electrophysiology is described to better understand the nature of magnetic signals to be measured.

1.3.1 Heart anatomy

A human heart, as showed in Fig.1.2, is composed of four chambers: the upper two are the right and left atria and they contract at the same time; the lower two chambers are the right and left ventricles that are also synchronized.

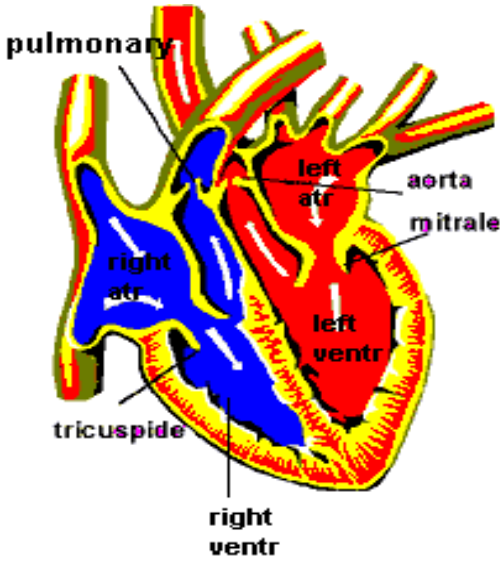

Fig.1.2: Human heart.

The right atrium receives the venous blood from the vena cava and pushes it into the right ventricle. The blood is then driven into the pulmonary arteries to reach the lungs where it is oxygenated and then returned into the heart through the left atrium where it is pumped into the left ventricle and then into the aorta that transports it around the body.

1.3.2 Electrophysiology of the heart

The cardiac muscle is characterized by a high number of individual cells with a diameter of 15µm and a length of 100µm [38]. Two adjacent cells are interconnected by a gap junction composed by an intercalated disk that has a particular structure containing proteins that allow ions to move between cells. Thanks to the electric connections granted from the junction gap, all cardiac cells work together as a unique large cell. As shown in Fig.1.3, each cell consists of a membrane that separates the inner volume from the external intercellular liquid.

This membrane is not permeable to charged ions so the inside of the cell remains at a negative potential with respect to the outside, therefore it can be treated like a biological battery [39] with a transmembrane potential, Vm that for a resting cell is about -70mV. Nevertheless, the membrane contains special gating proteins that under particular conditions, i.e., after a mechanical or electrical stimulus, create ion channels to allow an ion flux through the membrane. At rest, both inside and outside the cell, the electric fields are null whereas within the membrane the electric fields from the negative charge on the inner surface and the positive charge on the outer surface produce an electric field of approximately 10^6volts/meter.

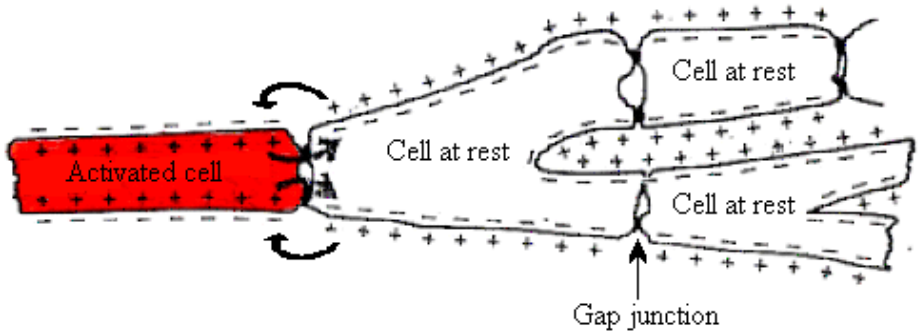

Fig.1.3: Cardiac cell.

When the cell is electrically stimulated there is a conformational change into gating proteins that creates an axial channel that allows certain ions to pass through the protein and so through the membrane. The transmembrane potential Vm increases till it reach positive values. That region of the cell is then termed depolarized.

A resting membrane of cardiac cells is highly permeable to K ions, therefore to maintain the electric balance the cell must spend energy to operate a sodium-potassium pump that ensures a large negative resting potential keeping the intracellular concentration high for K ions and low for Na ions. Normally, each Na-K pump exports three ions of sodium and imports two ions of potassium [40]; so there is a higher concentration of positive charged ions that constitutes an outward current. This flow of Na ions is equivalent in size to one third of the time

average of the inward Na currents associated with the electrical activity of the heart, so this pump current influences the electric activity of cells. The cardiac action potential is generated by Na, K, Cl ionic currents flowing across the cardiac cell membrane via their own channels. The sodium-potassium pump exerts a direct influence on the electrical activity of cardiac cells via its generation of a significant component of membrane current and an indirect influence through its control of the intracellular concentrations of Na and K ions [39]. For the heart to pump effectively, all contractions of the four cardiac chambers must be well synchronized. The working cycle of the heart is controlled by an electrical signal generated from a group of special cells called sinoatrial nodes, placed close to the vena cava's entrance, as shown in Fig.1.4. This signal is spontaneously generated.

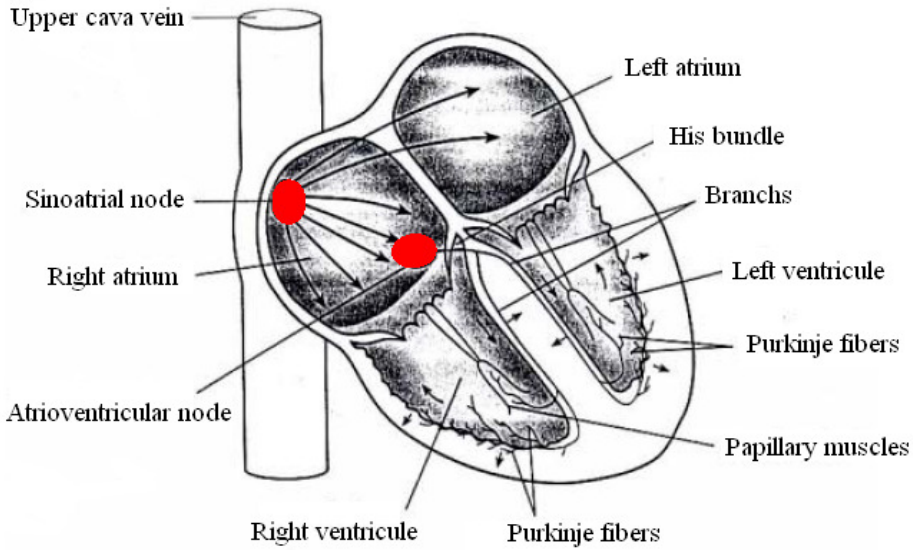

Fig.1.4: Electrical activity of the heart.

The electrical signal generated from the sinoatrial node causes the depolarization of nerves into the atria that consequently contract and pump blood into ventricles. Afterwards, the signal reaches the atrioventricular node and from there it travels along the His bundle to depolarize and contract the ventricles that send blood into the pulmonary arteries and into the aorta respectively. After the contractions, atria and ventricles repolarise and the cycle starts again.

Fig.1.5 shows the signal that represents a cardiac cycle.

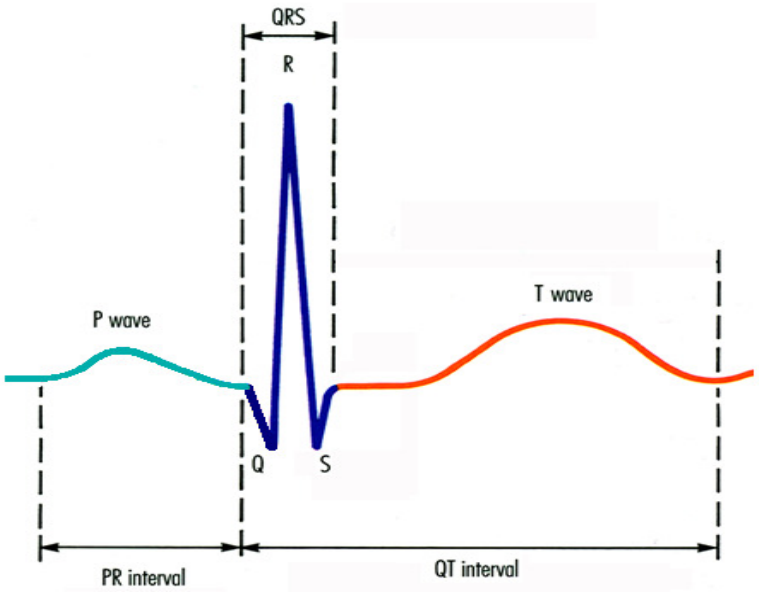

Fig.1.5: Typical heart waveform showing the P wave, QRS complex and T wave, which correspond to atrial depolarization, ventricular depolarization and ventricular repolarization, respectively.

This wave can be divided into three distinct areas: the P wave that corresponds to atria depolarization; the QRS complex that represents the ventricles depolarization; the T wave that coincides with ventricles repolarization. The atria repolarization occurs during ventricle depolarization so it is not visible on the signal because the QRS complex overlaps it. The R-R interval leads to the heartbeat frequency that gives useful information for the heart conditions. Electrocardiograms and magnetocardiograms have the same basic shape because they are generated by the same electrophysiological processes.

1.4 Objectives of the thesis

The principal aim of this thesis is to design, develop and experimentally demonstrate a magnetocardiographic system, which is cost-effective, movable, contact-free, totally harmless, does not require an expert to operate and can work in electromagnetically noisy environments, such as hospitals or laboratories. The novelty of employing an array of optical magnetometers in conjunction with an adaptive noise canceller will allow the magnetocardiographic system to be

operated in magnetically unshielded environments. This goal can be translated into discrete objectives:

- Design and develop an optical magnetometer;
- Maximize the magnetometer sensitivity by the optimization of several parameters, including: temperature dependent gas pressure, light power intensity and uniform magnetic field strength.
- Investigate the dependence of the frequency bandwidth of the magnetometer from above mentioned parameters.
- Develop a two dimensional array of sensitivity-optimized optical magnetometers.
- Implement an adaptive noise cancellation system employing several algorithms including: Least Mean Squared (LMS) algorithm, normalised LMS algorithm, and two heuristic optimization methods (namely: (i) Genetic Algorithms (GA) and (ii) Particle Swarm Optimization (PSO)).
- Demonstrate the proof of concept of the magnetocardiographic system for recovering a weak magnetic heart signal, with clear identification of the QRS complex, from a much stronger environmental electromagnetic noise.

1.5 The significance of the thesis

Telehealth is a health care program where the patient and the medical practitioner are in different geographic locations. The undeniably important application of Telehealth is when a continuous monitoring of specific parameters (health indicators) is needed, such as for chronic disease that can be only controlled but not cured. Recently, Telehealth has become part of the research and development in social healthcare systems. Particularly in Australia, where many people live in rural areas far away from any medical centres or hospitals, it is difficult for people with chronic disease to access centres for periodical checks. As discussed above, magnetocardiography provides better performance with respect to electrocardiography because it is contact free and is not affected by differences in the conductivity of human tissue. In order to be used in Telehealth

systems any magnetocardiographic system must be portable, which means they must be suitable to work in a magnetically unshielded environment.

This PhD research project experimentally demonstrates magnetocardiography based on optical magnetometry and employing an adaptive noise cancellation system and operating in a magnetically unshielded environment. The presented results signify a step forward in the achievement of a portable magnetocardiographic system.

The contributions of this study also include:

- Development and characterization of a high sensitivity optically-pumped quantum magnetometer.
- Experimental demonstration of a weak magnetic heart field, differentiated from a much higher noise by means of adaptive noise cancellation.
- Novel application of adaptive noise cancellation based on heuristic optimization techniques in the case of very low signal-to-noise ratio.

1.6 Layout of the thesis

This thesis consists of 7 chapters. The first introductory chapter reviews the techniques for heart activity monitoring, presents an overview on heart anatomy and electrophysiology and discusses the motivation for undertaking the research project.

Chapter 2 gives a general description of optical magnetometry principles and introduces the different modes of operation of optical magnetometers with a comparison of their sensitivity and their possible applications. The problem of noise is also covered in this chapter and an overview of the noise suppression techniques used in magnetocardiography is presented.

A thorough explanation of the theory behind the optical magnetometer is given in Chapter 3. This includes: (i) the description of the atomic structure of the alkali metals, focused on caesium; (ii) the analysis of the optical pumping process with the introduction of dark states and (iii) the effect of a radiofrequency radiation on atoms in dark states. Bloch equations, which describe the behaviour of the magnetization vector produced by the magnetic field inside the caesium gas

cell, are then examined. Finally, the parameters that affect the final sensitivity and frequency bandwidth of the instrument are analysed and discussed.

In Chapter 4, the operation principle of an adaptive noise cancellation system is described, together with the algorithms used to adaptively update the noise canceller filter coefficients. Those algorithms can be divided in to two classes: Least-Mean Squares (LMS) based algorithms and heuristic optimization techniques, which include genetic algorithms (GA) and particle swarm optimization (PSO). At the end of the chapter, the advantages and the disadvantages of the different techniques are discussed.

Chapter 5 describes in detail the experimental setting of the developed optically-pumped quantum magnetometer. This chapter also includes the results of the optimization process of the sensitivity and the frequency bandwidth of the instrument in respect of the significant parameters outlined in Chapter 3.

Chapter 6 shows the experimental results obtained employing an array configuration of the optical magnetometer optimized in Chapter 5, in combination with the adaptive noise cancellation system, which adopts each of the techniques described in Chapter 4. The experimental results for the various adaptive algorithms are compared with each other and with previous simulations results.

Finally, a comprehensive conclusion and recommendation for future work is presented in Chapter 7, discussing possible applications of the developed instrument and future research directions.

Chapter 2

Optical Magnetometry and Unshielded Magnetocardiography

In this chapter, we explain the general principle of optical magnetometry and describe the different operational modes of optical magnetometers, focusing on the sensitivity that they can achieve and their potential applications. We also introduce the problem of electromagnetic environmental noise and we report on noise suppression techniques which are used in magnetocardiography.

2.1 Optical magnetometry

When an atom interacts with a magnetic field, the magnetic field exerts a magnetic torque on the atom's total angular momentum causing it to precess around the field's axis at an angular frequency, known as Larmor frequency, which is proportional to the field's magnitude: $w_L = \gamma|B|$, where γ is the gyromagnetic constant. This precession is schematically illustrated in Fig.2.1.

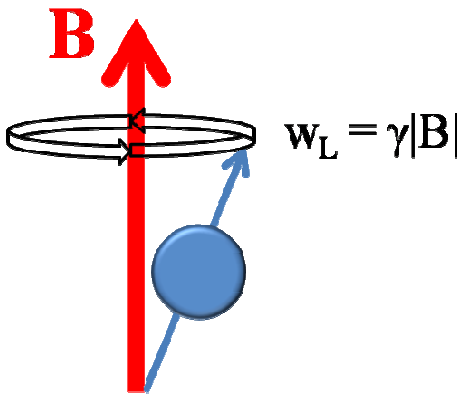

Fig.2.1: Precession of the atomic total angular momentum along the axis of an external magnetic field at the Larmor frequency w_L.

Optically-pumped atomic magnetometers aim to indirectly measure the magnetic field by directly measuring the Larmor frequency, using the atomic-spin-dependent optical properties of a medium. The general principle of operation of optically-pumped atomic magnetometers has been described in detail by Budker and Romalis [41]. A laser light, which is tuned to a frequency resonant with an optical transition and transmitted through an atomic medium, creates along-lived orientation and/or higher order moments in the atomic ground state. The atomic total angular momentum subsequently undergoes Larmor spin precession around the magnetic field modifying the optical absorptive and dispersive properties of the atoms. Those changes can be detected by measuring the intensity or the polarization of the transmitted light.

The optical magnetometry principle has been used in the development of sensitive optical magnetometers during the second half of the 19th Century. Dehmelt has demonstrated a high-frequency modulation of a light beam

transmitted through atoms precessing into a magnetic field [42, 43] referring to the description of the behaviour of a momentum vector interacting with an external magnetic field made by Bloch [44, 45]. The first highly sensitive optical magnetometer, based on Dehmelt studies, was made by Bloom and Bell [46-48]. Since then, optical magnetometers have experienced a large expansion triggered by technological development of the laser light source.

At present optical magnetometers achieve sensitivity comparable with magnetometers using SQUID technology [49-51], and they are being used in many applications, including magnetocardiography.

2.2 Mode of operation of optical magnetometers

The basic operation mode of optical magnetometers involves the following mechanisms: Coherent Population Trapping (CPT), Nonlinear-Magneto-Optical rotation (NMOR), Spin-Exchange Relaxation Free (SERF) regime, and Mx magnetometer, which will be explained in the subsequent sections.

2.2.1 Coherent Population Trapping (CPT)

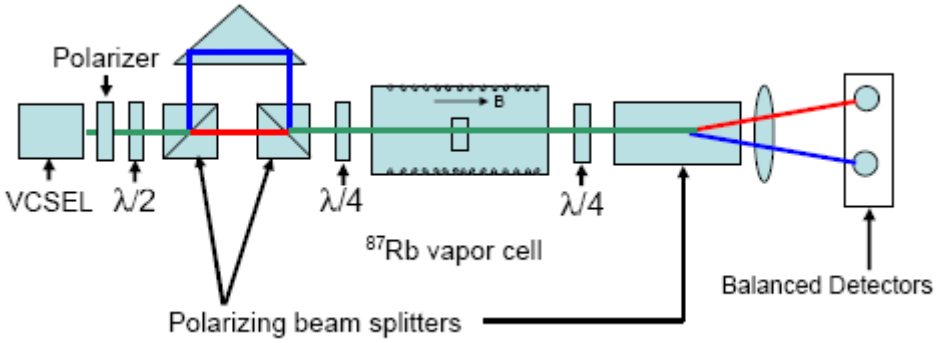

Fig.2.2: CPT example reported in [52].

The CPT method, illustrated in Fig.2.2, is an all-optical technique involving two light sources with orthogonal polarizations that create a coupling between two Zeeman sublevels located in different hyperfine states (more details on Zeeman sublevel splitting will be presented in Chapter 3). A 795 nm VCSEL (laser) is modulated at around 1.7 GHz and the resulting optical side bands induce quantum

interference in ^{87}Rb atoms mixed with nitrogen gas. An imbalance in the orthogonal circular polarization component is introduced by passing the RF-modulated VCSEL beam through a polarizing beam splitter (PBS) followed by a quarter wave plate. For a magnetic field along and transverse to the VCSEL propagation direction, the transmission and polarization rotation of the output VCSEL beam is monitored with the help of the PBS and two balanced photo detectors. When the modulation of the probing light is in resonance with the Zeeman splitting frequency ground sublevels, a decrement in the light intensity can be observed. The direct measurement of the Larmor frequency gives an absolute value for the modulus of the magnetic field, i.e., the magnetometer works in a scalar mode.

CPT based devices present considerable benefits, i.e., a decrease in size, power reduction and cost effectiveness. They are typically used in atomic clocks [53, 54] and magnetometers [55-57]. The application of CPT based magnetometers for cardiosignal detection, with a sensitivity of $1pT/\sqrt{Hz}$ into an unshielded environment, is demonstrated in [58].

2.2.2 Nonlinear-Magneto-Optical rotation (NMOR)

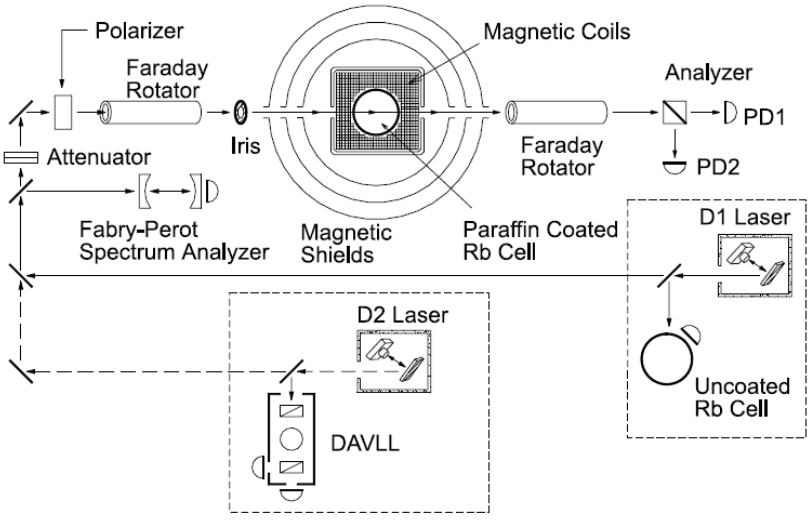

Fig.2.3: NMOR block diagram reported in [59].

Nonlinear-Magneto-Optical rotation (NMOR) is based on the linear magneto-optical (Faraday) rotation principle, where the polarization plane of a linearly polarized light, is propagated through a medium immersed in a magnetic field, undergoes a rotation at the output. Fig.2.3 shows a block diagram for a NMOR-based system. Tunable lasers are used to generate an optical beam at 795 nm for the rubidium D1 line ($^2S_{1=2} \rightarrow {}^2P_{1=2}$) and 780 nm for the rubidium D2 line ($^2S_{1=2} \rightarrow {}^2P_{3=2}$). The frequency of the D1 laser is monitored by observing fluorescence from another uncoated Rb vapour cell and the signal from a cofocal Fabry-Perot spectrum analyser. The frequency of the D2 laser is monitored by observing the signals from the Fabry-Perot cavity and a DAVLL (diachronic atomic vapour laser lock). The four-layer magnetic shield suppresses the external dc magnetic fields. Residual magnetic fields are compensated by three mutually perpendicular Helmholtz coils. Modulation polarimetry is used to detect the NMOR signals. After transmission through the coated Rb vapour cell, the laser beam passes through a second Faraday rotator that rotates its polarization, which is monitored by a polarizing beam splitter. The first harmonic of the signal detected by photodiode PD1 is measured using a lock-in amplifier. The ratio of the first harmonic signal from PD1 to the transmitted light intensity (sum of light detected photodiodes PD2 and PD1) is a measure of the optical rotation angle.

Note that Faraday rotation is independent of the light intensity, however the light modifies the properties of the Rb medium, causing nonlinear Faraday rotation when the light frequency is at resonance with the atomic transitions of the medium, thus allowing optical pumping to take place. In this case, two light-atoms interactions occur, one to pump the atomic sample and the other to probe it. The dynamic range of an NMOR-based magnetometer is limited by the linewidth of the NMOR. While a magnetic field modulates the optical properties of a medium at a frequency of $2w_L$ (where w_L is the Larmor frequency) the dynamic range can be increased by modulating the light at the same frequency. The sensitivity that can be obtained with this operation mode is around $0{,}15 pT/\sqrt{Hz}$ [60] and it is suitable for geomagnetic measurements but it needs to be improved to be applied to biomagnetic signal measurements.

2.2.3 Spin-Exchange Relaxation Free (SERF) regime

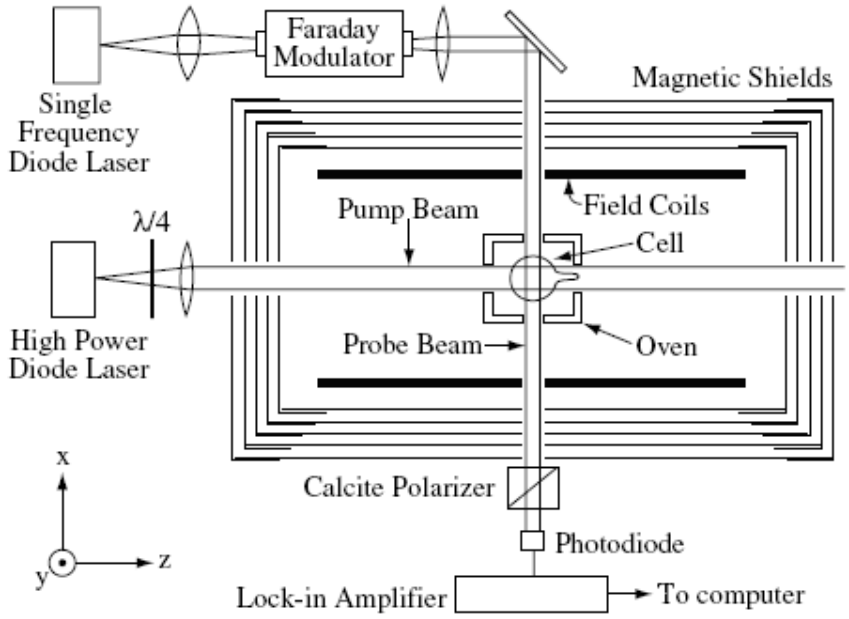

Fig.2.4: SERF block diagram reported in [61].

Fig.2.4 shows a typical Spin-Exchange Relaxation Free (SERF) magnetometer that comprises a vapour cell containing potassium and a buffer gas. A pump laser is used to spin-polarise the unpaired electrons of the potassium atoms, while a perpendicular probe laser is used to detect the precession of the electron spin when an external magnetic field is applied. The electrons of potassium vapour, which is synthesised by heating a potassium droplet inside a glass cell, absorb a circularly polarized laser light, spinning the electrons along the direction of the circular polarization of the light. A laser is used to detect the orientation of the electron spins while precessing. By detuning the laser frequency with respect to the potassium resonance, and as a result of the circular dichroism of the vapour, the laser polarization angle rotates by an angle proportional to the electron precessing angle (or signal magnetic field). This configuration suppresses spin-exchange relaxation as the spin-exchange collisions is fast as the spins do not have enough time to precess and loose coherence between collisions.

Magnetometers operating in the SERF regime are typically based on the NMOR principle. The limitation in sensitivity is due to depolarization which is

due to atoms' interaction. The dominant type of these interactions is the spin-exchange collisions that can change the hyperfine state of the atoms while preserving total angular momentum of the colliding pair. The result is a decoherent precession of the atom ensemble in the presence of a magnetic field that does not allow the detection of the Larmor frequency. However, decoherence due to spin-exchange collisions can be completely eliminated if the spin-exchange collisions occur much faster than the precession frequency of the atoms. This optical magnetometer mode of operation can reach a sensitivity of $0.54 fT/\sqrt{Hz}$ [51] and is used extensively in magnetocardiography [62].

2.2.4 Mx magnetometer

The generic configuration of an optical Mx magnetometer is shown in Fig.2.5 (a). Mx magnetometers are so called because an oscillating magnetic field is supplied to the vapour atoms to modulate the x component of the magnetization inside the vapour cell. The core of the system is a glass cell filled with the vapour of one of the alkali metals that have only one electron in their outermost shell. Generally, caesium is used because it possesses only one stable isotope, ^{133}Cs, with a nuclear spin I = 7/2.

When a uniform dc external magnetic field is applied, each hyperfine level of caesium atoms splits into 2F+1 Zeeman sublevels, as displayed in Fig.2.5 (b). The light source is used both for pumping the Cs atoms to excited states and as a probe signal. Photons having a wavelength equal to the first absorption line of the alkali atoms are absorbed by the caesium atoms, thus moving them to the excited state. Fig.2.5 (b) shows the optical pumping over the $F = 4 \rightarrow F' = 3$ transition of the caesium D1 absorption line using right circularly polarized light, which results in photon's angular momentum equal to +1. A Cs atom in the lower state with a quantum number m_F is allowed to move only to the upper level with $m'_F = m_F + 1$ because of total angular momentum conservation. A Cs atom that is in the excited state can decay via one of three possible decay channels and it spontaneously emits a photon that has equal probability to be sent in any direction, not necessary the direction of light beam. Therefore, there is a finite probability for the atom to decay into a level with a larger m_F value; thus, if the pumping process is repeated

several times the atom moves to the two outermost states (m_F = 3 and 4) and, eventually, can no longer be optically pumped because there is not a corresponding state in the excited level available for transition [58]. Since these atoms do not absorb light, they are called dark states.

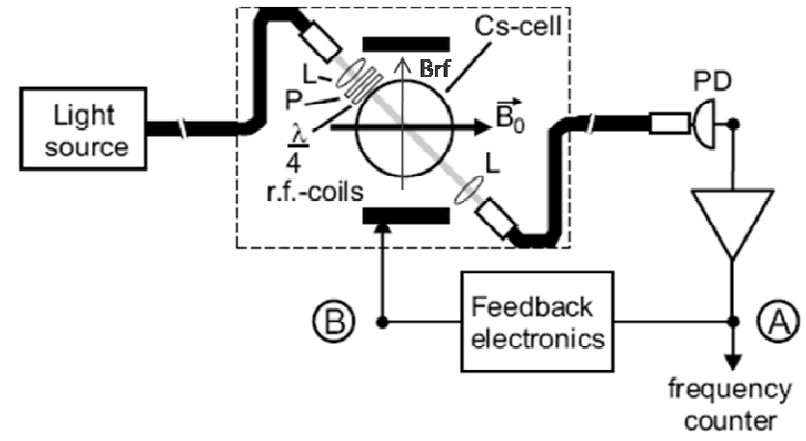

(a)

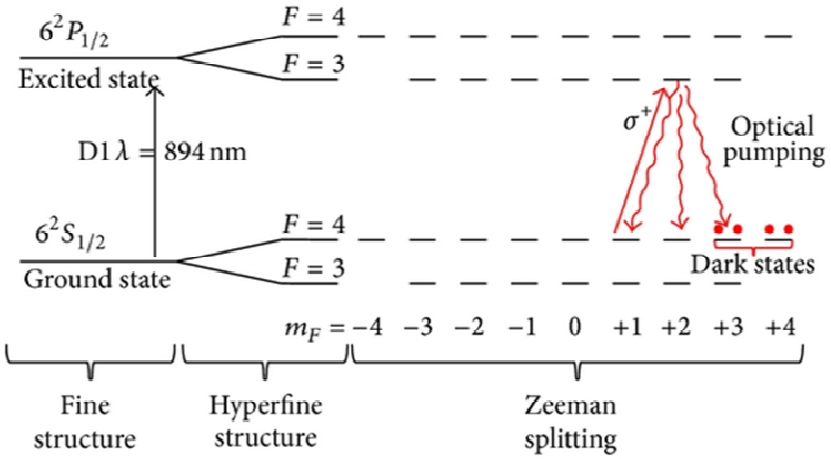

(b)

Fig.2.5: (a) Schematic of a Mx magnetometer reported in [63]. *(b) Fine, hyperfine structures and Zeeman splitting of the caesium D1 line with the optical pumping process and the dark states highlighted.*

The Cs atoms in the dark states precess around the magnetic field axis at the Larmor frequency that is proportional to the field magnitude: $w_L = \gamma | B_0|$, where γ is the gyromagnetic constant; that for caesium is 2 $\pi\times$ 3.5 Hz/nT. During this

time, the atom spin accumulates an increasing phase angle. The spin state of an atom can be changed to an absorbing (non dark) state through the absorption of resonant radio frequency radiation (w_{rf}). The phase difference between this rf signal and the frequency of the probing light gives a direct measurement of the Larmor frequency. This kind of magnetometer can reach sensitivity of $63 fT / \sqrt{Hz}$ [28] and is widely used in magnetocardiography [30].

2.2.5 Capability and limitations of the modes of operation of optical magnetometers

Magnetometers based on CPT and on SERF regime work in zero magnetic field conditions while NMOR and Mx configurations require a weak magnetic field to generate Zeeman splitting. Throughout all the operation modes described above, only the Mx configuration and SERF regime have sensitivity high enough to capture the magnetic field generated by a foetal heart. An attractive feature of magnetometers working in the SERF regime over the Mx configuration is that they do not need an rf magnetic field or magnetic coils in the proximity of the vapour cell; this can create crosstalk problems in array configurations. On the other hand, the SERF regime requires very high temperatures to assure high sensitivity, and only works in very weak magnetic fields because the frequency of collisions must be higher than the Larmor frequency; this makes the SERF regime much more susceptible to environmental noise.

2.3 Environmental electromagnetic noise

The environmental magnetic noise is composed essentially of two parts: a constant component caused by the geomagnetic field and a variable field that depends on particular sources, such as power lines, electronic instruments and wireless devices.

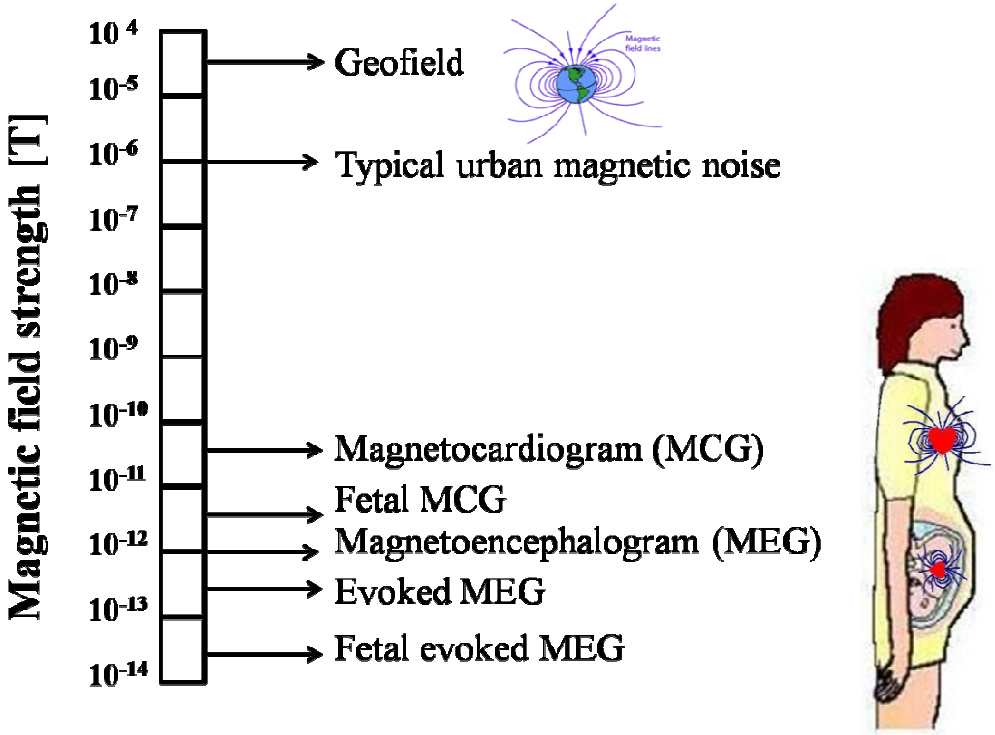

Fig.2.6: Typical strength of bio- magnetic fields and electromagnetic noise.

The geomagnetic field is stable and typically has an intensity between 25 to 70 μT [33] depending on the geographic location. The magnetic field generated by a human adult heart has a peak intensity of 100 pT, one million times less than the earth's magnetic field, and the magnetic field generated by a foetal heart is even weaker, about 1pT to 10 pT, as shown in Fig.2.6. The resulting signal-to-noise ratio is very low and can be increased by improving the sensitivity of the magnetometer or by a noise reduction, which can be obtained by means of shielding, or applying noise cancellation techniques based on signal processing.

There are two shielding techniques to attenuate the surrounding magnetic noise, as illustrated in Fig.2.7, namely, passive shielding, which consists of the use of a shielding room, and active shielding, which is based on the principle that the disturbing magnetic field can be reduced by superimposing other magnetic fields having the same magnitude but with opposite orientation.

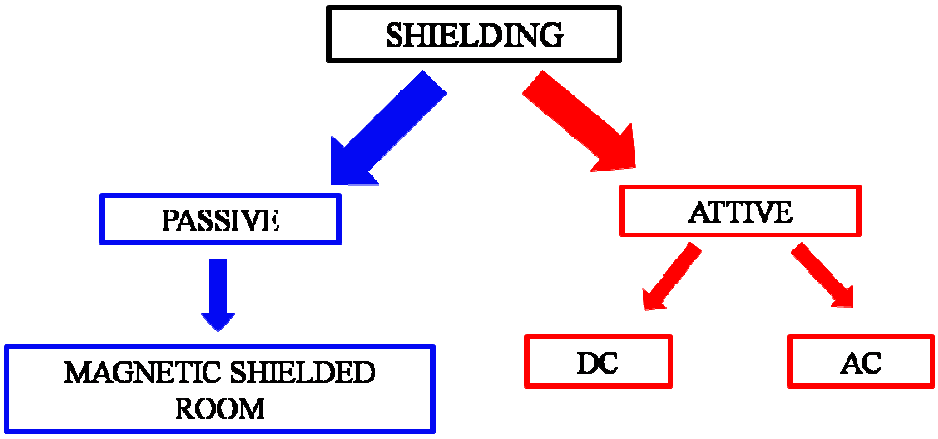

Fig.2.7: Electromagnetic noise shielding techniques.

The use of a shielded room assures the cancellation of both DC and AC components of magnetic noise [64-66], while the active shielding techniques must be divided into DC noise cancellation and AC noise cancellation. The DC compensation is achieved by using DC excited coils surrounding the workspace. The AC compensation, instead, requires the detection of the disturbing magnetic field, a feedback loop and a compensation coil system [67, 68]. Magnetocardiographic systems working inside a shielded room have been largely demonstrated [69, 70]. For example, the research group at the University of Fribourg in Switzerland [71] recently developed a cardiomagnetometer combining the use of a magnetically-shielded room with a second order gradiometer configuration. The passive shielding attenuates both the geomagnetic field and the oscillating magnetic fields of the environment, while the second order gradiometer, driven by a digitally controlled feedback loop, allows for the compensation of the linear vertical field gradient and fluctuations of the uniform field that generate the magnetization inside the vapour cell. The problem with the system is crosstalk between adjacent sensors in the array system, which marginally affects measurements.

2.4 Magnetocardiographic systems operating in a magnetically-unshielded environment

Magnetically-shielded rooms are expensive to install and maintain; and are heavy and uncomfortable for the patients. Hence, systems working in unshielded environments have advantages in terms of cost, flexibility and comfort. Several studies have been conducted on the possibility of effecting an MCG measurement outside shielded rooms, in a noisy environment. Different techniques have been used to suppress the noise. Aarnink et al. [72] have used a multichannel SQUID-based magnetometer adopting two different active noise compensation techniques to successfully record magnetocardiograms in an ordinary environment; but these techniques create constraints in the sensor array spatial arrangement and are less effective in cancelling nearby sources of noise. More studies have also been successfully carried out on the use of active magnetic shielding for unshielded MCG [73-75]; however more improvements are still needed to make these system practical.

A 36-channels system based on SQUID magnetometers working in an unshielded environment has been developed by a research group at the Catholic University in Rome, Italy. They have particularly demonstrated: (i) the ability of the system to perform 3-D cardiac source localization; (ii) the consistency of the instrument for the study of patients affected by coronary artery disease [76, 77]; (iii) a higher accuracy in respect of electrocardiography for the classification of ventricular pre-excitation [78]; (iv) the possibility of detection of atrial and ventricular magnetic fields in live animals, with a weight of about 250 grams [79]; and (v) the feasibility of unshielded mapping of foetal magnetocardiogram, after the 32^{nd} gestational week, of a quality comparable to measurements taken inside the shielded room [26, 80].

Magnetocardiographic systems working in magnetically-unshielded environments are mainly based on SQUID magnetometers [81-84]; however, some optical-magnetometry-based magnetocardiographs have been demonstrated, which operate in an electromagnetically noisy environment. A SERF atomic magnetometer, working in an unshielded environment and including a feedback system to ensure a zero-field condition in proximity to the sensor, has been shown

to reach a sensitivity of $1pT/\sqrt{Hz}$ [85]. Moreover, a CPT magnetometer operating in a magnetically-compensated environment and using differential configuration for the detector has demonstrated accurate detection of a magnetic heart signal [58].

2.5 Summary

In this chapter, we have introduced the fundamentals of optical magnetometers and described their diverse operational modes, highlighting the sensitivities they can achieve. We have also discussed their advantages and disadvantages and finally reported on the potential applications for these devices. Furthermore, we have described electromagnetic environmental noise problems and given an overview of existing noise suppression techniques which are currently used in unshielded magnetocardiography.

Chapter 3

Optical Mx Magnetometer: principle of operation

In this chapter, we give a comprehensive explanation of the theory behind the operation of an optical Mx magnetometer, including: the atomic fine and hyperfine structures of an alkali metal (caesium); the optical pumping process and the effect of a radio-frequency radiation. Also, the behaviour of the magnetization vector inside the caesium gas cell is described by exploiting the Bloch equations. Finally, the sensitivity and frequency bandwidth of the instrument are analysed and discussed.

3.1 Introduction

The generic configuration of an optical Mx magnetometer is shown in Fig.3.1. A circularly polarized laser light transmitted through a glass cell containing a vapour of alkali atoms resonates when its frequency equals that of the first absorption line of the alkali atoms, thus creating electron spin alignment and precession with a frequency proportional to the modulus of an externally applied magnetic field, B_0 (Larmor frequency, $w_L = \gamma|B_0|$). If this precession is coherently driven by a radio-frequency (rf) magnetic field, B_{rf} (oscillating at frequency w_{rf}), the absorption coefficient of the alkali medium changes, thus modulating the transmitted optical intensity. By applying a weak magnetic field and maintaining the driving rf magnetic field resonant with the Larmor frequency, i.e., $w_{rf} = w_L$, the applied very-small magnetic field can be determined.

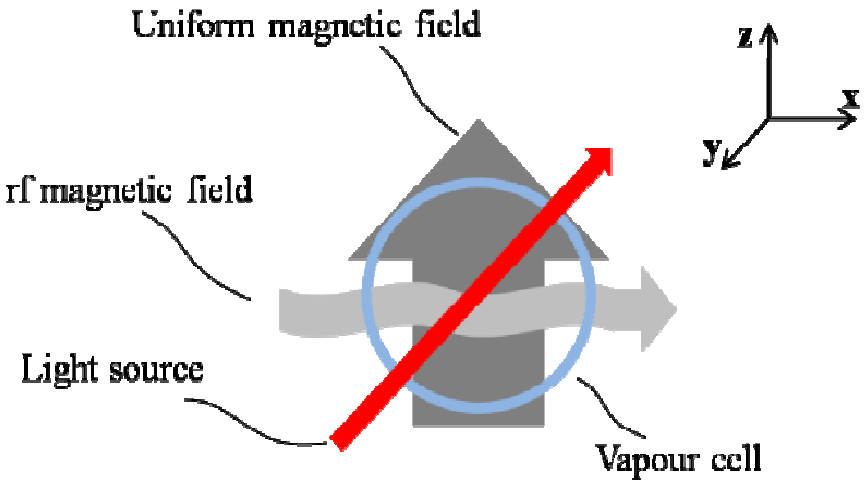

Fig.3.1: The generic configuration of an optical Mx magnetometer. The vapour cell contains alkali atoms, such as caesium atoms.

The core of the system is a glass cell filled with the vapour of one of the alkali metals that have only one electron in their outermost shell. Generally, caesium is used because it possesses only one stable isotope, ^{133}Cs, with a nuclear spin $I = 7/2$. The caesium atoms in the vapour cell interact with the external uniform magnetic field and with both the laser light and the radio-frequency oscillating magnetic field. In the following sections, we will explain the nature of those interactions and the effects that they have on the atomic structure.

3.2 Caesium fine and hyperfine structures

To understand the behaviour of caesium atoms when interacting with a light source, it is important to introduce the fine and the hyperfine structures of an atom. As explained in [86], the fine structure of an atom is a result of the coupling between the orbital angular momentum *L* of the outer electron and its spin angular momentum *S*. The total electron angular momentum *J* is then given by $J = L + S$ and the corresponding quantum number *J* must lie in the range: $|L - S| \le J \le L + S$. The hyperfine structure is a result of the coupling of *J* with the total nuclear angular momentum *I*. The total angular momentum *F* is then given by $F = J + I$ and the magnitude of *F* can lie in the range $|J - I| \le F \le J + I$. Each hyperfine energy level contains *2F+1* magnetic degenerated sub-levels. However, when an external magnetic field is applied, their degeneracy is broken (Zeeman Effect).

Energy levels splitting for the ground state in caesium:

$$\begin{cases} L = 0 \\ S = \frac{1}{2} \end{cases} \Rightarrow J = \frac{1}{2}. \tag{3.1}$$

For the first excited state:

$$\begin{cases} L = 1 \\ S = \frac{1}{2} \end{cases} \Rightarrow J = \frac{1}{2}, \frac{3}{2} \quad . \tag{3.2}$$

The energy of any particular level is shifted according to the value of *J*, so the $L = 0 \rightarrow L = 1$ (D line) transition is split into two components, the *D1* line $\left(6^2 S_{1/2} \rightarrow 6^2 P_{1/2}\right)$ and the *D2* line $\left(6^2 S_{1/2} \rightarrow 6^2 P_{3/2}\right)$, as shown in Fig.3.2.

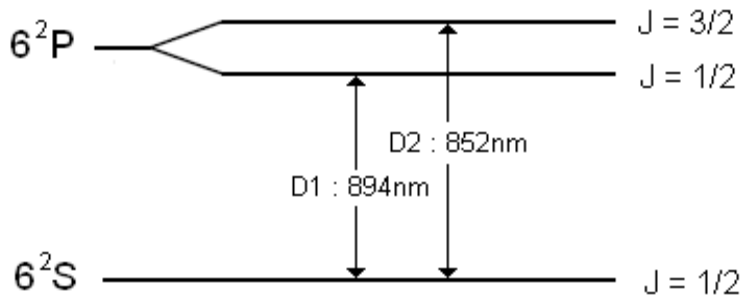

Fig.3.2: Caesium fine structure with highlighted D1 line and D2 line.

Since the fine structure splitting in caesium is large enough to be resolved by many lasers, the two D-line components can be treated separately. We will consider the *D1* line, hence for both the ground level and the excited state the angular momentum *F* is:

$$\begin{cases} J = \dfrac{1}{2} \\ I = \dfrac{7}{2} \end{cases} \Rightarrow F = 3,4 \ . \tag{3.3}$$

The atomic energy levels are shifted according to the value of *F*. In the presence of an external magnetic field, each hyperfine level splits into *2F+1* Zeeman sublevels, as displayed in Fig.3.3.

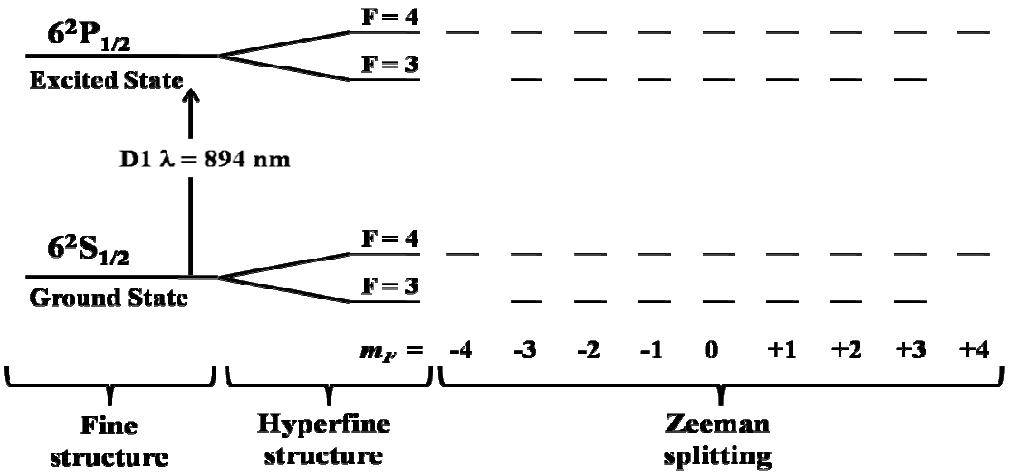

Fig.3.3 : Atomic fine and hyperfine structures and Zeeman splitting of the caesium D1 line.

The magnetic field also applies a magnetic torque on the atom's total angular momentum that starts to precess around the field axis at the Larmor frequency which is proportional to the field's magnitude: $w_L = \gamma |B|$, where γ is the gyromagnetic constant that for caesium has a value of $2\pi \times 3.5 Hz/nT$. In order to align all atomic magnetic moments in the same direction, a laser light tuned at the appropriate frequency is used to optically pump the caesium atoms inside the vapour cell.

3.3 Optical pumping and dark states

When a laser light with a wavelength equals to the first absorption line of the alkali atoms is transmitted through the vapour cell, the photons are absorbed by the caesium atoms, which then move from a ground state to an excited state.

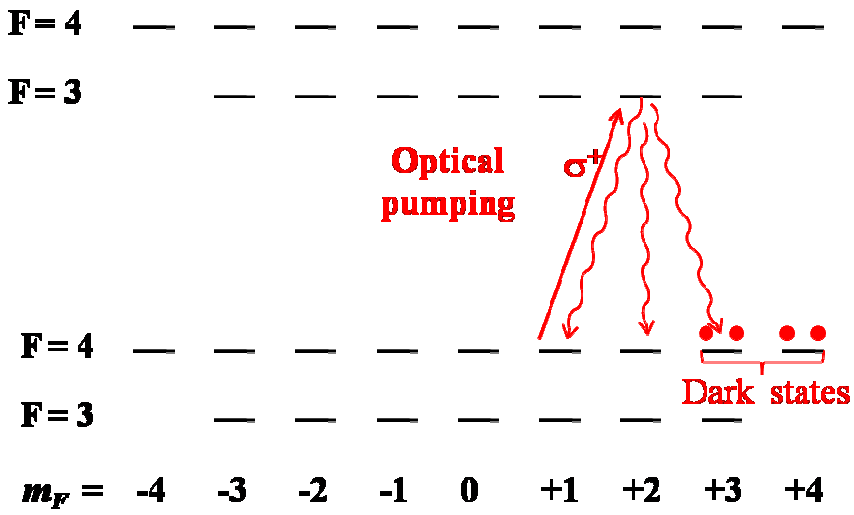

Fig.3.4: Optical pumping process with highlighted dark states.

Fig.3.4 shows the optical pumping over the $F = 4 \rightarrow F' = 3$ transition of the caesium D1 absorption line using right circularly polarized light, which results in the photon's angular momentum (σ^+) which is equal to +1. Hence, a caesium atom in the lower state with a quantum number m_F is only allowed to move to the upper level with $m_F^i = m_F + 1$ because of the total angular momentum conservation. A caesium atom that is in an excited state can then fall down via one of three possible decay channels and it spontaneously emits a photon which could

feasibly be sent in any direction and not necessary the direction of the light beam. Therefore, there is a finite probability for the atom to decay into a level with a larger m_F value. If the pumping process is repeated several times, the atom moves to one of the two outermost states (m_F = 3 and 4) of the ground level and, eventually, can no longer be optically pumped because there is no corresponding state in the excited level available for transition [87]. Since these atoms do not absorb light, they are called dark states. When the pumping process is saturated no more photons are absorbed. The caesium atoms in the dark state precess around the magnetic field's axis at the Larmor frequency whilst accumulating an increasing phase angle.

3.4 Radio-frequency radiation effect

The spin state of an atom can be changed to an absorbing (non dark) state through the absorption of resonant radio frequency radiation (w_{rf}), as shown in Fig.3.5. A change in the spin orientation causes a caesium atom to come out of a dark state into an absorbing state. Subsequently, the atom can be pumped again and after at least one pumping cycle it will revert to a dark state.

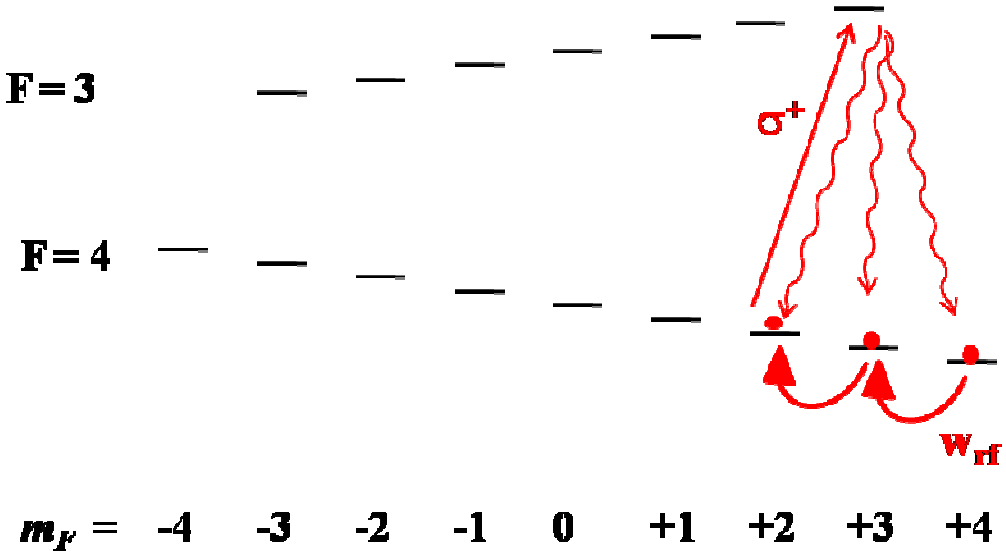

Fig.3.5: Atoms are pulled out of dark states by the effect of a resonant radio-frequency radiation.

This cycling process of pumping-saturation-pumping will result in a modulation of the laser light at the frequency of the rf radiation. The amplitude modulation of the transmitted light denotes that a large fraction of the atoms precess coherently in phase [46]. To maintain this coherence and synchronize the precession of atomic spins, the radio-frequency driving magnetic field must be resonant with the Larmor frequency, i.e., $w_{RF} = w_L$.

3.5 Atomic spin behaviour

The ensemble average of the magnetic moments associated with the spins can be treated as a classical magnetization vector M. The following explanation refers to the geometry illustrated in Fig.3.6. At the centre of the system is a vapour cell containing an appropriate atomic medium, a uniform magnetic field B_0 is directed along the z axis, a radio-frequency oscillating magnetic field B_{rf} is oriented along the x direction and a laser beam is transmitted through the atomic medium at an angle θ with respect to the z axis.

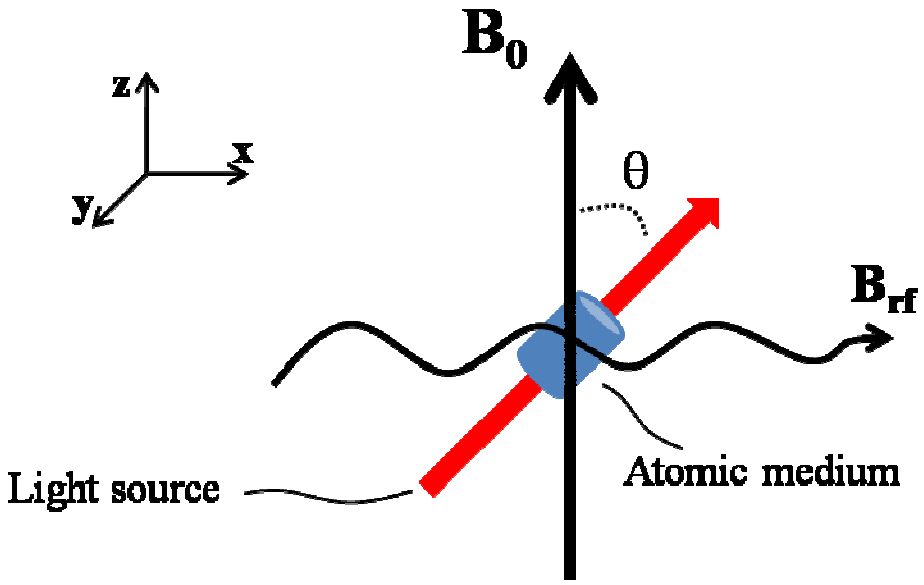

Fig.3.6: Geometry of the main components of a Mx magnetometer. At the centre of the system there is an appropriate atomic medium; the uniform magnetic field B_0 is directed along the z axis; the radio-frequency oscillating magnetic field B_{rf} propagates along the x direction, and the laser light is transmitted through the atomic medium along an angle θ with respect to the z axis.

Bloch equations [45] describe the precession of M around the total magnetic field ($B_{tot} = zB_0 + xB_{rf}cos(w_{rf}t)$):

$$\begin{pmatrix} \dot{M}_x \\ \dot{M}_y \\ \dot{M}_z \end{pmatrix} = \begin{pmatrix} M_x \\ M_y \\ M_z \end{pmatrix} \times \begin{pmatrix} \gamma B_{rf} \cos w_{rf} t \\ 0 \\ \gamma B_0 \end{pmatrix} - \begin{pmatrix} \Gamma_2 M_x \\ \Gamma_2 M_y \\ \Gamma_1 (M_z - M_0) \end{pmatrix}, \tag{3.4}$$

where Γ_1 and Γ_2 are the longitudinal and the transverse relaxation times, respectively, and M_0 is the magnetization in the absence of the radio-frequency field. Equation (3.4) can be rewritten and solved in the rotating frame, i.e., the frame co-rotating with the radio-frequency field. The time derivative of the magnetization vector in the rotating frame is related to the one in the laboratory frame as follows [87]:

$$\left(\frac{d\vec{M}}{dt} \right)_{rot} = \left(\frac{d\vec{M}}{dt} \right)_{lab} - \vec{w}_{rf} \times \vec{M} = \gamma \vec{M} \times \left(\vec{B}_{tot} + \frac{\vec{w}_{rf}}{\gamma} \right). \tag{3.5}$$

Hence, choosing the negative direction for the rotation frame, the Equation (3.4) in the rotating frame becomes:

$$\begin{pmatrix} \dot{M}_{x'} \\ \dot{M}_{y'} \\ \dot{M}_{z'} \end{pmatrix} = \begin{pmatrix} M_{x'} \\ M_{y'} \\ M_{z'} \end{pmatrix} \times \begin{pmatrix} \gamma\left(B_{rf}\right) \\ 0 \\ \gamma\left(B_0 - w_{rf} / \gamma\right) \end{pmatrix} - \begin{pmatrix} \Gamma_2 M_{x'} \\ \Gamma_2 M_{y'} \\ \Gamma_1 (M_{z'} - M_0) \end{pmatrix}. \tag{3.6}$$

Since in the rotating frame the problem is stationary, the time derivative of the magnetization vector can be set to zero, yielding:

$$\begin{pmatrix} -\Gamma_2 & \delta & 0 \\ -\delta & -\Gamma_2 & \Omega_R \\ 0 & -\Omega_R & -\Gamma_1 \end{pmatrix} \begin{pmatrix} M_{x'} \\ M_{y'} \\ M_{z'} \end{pmatrix} = \begin{pmatrix} 0 \\ 0 \\ -\Gamma_1 M_0 \end{pmatrix}, \tag{3.7}$$

where $\delta = \gamma B_0 - w_{rf} = w_L - w_{rf}$ is the frequency detuning from the Larmor frequency and $\Omega_R = \gamma B_{rf}$ is the Rabi frequency.

Solving equation (3.7) with respect to the components of the magnetization vector leads to:

$$M_{x'} = M_0 \frac{\Omega_R \delta}{\Gamma_2^2 + \delta^2 + \Omega_R^2 \frac{\Gamma_2}{\Gamma_1}}; \tag{3.8}$$

$$M_{y'} = M_0 \frac{\Omega_R \Gamma_2}{\Gamma_2^2 + \delta^2 + \Omega_R^2 \frac{\Gamma_2}{\Gamma_1}}; \tag{3.9}$$

$$M_{z'} = M_0 \frac{\delta^2 + \Gamma_2^2}{\Gamma_2^2 + \delta^2 + \Omega_R^2 \frac{\Gamma_2}{\Gamma_1}}. \tag{3.10}$$

These time-independent solutions in the rotating frame represent the steady-state precession of the magnetization vector with a frequency w_{rf} around the magnetic field's axis, which is the z-axis according to the geometry shown in Fig.3.6. Since the pumping laser light is right circularly polarized, this precession creates a modulation in the transmission coefficient that is proportional to the projection of M on the light vector and is measureable as an oscillation of the light power P. The calculated in-phase (P_{ip}) and quadrature (P_{qu}) amplitudes and the phase shift (ϕ) of light power with respect to the driving radio-frequency magnetic field, B_{rf}, can be calculated from Equations (3.8-3.10):

$$P_{ip}(\delta) = -P_0 \sin(2\theta) \frac{\Omega_R \delta}{\Gamma_2^2 + \delta^2 + \Omega_R^2 \frac{\Gamma_2}{\Gamma_1}}; \tag{3.11}$$

$$P_{qu}(\delta) = -P_0 \sin(2\theta) \frac{\Omega_R \Gamma_2}{\Gamma_2^2 + \delta^2 + \Omega_R^2 \frac{\Gamma_2}{\Gamma_1}}; \tag{3.12}$$

$$\phi = \arctan \frac{\Gamma_2}{\delta}. \tag{3.13}$$

where P_0 is the initial light power and θ is the angle between the laser beam and B_0. The in-phase and quadrature components as well as the phase shift can be measured by a phase-sensitive detector, such as a lock-in amplifier. It is important to notice from Equations (3.11) and (3.12) that both P_{ip} and P_{qu} are at their maximum when θ is equal to 45°. Under resonance conditions, i.e., when $\delta = 0$ and hence when the rf field is oscillating at the Larmor frequency ($w_L = w_{rf}$), the in-phase component that has a dispersive Lorentzian line shape is zero, while the quadrature component that has an adsorptive Lorentzian line shape is at maximum. Furthermore, Equation (3.13) shows a linear behaviour near resonance and predicts a phase shift between the light power and the driving rf field of 90° when $\delta = 0$.

3.6 Magnetometer sensitivity

The sensitivity of the optical Mx magnetometer is defined as the smallest change in magnetic field that can be detected by the magnetometer. The sensitivity can be calculated using the Cramer-Rao equation [88]:

$$\rho = \frac{4\sqrt{3}\sqrt{BW}}{\gamma SNR}, \tag{3.14}$$

where BW is the bandwidth, γ is the gyromagnetic constant and SNR is the signal-to-noise ratio of the magnetometer. The SNR can be calculated from the experimentally measured power spectral density (PSD) of the photodiode output.

Several important parameters can affect the sensitivity of a magnetometer, namely: (i) the laser power; (ii) the laser beam profile; (iii) the rf field power; (iv) the cell size and (v) the buffer-gas pressure which depends on the temperature. Typically, the magnetometer spatial resolution depends on the cell dimensions.

3.7 Magnetometer bandwidth

Another important feature of a magnetometer is its bandwidth, i.e., how fast the magnetometer responds to changes in the magnetic field. The bandwidth, f_{bw}, of the magnetometer can be calculated as [89]:

$$BW = \frac{\pi}{2}\Delta\nu\,, \tag{3.15}$$

where $\Delta\nu$ is the half width at half maximum (HWHM) bandwidth of the phase signal measured in hertz. As highlighted in Equations (3.11 - 3.13), the phase shift signal is the only signal that is not dependent on the radio-frequency magnetic field. Therefore, for the accurate evaluation of the bandwidth of the magnetometer, BW, it is important to use into Equation (3.15) the HWHM bandwidth, $\Delta\nu$, measured from the phase shift rather than the HWHM bandwidths, $\Delta\nu_X$ and $\Delta\nu_Y$, measured from the in-phase and quadrature components, respectively.

3.8 Summary

The working principle of an optical magnetometer in Mx configuration has been explained in this chapter, focusing on the interactions of atoms with the magnetic field, the light beam and the radio-frequency radiation. Moreover, we have described the atomic spin behaviour using Bloch equations. Finally, the parameters that affect the final sensitivity and the bandwidth of the instrument have been analysed and discussed.

Chapter 4

Adaptive Noise Cancellation based on Signal Processing

In this chapter, we describe the principle of operation of an adaptive noise cancellation system and of the algorithms used to adaptively update the coefficients of the filter in the noise canceller. Those algorithms can be divided in to two classes: Least-Mean Squares (LMS) based algorithms and heuristic optimization techniques, which include Genetic Algorithms (GA) and Particle Swarm Optimization (PSO).

4.1 Introduction

An adaptive noise canceller involves the use of multiple sensors, namely, (i) signal sensors that capture the signal of interest, which are typically placed as close as possible to the source, and (ii) noise sensors that capture environmental noise, which are placed far from the signal sensor, but not too far to ensure that the noise detected by the signal and noise sensors is almost the same. Adaptive noise cancellation techniques are typically used to extract the useful information from the noisy signal by means of signal processing. They are widely used in several applications, including, acoustic echo cancellation [90], de-noise of speech signals [91-93], suppression of noisy artefacts in magnetic resonance systems [94, 95], solution to random drift problem of Fibre Optics Gyroscope [96], and separation of multiple sources of motion in radar systems [97]. In addition, adaptive noise cancellation systems have largely been used to cancel noise in electrocardiography [98-100] and recently they started to be used in magnetocardiography as well [101].

The most common algorithm used for adaptive noise cancellation is the Least-Mean-Squares (LMS) algorithm, which is very effective in removing low noise levels, especially in electrocardiography [102, 103]. However, the LMS algorithm has limitations, namely, (i) it requires the calculation of the punctual derivative of the squared error; (ii) its convergence time is typically long, especially if the noise power to be removed is much higher than the signal power; and (iii) it is susceptible to the risk of falling into local minima. Recently, heuristic algorithms, such as Genetic Algorithms (GA) and Particle Swarm Optimization (PSO), have found a large space in adaptive noise cancellation applications [104, 105], such as image noise cancellation [106] and maternal interference removal from foetal electrocardiogram [107]. Compared to the LMS algorithm, the GA and PSO algorithms provide additional benefits, including (i) ability to perform parallel search for population points rather than for a single point, thus avoiding to fall into local minima; (ii) no prior information on the gradient of the signal is needed; (iii) the use of probabilistic rules instead of deterministic ones, thus ensuring the convergence to an optimum solution.

4.2 Adaptive Noise Canceller

Adaptive noise suppression techniques are typically based on adaptive filtering and require very little or no prior knowledge of the signal of interest. To suppress the noise, a reference input signal is required, which is typically derived from one or more magnetic sensors placed at positions where the noise level is higher than the signal amplitude. Fig.4.1 shows a block diagram of an adaptive noise canceller. The primary input to the canceller, denoted *d(k),* is the sum of the signal of interest *s(k)* and the noise *n(k)*, which is typically uncorrelated with *s(k)*. The reference input signal of the system, *x(k) = n1(k)*, is a noise that is correlated in some unknown way with *n(k)*, but uncorrelated with the signal of interest *s(k)*. As shown in Fig.4.1, *n1(k)* is adaptively filtered to produce a replica of the noise *n(k)* that can be subtracted from the primary input to eventually produce an output signal *e(k)* equals to *s(k)*. The objective of the noise canceller is to minimize the mean-squared error between the primary input signal, *d(k)*, and the output of the filter, *y(k)* [108].

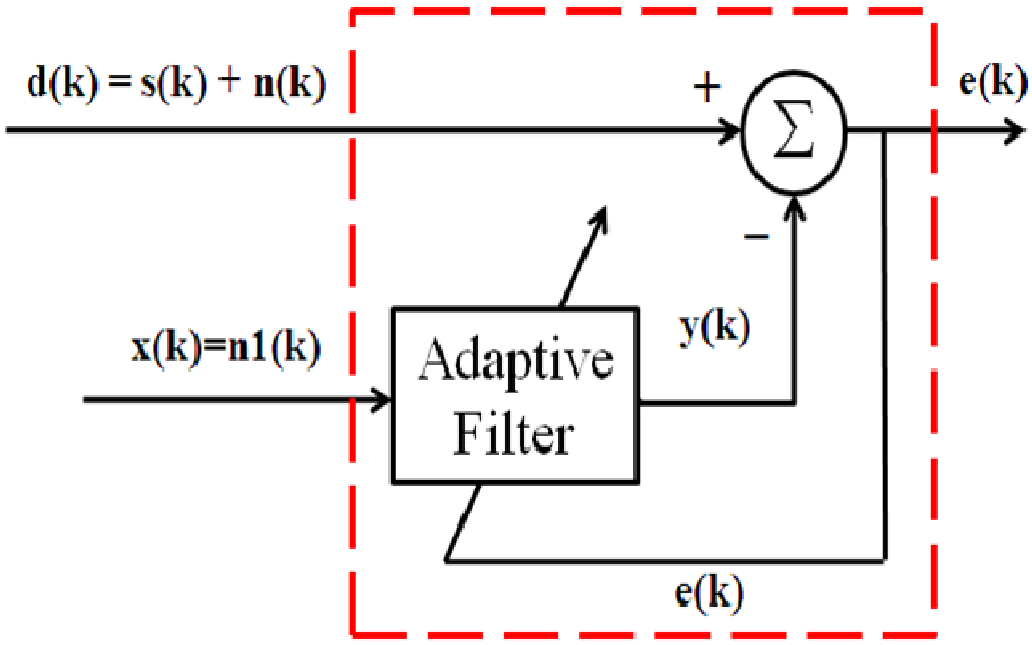

Fig.4.1. Typical block diagram of an adaptive noise canceller.

Referring to Fig.4.1, the output signal is given by

$$e(k) = d(k) - y(k) = s(k) + n(k) - y(k). \tag{4.1}$$

Therefore, the mean-squared of *e(k)* is given by

$$\begin{aligned} E\left\{e^2(k)\right\} = E\left\{s^2(k)\right\} + E\left\{\left(n(k) - y(k)\right)^2\right\} \\ + 2E\left\{s(k)\left(n(k) - y(k)\right)\right\} \end{aligned}. \tag{4.2}$$

Since *s(k)* is uncorrelated with *n(k)* and *y(k)*, the last term in Equation (4.2) is zero, yielding:

$$E\left\{e^2\left(k\right)\right\} = E\left\{s^2\left(k\right)\right\} + E\left\{\left(n\left(k\right) - y\left(k\right)\right)^2\right\}. \tag{4.3}$$

It is noticed from Equation (4.3) that the mean-squared error is minimum when *n(k) = y(k)*, and hence, when the output signal *e(k)* is equal to the desired signal *s(k)*.

4.3 LMS based algorithms

The LMS algorithm is based on the steepest descend algorithm that aims to minimize the mean-squared error. The steepest descend algorithm updates the filter parameters based on the gradient of the mean-squared error ε, calculated from the transfer function of the filter, governed by:

$$f_i^{(k+1)} = f_i^{(k)} - \mu\nabla(\varepsilon) = f_i^{(k)} - \mu\frac{\delta E\left\{e^2(k)\right\}}{\delta f(k)}, \tag{4.4}$$

where μ is the adaption rate.

The steepest descend algorithm assumes the complete knowledge of the gradient, but generally this is not always possible. The LMS algorithm replaces it with an estimation given by the punctual derivative of the squared error:

$$\hat{\nabla}(\varepsilon) = \frac{\delta e^2(k)}{\delta f(k)}. \tag{4.5}$$

Assuming that the adaptive filter is an FIR filter of order M [109], then Equation (4.1) becomes:

$$e(k) = d(k) - \sum_{i=0}^{M-1} b_i x(k-i). \tag{4.6}$$

The updating procedure is applied on coefficients b_i following the above rule [109]:

$$b_i^{(k+1)} = b_i^{(k)} + 2\mu e(k) x(k-i), \tag{4.7}$$

Where $k = 0,1,\ldots,M-1$ and μ is the step size.

The step size μ usually is included in the range (0,1]; the condition to assure convergence and stability is given by [109]:

$$0 < \mu < \frac{2}{ME\{x^2(k)\}}. \tag{4.8}$$

With the filter length M, the LMS algorithm has computational complexity of O(M).

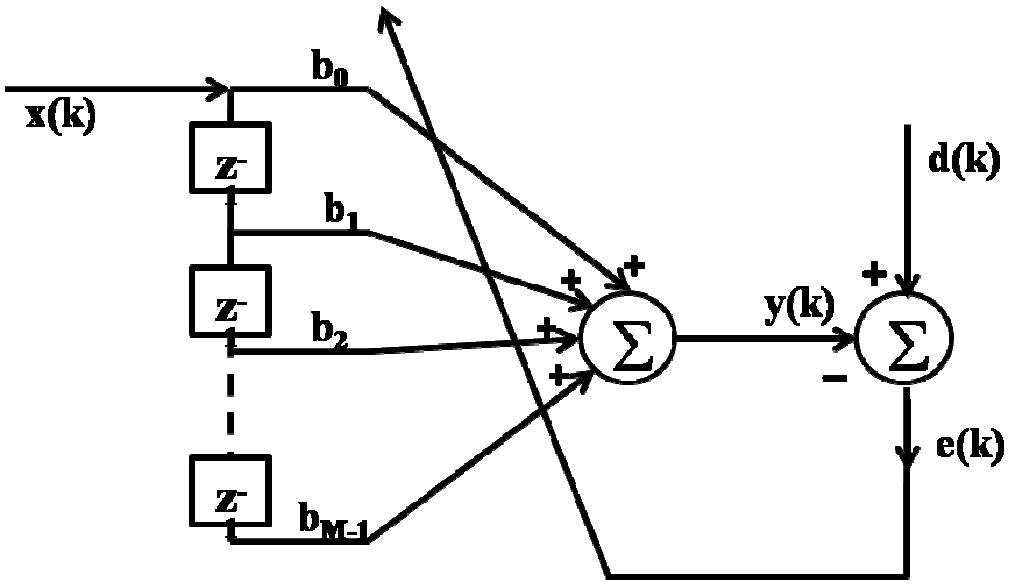

Fig.4.2: LMS FIR filter coefficients updating.

The LMS algorithm can have high convergence time especially if the noise to be removed is much larger than the signal. To increase the convergence speed, a variable adaption rate can be used. This is a variant of the LMS algorithm called normalised LMS. Equation (4.7) now can be written [109]:

$$b_i^{(k+1)} = b_i^{(k)} + 2\mu_k e(k)x(k-i)\,, \tag{4.9}$$

where

$$\mu_k = \frac{\mu_n}{\|x(k)\|^2}, \qquad 0 < \mu_n < 2\,. \tag{4.10}$$

The normalization of the LMS step size by $\|x(k)\|^2$ will reduce the convergence time.

4.4 Heuristic Algorithms

4.4.1 Genetic Algorithm

Genetic Algorithms (GA) are part of the Evolutionary Algorithms, which are stochastic, population-based techniques inspired by the natural evolution process [110]. Using GA, the optimal solution is found through the minimization of a defined function, called the fitness function. For the problem of magnetic noise cancellation, the objective of the optimization process is to minimize the MSE, defined in Equation (4.3). Fig.4.3 shows a typical flowchart of the Genetic Algorithm.

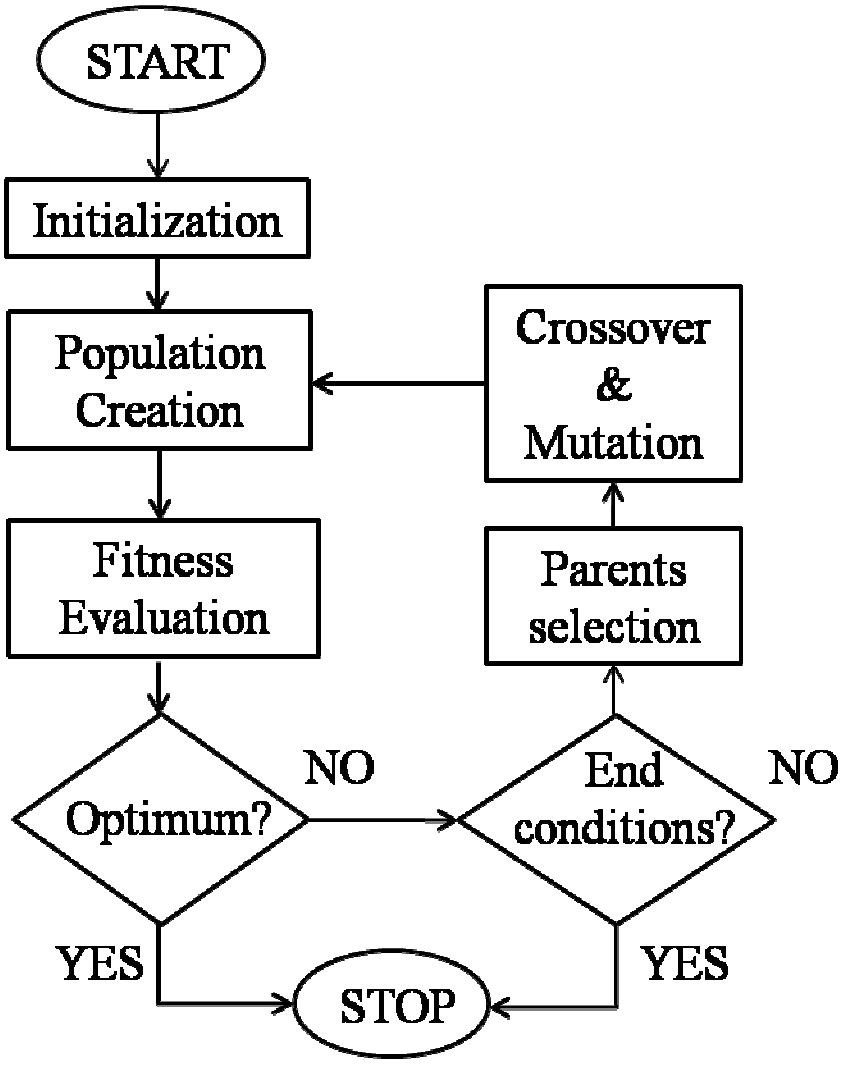

Fig.4.3: Genetic Algorithm (GA) flowchart.

The initialization process produces a random initial population. For each individual belonging to the population, the fitness function is evaluated to find the fitness value of that individual. If the value of the fitness function for the best point in the current population is less or equal to a pre-defined threshold value, it is therefore considered as the optimum value and the iteration will be terminated. A few predefined end conditions are evaluated to avoid an infinite loop in case the optimum value cannot be found. If none of the predefined end conditions is verified, the algorithm proceeds with the reproduction, i.e., the creation of new generation. The individuals that have higher fitness values are chosen as parents to produce children either by mutation (making random changes to a single parent) or crossover (combining the vector entries of pair of parents). Each individual can be seen as an array of chromosomes. As for natural evolution, during the reproduction the chromosomes of parents are mixed together to form the children, according to the following rule [111]:

$$C = \alpha P_1 + (1-\alpha) P_2, \tag{4.11}$$

where: C is a child, $P_{1,2}$ are the two parents and α is a randomly generated number in the range (0,1). The current population is then replaced with the new generation and the iteration continues.

4.4.2 Particle Swarm Optimization Algorithm

Particle Swarm Optimization (PSO) algorithm, first described by Kennedy and others in [112], belongs to a class of metaheuristic algorithms called Swarm Intelligence, which is based on the social behaviour of animals, such as bird flocking, when they search for food. In PSO, particles denote a population of potential solutions. Each individual moves in the search space exploring for better solutions, and its behaviour is affected by its current position, its best known position (personal best) and the shared knowledge of the swarm (global best). A population of M particles, in which each individual, k, represents a potential solution, is defined as a point in an N-dimensional space. The function to be optimized, called fitness function, defines the search space and the number of

variable in that function define the space's dimensions. Fig.4.4 shows the flowchart of the PSO algorithm.

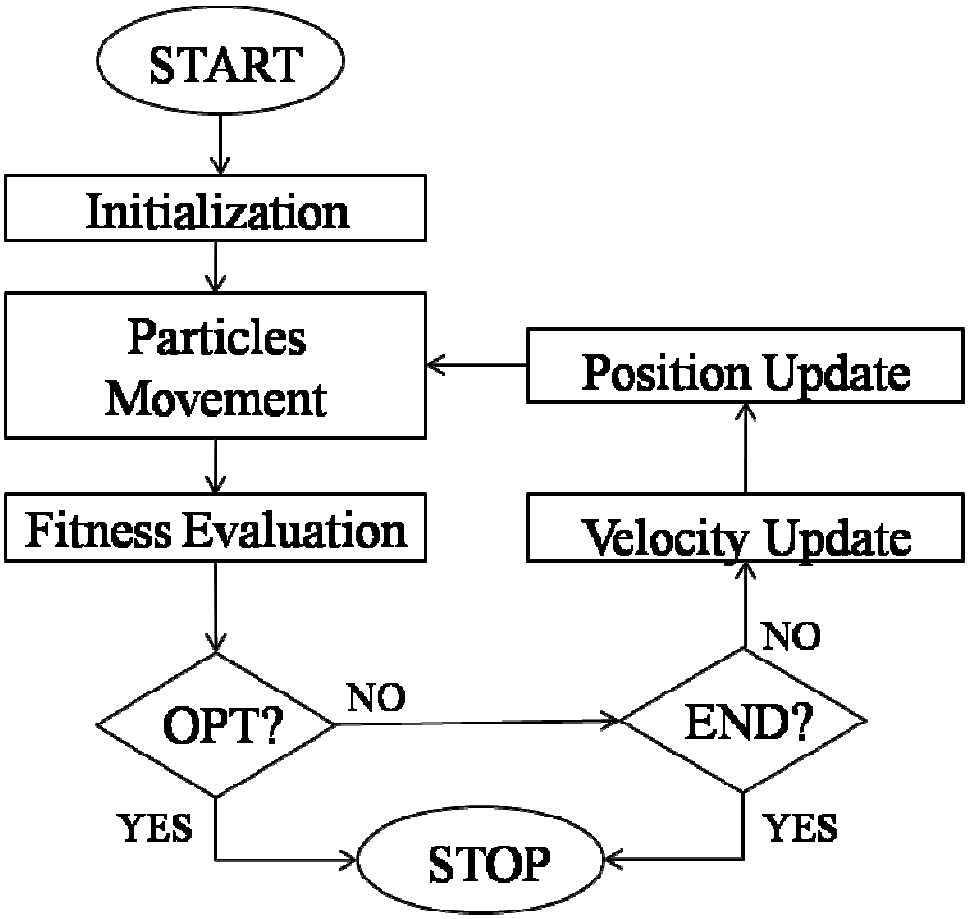

Fig.4.4: Flowchart of the Particle Swarm Optimization (PSO) algorithm.

Each particle is characterized by a position in the search space and a velocity that represents the amount of change in the position in the next iteration. The initialization process assigns a random start position and random velocity to each particle of the population. For each particle, the fitness function is evaluated to find the fitness value. If, for a pre-established number of iterations, the change in the best fitness value is lower than a defined threshold value, or if the maximum number of iterations is reached, then the iteration cycle will be terminated. If none of above conditions is verified, the algorithm proceeds with the update of velocity and position.

The new velocity and position are calculated using the current velocity and the distance from the current position and the personal and global best position, according to the following equations [113]:

$$v_k(i+1) = \varphi(i)v_k(i) + a_1\left[c_{1k}\left(P_k - x_k(i)\right)\right] + a_2\left[c_{2k}\left(G_k - x_k(i)\right)\right], \tag{4.12}$$

$$x_k(i+1) = x_k(i) + v_k(i+1), \tag{4.13}$$

where: i is the iteration index, k is the particle index, v_k is the velocity of the kth particle, x_k is the position of the kth particle, P_k is the personal best (best position) found by the kth particle, G_k is the global best (best position) found by the swarm, $c_{1,2}$ are randomly-generated numbers in the range (0,1), $a_{1,2}$ are the acceleration constants (in the algorithm, the optimum values were found to be $a_1 = 1.5$ and $a_2 = 2.2$) and $\varphi(i)$ is the inertia function (which is defined as: $\varphi(i)=0.9 - i(0.6/50)$).

The velocity update consists of three parts: the first part considers the current position of the particle, the second part is linked to the particle's best known position among past positions (personal best) and the third part involves the shared knowledge of the swarm (global best). Those three components are weighted (multiplied) by the inertia function and the acceleration constants, respectively. For the adaptive noise cancellation problem, the fitness function is defined as the mean-squared error between the primary input signal, d(k), and the output of the filter, y(k) (Fig.4.1):

$$E\left\{e^2(k)\right\} = \frac{\sum_{k=1}^{L} e^2(k)}{L}, \tag{4.14}$$

where L is the number of samples representing the signal.

The number of variables of the fitness function equals to the number of coefficients of the adaptive filter, which defines the dimensions of the search

space. Note that an efficient Particle Swarm Optimization Toolbox for use with Matlab is readily available [114, 115], and was used to generate the simulation results.

The GA shares many properties with the PSO algorithm, including (i) the applicability across a wide range of problems, (ii) no requirements for a prior knowledge of the problem space and (iii) ease of development. However, the PSO usually has a higher convergence time.

4.5 Summary

The principle of operation of an adaptive noise cancellation system has been presented in this chapter as well as the different algorithms which were used for the adaptive update of the filter coefficients of the noise canceller. Those algorithms were the Least-Mean Squares (LMS) based algorithms, the Genetic Algorithms (GA) and Particle Swarm Optimization (PSO) algorithm.

Chapter 5

Development and characterization of the Mx magnetometer

In this chapter, we describe the components and setup of the developed optically-pumped quantum magnetometer. We also present the experimental results of the optimization and characterization of the sensitivity and frequency bandwidth of the instrument, with respect to the laser light power and vapour cell temperature.

5.1 Experimental setup

The experimental setting of the Mx magnetometer is shown in Fig.5.1 (a) and (b). The system can be divided into four main blocks: (i) frequency-stabilized laser light source, (ii) uniform and oscillating magnetic fields generation system, (iii) sensing head and (iv) detector electronics. These blocks are discussed in detail in the subsequent sections.

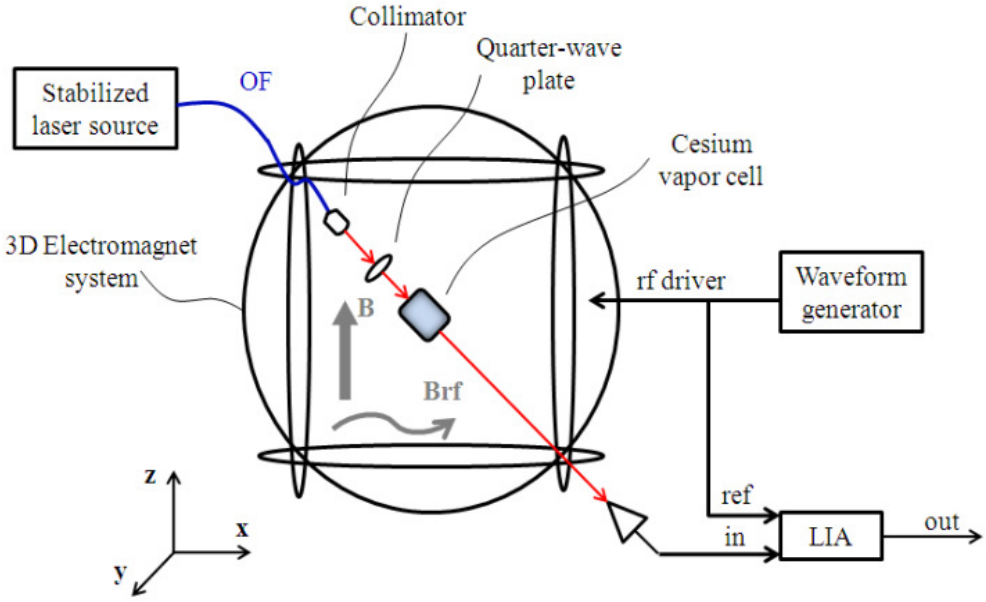

(a)

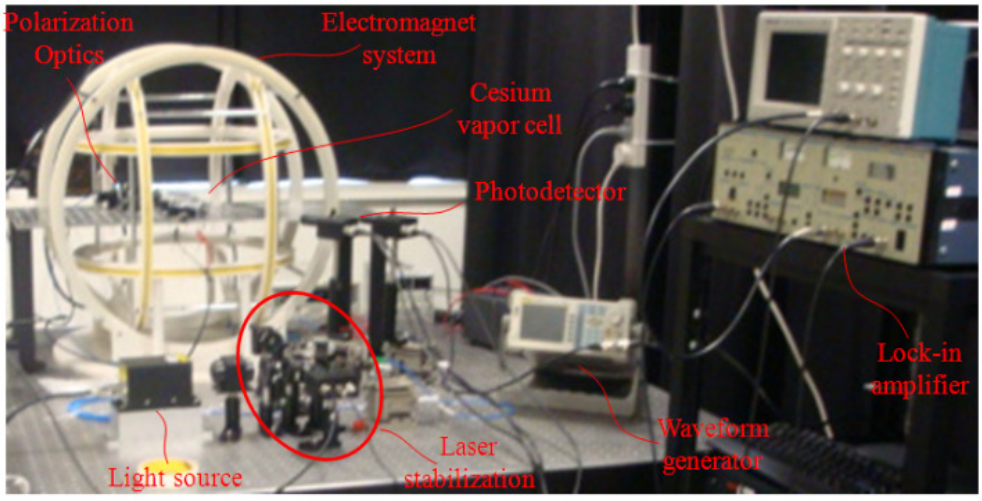

(b)

Fig.5.1: (a) Block diagram and (b) photo of the experimental setup demonstrating the concept of the optical Mx magnetometer.

5.1.1 Frequency-stabilized laser light source

An external-cavity semiconductor laser (made by Uniquanta Technology, Beijing, China) was used as the light source for both pumping and probing. The laser wavelength was tuned to 894nm which is equal to the caesium D1 absorption line F=4→F′=3 transition, and stabilized using saturation spectroscopy in an auxiliary cell [116]. The frequency stabilized light was coupled into single-mode polarization maintaining optical fibre of 5μm core diameter, and delivered to the sensing head. Fig.5.2 shows the linear polarization of the light (red arrow), the saturation spectroscopy set up to stabilize the light frequency (blue arrows) and the collimation of the laser beam into the optical fibre (green arrow).

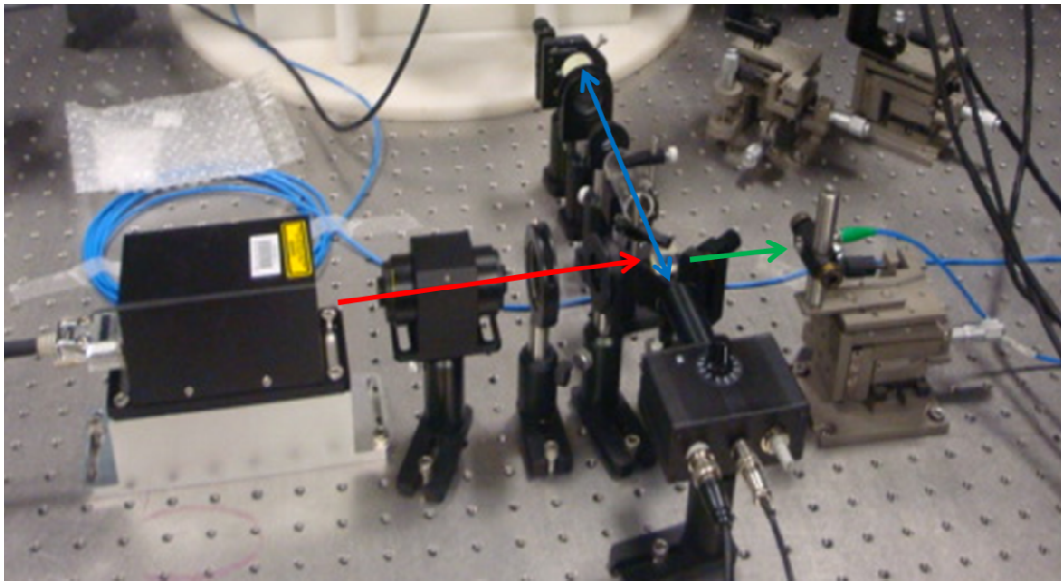

Fig.5.2: Laser light source highlighting the linear polarization optics (red arrow), the saturation spectroscopy set up (blue arrows) and the light-optical fibre coupling (green arrow).

As shown in Fig.5.2, the beam coming from the laser cavity propagates into an optical isolator and the light beam diameter is adjusted by an optical iris, hence the light beam passes through a half wave plate and a polarizer beam splitter that allows the polarization angle to be adjusted. The two resulting laser beams are linearly polarized. One of them is used to stabilize and lock the light frequency, while the other is collimated and coupled into the optical fibre.

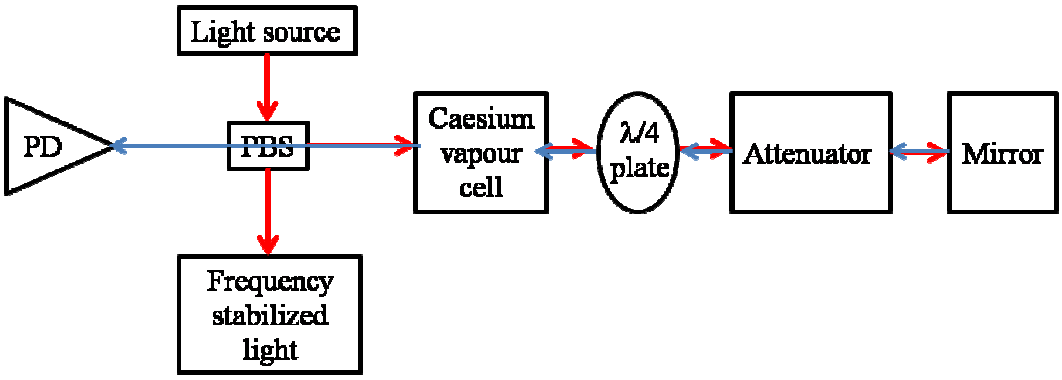

Fig.5.3: Saturation spectroscopy setup.

In principle, light radiation can interact with the atomic vapour only if its propagation frequency is equal to the gap between two energy levels of the atom. Due to the thermal motion of the atoms, this resonance frequency is Doppler-shifted by an amount proportional to the atomic velocity. Saturation spectroscopy enables Doppler-broadened free laser frequency to be attained. As shown in Fig.5.3, the laser light from the laser source is split in two by a polariser beam splitter (PBS); one beam is transmitted through a caesium vapour cell, a quarter-wave plate, an attenuator and is then reflected by a mirror. The reflected light beam (which is the probe beam) is overlapped to the original beam (which is the pumping beam) and flows back through the caesium vapour cell to reach a photo detector (PD), whose output represents a feedback loop to the laser light driver.

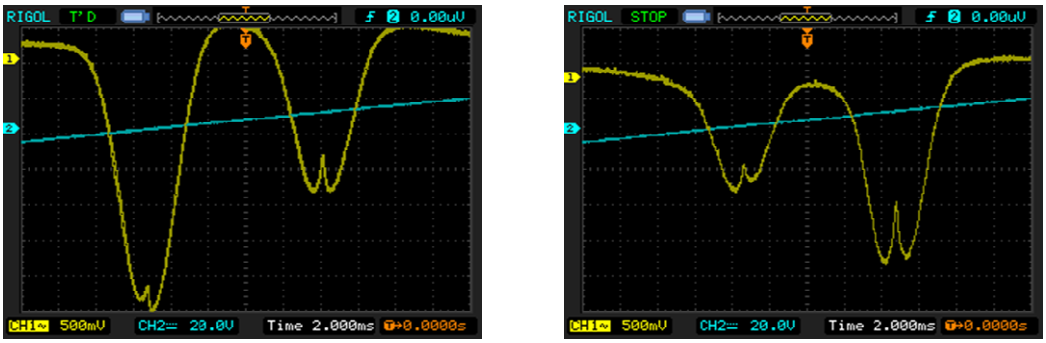

Fig.5.4: Spectra of the saturated absorption lines of the D1 line of caesium: (a) F=4→F'=3 and F=4→F'=4 transitions and (b) F=3→F'=3 and F=3→F'=4 transitions.

The pump beam causes a population change that is dependent on the velocity of the atoms caused by the Doppler shift. If the pump light has a high power it can rapidly pump atoms into an excited state causing the effect of saturation, where half the population is in the excited state and half in the ground state. The signal from the overlapping probe beam can be used to measure the Doppler-broadened spectral lines and the saturation lines. Fig.5.4 shows the spectra of the saturated absorption lines of the D1 line of caesium: (a) F=4→F′=3 and F=4→F′=4 transitions and (b) F=3→F′=3 and F=3→F′=4 transitions. In this experiment the laser light is locked to the F=4→F′=3 transition.

5.1.2 Magnetic fields generation system

A three dimensional electromagnet system was used to generate both the uniform and the radio-frequency oscillating magnetic fields.

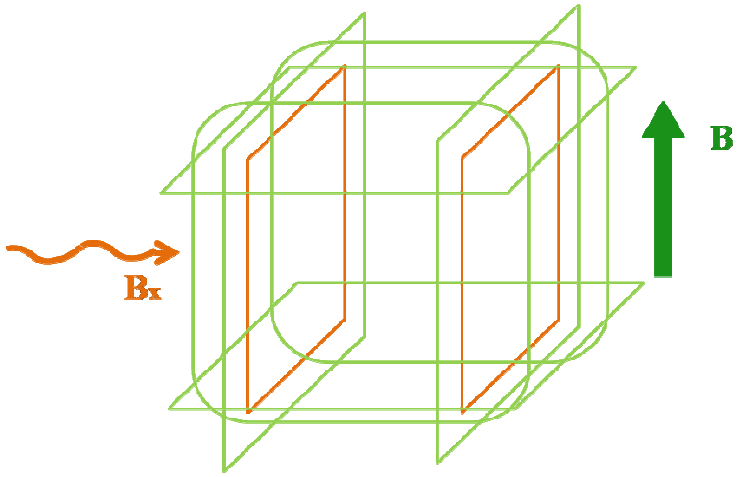

Fig.5.5: Electromagnet system consisting of a 3-D Helmholtz coils system (green coils) for cancelling the geomagnetic field and generating a uniform field and a Helmholtz coils pair (orange coils) for generating the rf oscillating field.

As shown in Fig.5.5, the electromagnet used in the experiments consists of two parts: (i) a 3-D DC coils of dimension 580mm×530mm×640mm providing a magnetic field with a uniformity better than 1% in the central region; and (ii) an additional pair of coils that generate a small-magnitude radio-frequency magnetic field along the x axis.

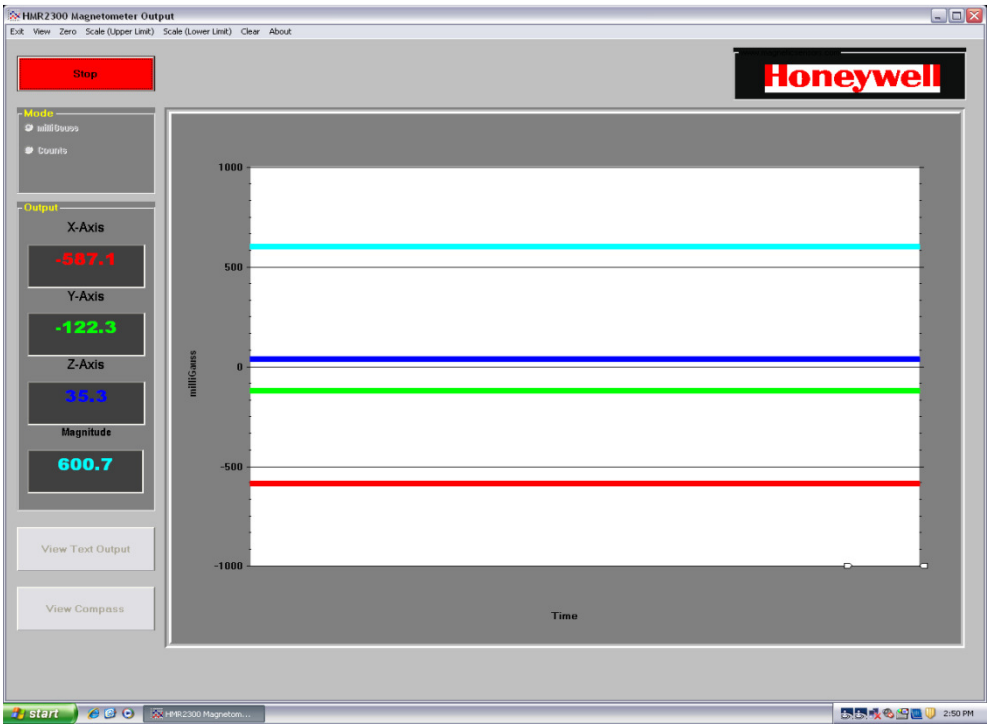

(a)

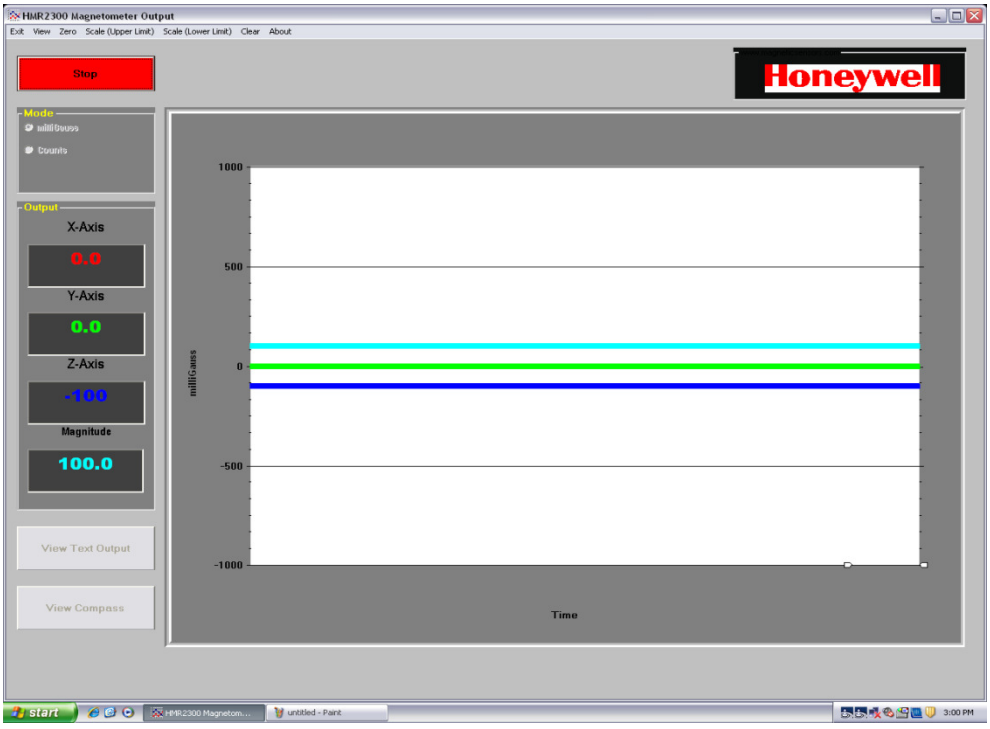

(b)

Fig.5.6: (a) Measured geomagnetic field and (b) generated uniform field (with intensity of 10μT) after geomagnetic field cancellation. The Honeywell magnetometer unit of measurement is milliGauss.

The intensity of the magnetic field at the centre of the electromagnet was measured by a three-axes smart digital magnetometer Honeywell HMR2300. As shown from Fig.5.6 (a), the geomagnetic field measured at the centre of the electromagnet exhibits strong components along the x-axis and y-axis, while it is weak along the z-axis. Each coil-pair of the electromagnet was then independently driven by a digital power supply to cancel the geomagnetic field along the x and y directions, and generate a uniform magnetic field along the z axis, as shown in Fig.5.6 (b). The AC coils were driven by a waveform generator (Agilent, model 33250A) to produce a radio-frequency oscillating magnetic field along the x-axis.

5.1.3 Sensing head

The sensing head contained an array of two sensors. Fig.5.7 shows a block diagram of the sensing head of the instrument.

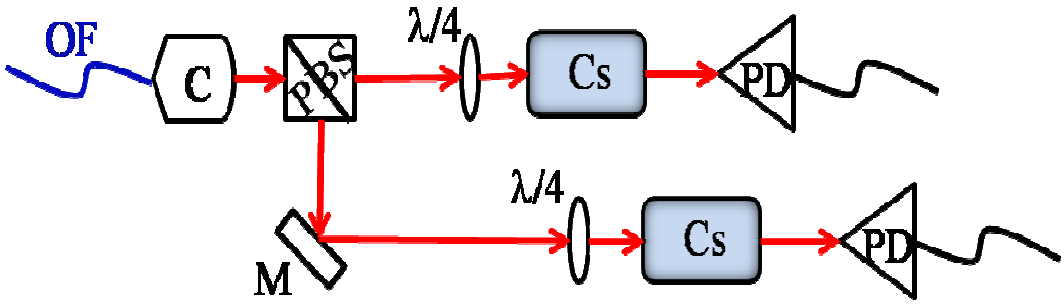

Fig.5.7: Block diagram of the sensing head made by an array of two sensors.

The frequency stabilized light was coupled into a single-mode polarization maintaining optical fibre and delivered to the vapour cells which were placed inside the electromagnet. At the cells location, the light was collimated, providing an output beam diameter of 1.6mm, split into two beams of equal power and right circularly polarized using a half-wave plate, an optical polarizer beam splitter, a mirror and two quarter-wave plates. The laser beams were transmitted through the vapour cells at an angle of 45 degree with respect to both the z-axis and the x- axis and then detected by two photodiodes placed outside the electromagnet.

The core of each sensor was a quartz-made cylindrical cell containing caesium vapour. Also, Neon gas at 34Torr and Argon gas at 6Torr were added to

the Cs vapour in order to reduce atom collisions. The cell diameter and length were 21mm and 75mm, respectively, yielding a spatial resolution of about 53mm when the cell was tilted at an angle of 45 degree with respect to both the z- and the x- axes. In the experiments, the gas pressure inside the cell was increased by increasing the temperature using hot water flowing into a silicon pipe wrapped around the cell. Fig.5.8 displays the electromagnet containing, in its centre, the two vapour cells and the polarization optics; the heating system is shown in the inset of Fig.5.8.

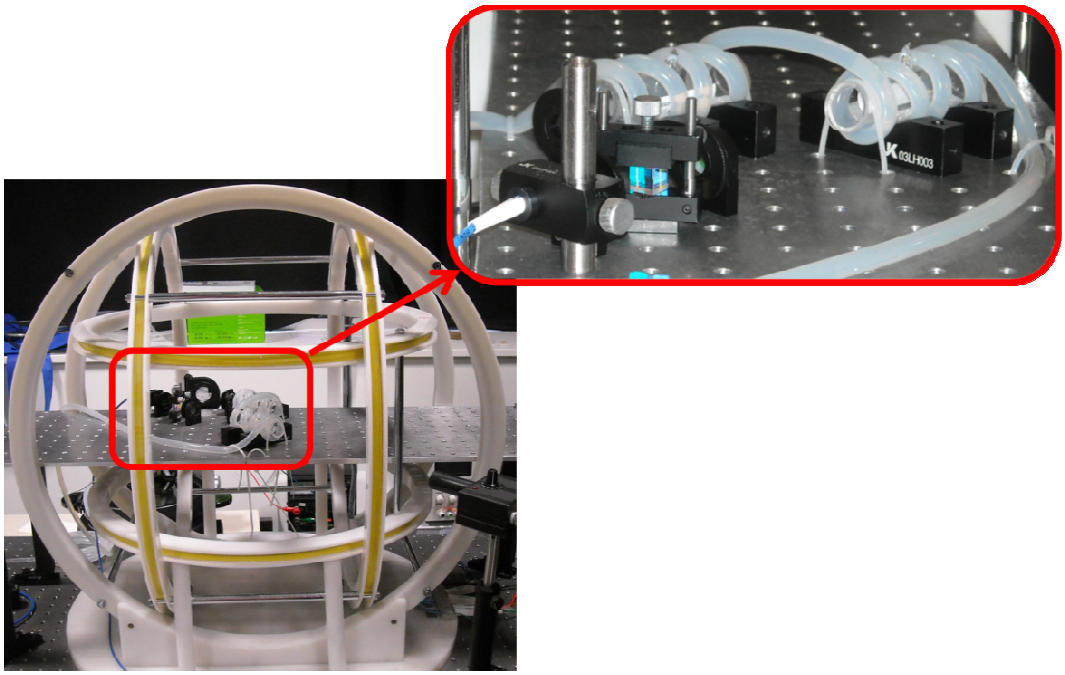

Fig.5.8: Picture displaying the sensing head placed in the centre of the electromagnet; the vapour cells with the heating system and the polarization optics are shown in the inset.

5.1.4 Detector electronics

The output light beam was focused into two photodiodes (PED801 from UniQuanta Technology), which were placed outside the electromagnet, as shown in Fig.5.9, in order to reduce the magnetic interference produced by the transimpedance amplifier of the photodiodes' packages.

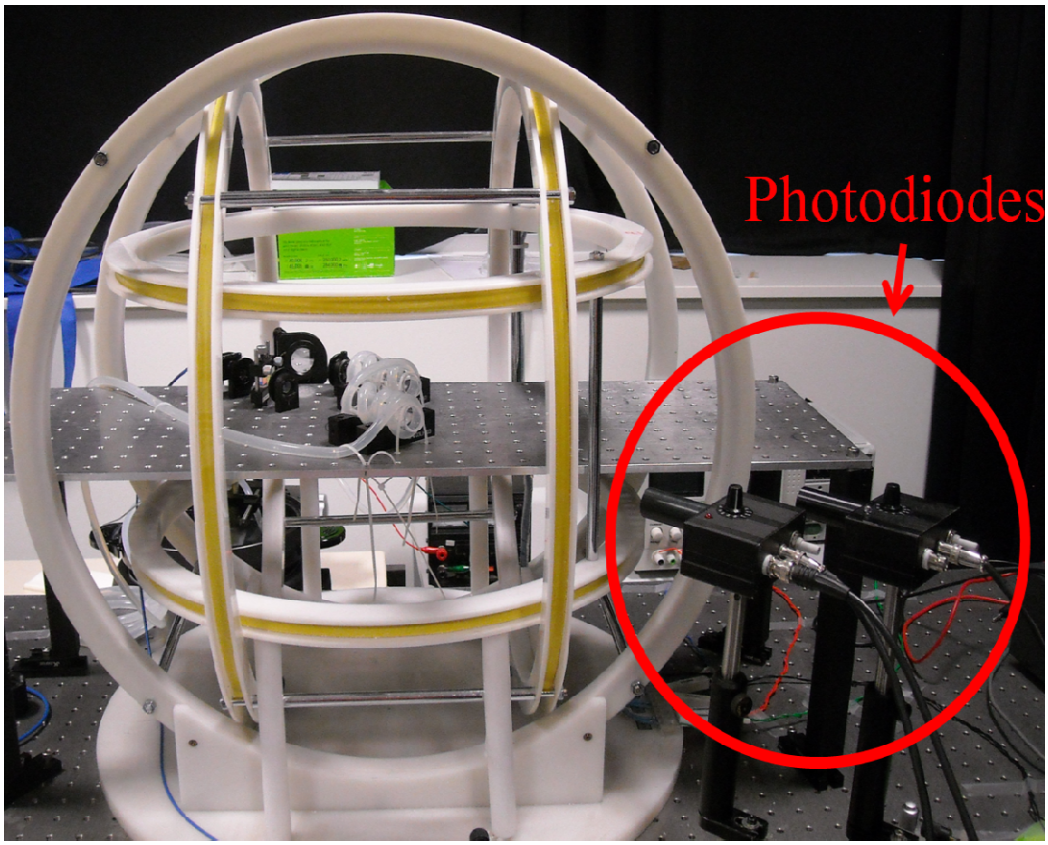

Fig.5.9: Photodiodes placed outside the electromagnet in order to reduce interference.

A lock-in amplifier (Stanford Research Systems, model SR530) was used to measure the phase shift between the photocurrent detected by a photodiode, with respect to the oscillating rf magnetic field, as well as the in-phase component and the quadrature component. Note that, by sweeping the frequency of the rf magnetic field along the Larmor frequency, it was possible to measure the half width at half maximum (HWHM) of the in-phase, the quadrature and the phase signals. Furthermore, a spectrum analyser (Agilent, model E4407B) was used to measure the power spectral density of the photodiode output in order to calculate the signal-to-noise ratio, and hence the intrinsic and actual sensitivity of the optical Mx magnetometer.

5.2 Experimental conditions

It is important to mention that all the experimental results reported below were performed in a laboratory environment without any magnetic shield. The uniform magnetic field along the z-axis was 13μT corresponding to a Larmor frequency of 45.5kHz. It is also important to note that when the measurements were carried out with different uniform dc magnetic field intensities the performances of the magnetometer were not affected. The intensity of the rf magnetic field was 200nT. In the experiments, the optical Mx magnetometer was operated in free-running mode without the use of a feedback loop between the lock-in amplifier and the signal generator to lock the rf frequency to the Larmor frequency. In particular, the dependence of the sensitivity and the bandwidth of the optical Mx magnetometer on cell temperature and optical power were investigated for different input optical power levels (from 5μW to 20μW) over a cell temperature range of 23°C to 55°C. Since the two sensors were identical, the characterization of the sensitivity and frequency bandwidth dependent on the light power and vapour temperature was made only on one sensor.

5.3 Sensitivity optimization

The sensitivity of the optical Mx magnetometer is calculated from Equation (3.14). The SNR can be calculated from the measured power spectral density (PSD) of the photodiode output, as illustrated in Fig.5.10. Since the magnetometer was operated in a magnetically-unshielded environment, all the measurements were dominated by magnetic field noise.

The intrinsic signal-to-noise ratio was calculated with the noise being the intrinsic rms noise of the magnetometer, measured over 100Hz from the resonance frequency. The actual signal-to-noise ratio was calculated by taking into account the sidebands induced by the 50Hz magnetic noise produced by power lines. Fig.5.11 shows (a) the intrinsic SNR and (b) the intrinsic sensitivity of the magnetometer versus the cell temperature at different input optical power levels.

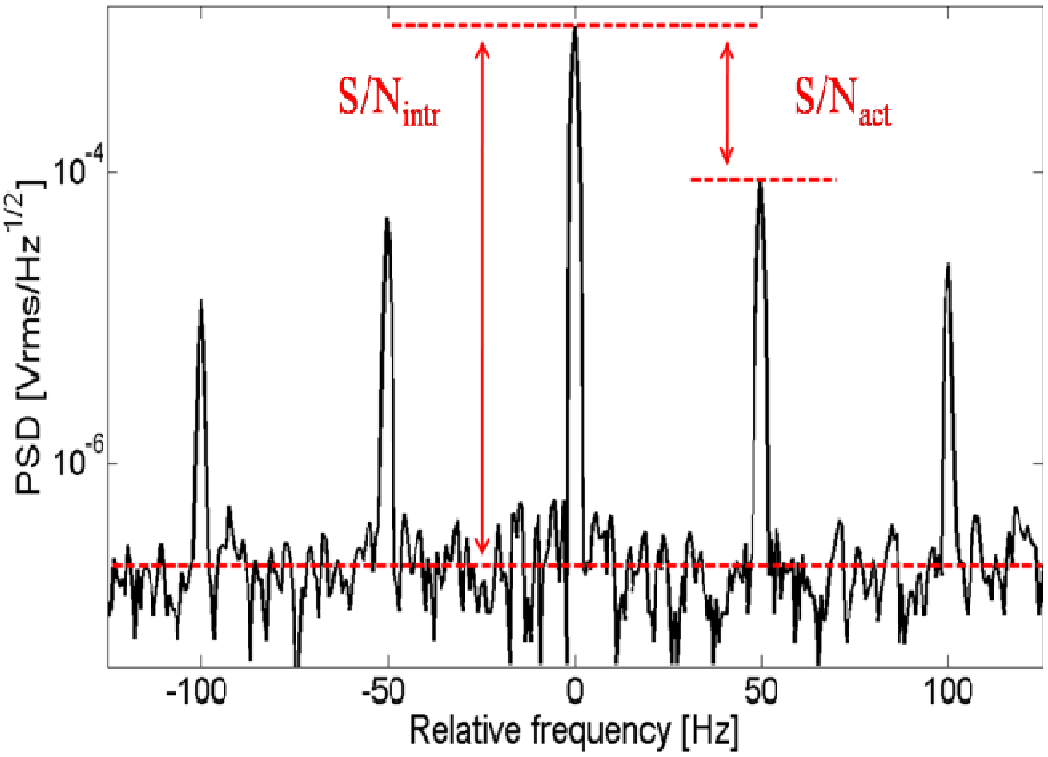

Fig.5.10: Power Spectral Density (PSD) of the photodiode output normalised to the resonance frequency. The spectrum was measured in a 1Hz bandwidth. The signal was recorded with optical power of 20μW and cell temperature of 50 ℃. The intrinsic and actual signal-to-noise ratios are highlighted.

The intrinsic SNR, and hence the intrinsic sensitivity, curve exhibits a similar trend for all input optical power levels, namely, the SNR increases when the temperature is increased, reaching a maximum value around 50°C before it then starts to decrease. Moreover, increasing the input optical power increases the intrinsic SNR, and hence the intrinsic sensitivity. In fact, when the temperature is increased, the gas pressure inside the vapour cell increases, resulting in a higher number of atoms interacting with the light and coherently precessing around the magnetic field at the Larmor frequency. Furthermore, increasing the input optical power results in a greater number of atoms being optically pumped. However, when the gas pressure is too high, the collisions of atoms with each other or with the walls of the cell lead to phase incoherence during precession, thus reducing the SNR performance of the magnetometer. The best performance of the magnetometer was obtained with an input optical power of 20μW and a cell

temperature of 50°C. The measured intrinsic SNR was 5000 and the intrinsic sensitivity was 63fT/Hz$^{1/2}$, measured in a 1Hz bandwidth.

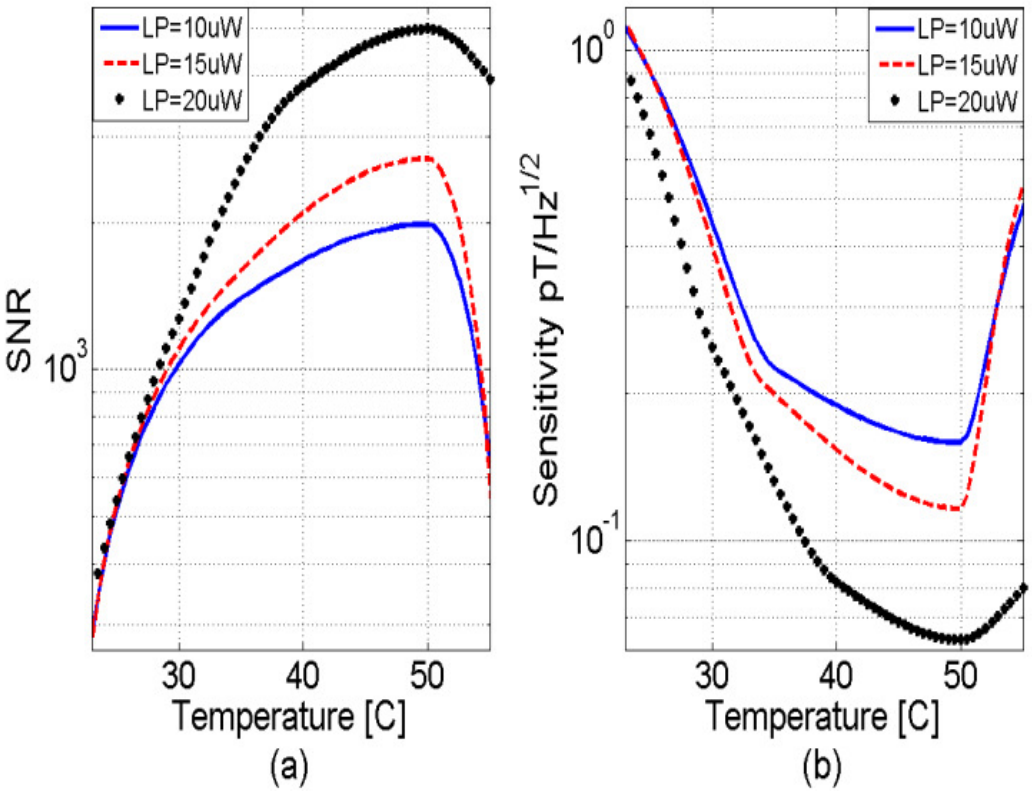

Fig.5.11: (a) Intrinsic signal-to-noise ratio (SNR) and (b) intrinsic sensitivity, measured in a 1Hz bandwidth versus cell temperature for input optical power of 10μW, 15μW and 20μW.

To obtain the actual SNR and the actual sensitivity of the magnetometer, the SNR was calculated by taking into account the external magnetic noise. The actual sensitivity is strongly dependent on the location of the magnetometer. All the experiments reported in this paper were performed in a laboratory environment without any magnetic shield. This resulted in a very poor actual signal-to-noise ratio, and hence, a very low actual sensitivity. Fig.5.12 (a) and (b) show the actual SNR and the actual sensitivity of the magnetometer, respectively. It was also noted in this situation, that the actual SNR increases (and hence the actual sensitivity is enhanced) with increasing the input optical power. However, the actual SNR decreases by increasing the cell temperature. This is mainly

because of the higher phase incoherence that reduces the output signal level. With an input optical power of 20μW and a cell temperature of 50°C, the actual SNR dropped to 11.6 and the actual sensitivity was 27pT/Hz$^{1/2}$, measured in a 1Hz bandwidth. The best actual sensitivity was obtained with an input optical power of 20μW at room temperature (23°C). The corresponding actual SNR was 14.5 and the actual sensitivity was 21pT/Hz$^{1/2}$, measured in a 1Hz bandwidth.

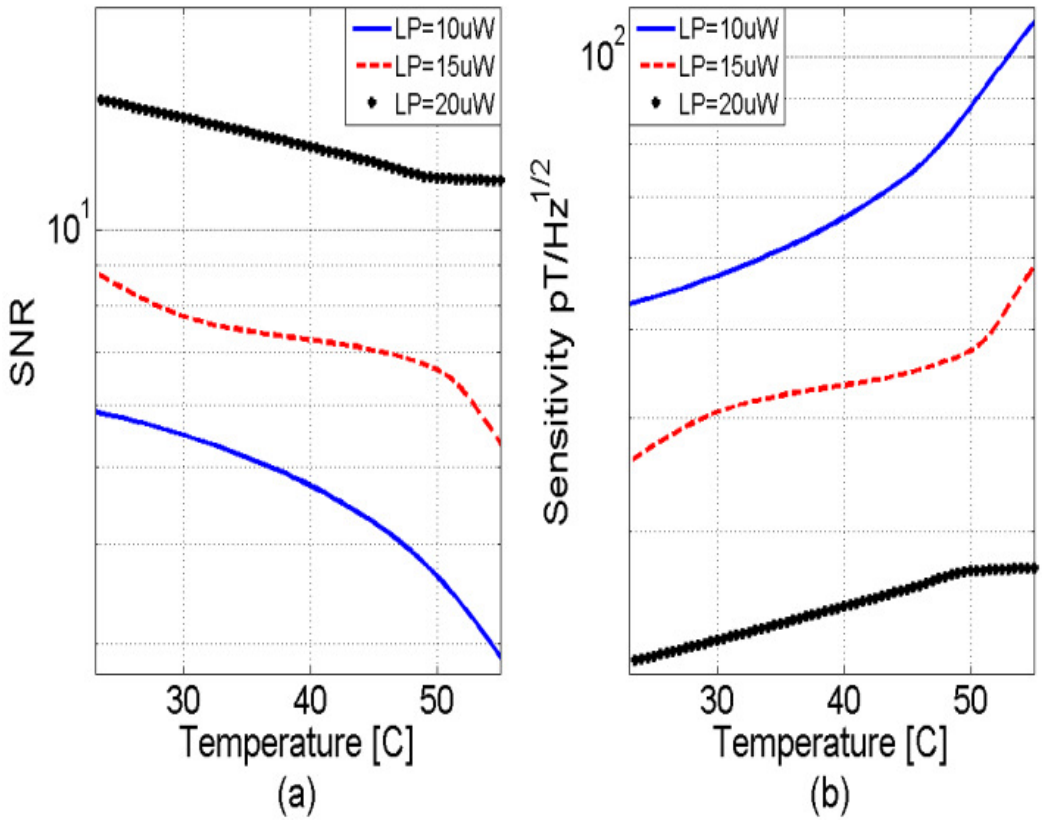

Fig.5.12: (a) Actual signal-to-noise ratio (SNR) and (b) actual sensitivity versus cell temperature, measured in a 1Hz bandwidth for an input optical light power of 10μW, 15μW and 20μW.

5.4 Bandwidth characterization

The bandwidth, f_{bw}, of the magnetometer can be calculated from Equation (3.15). The half width at half maximum (HWHM) bandwidth of the phase signal ($\Delta\nu$), measured in hertz, is illustrated in Fig.5.13 (c).

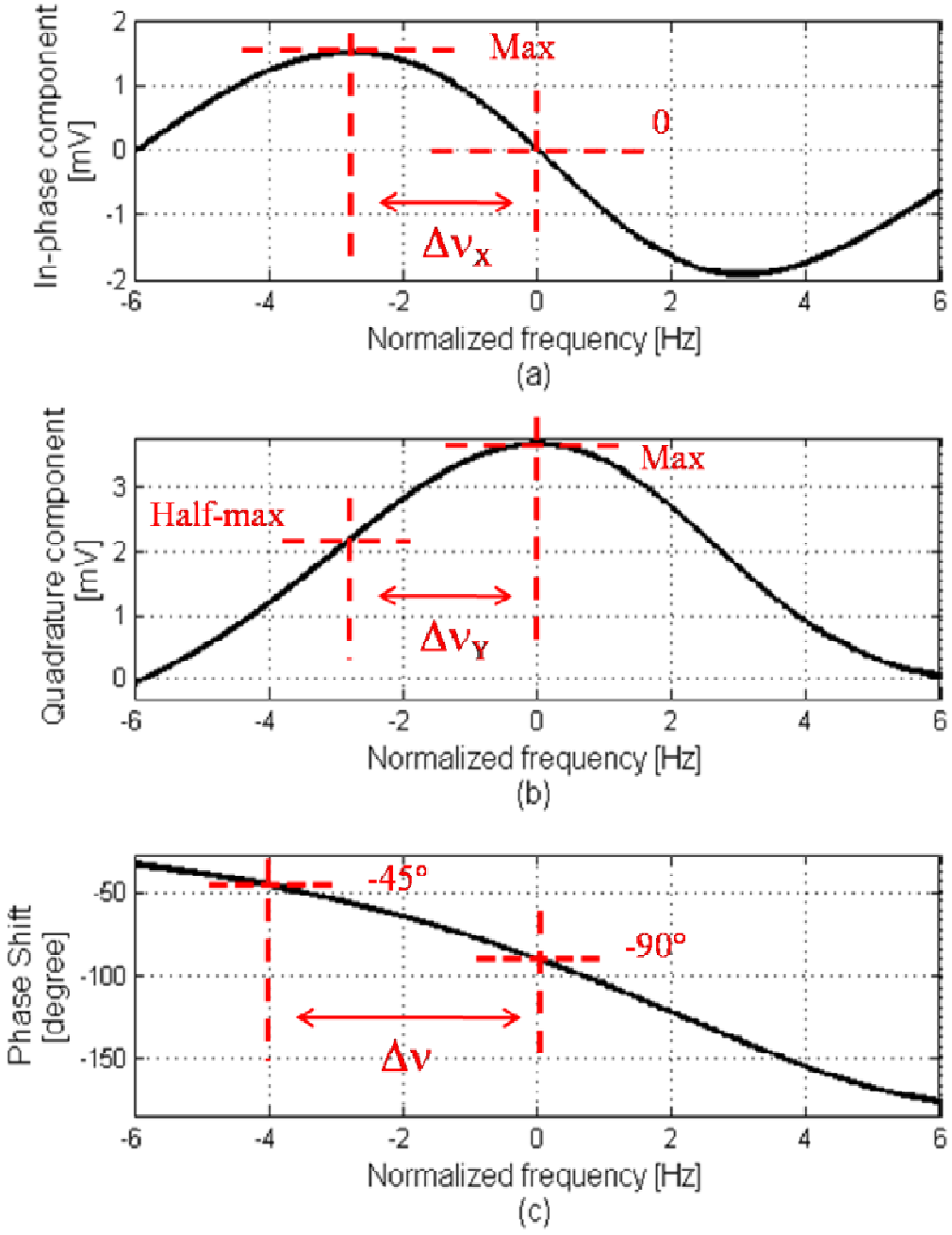

Fig.5.13: (a) Measured in-phase component; (b) quadrature component and (c) phase shift between the photo diode output and the driving rf magnetic field. All signals were measured in a magnetically unshielded environment by continuously sweeping the driving rf frequency along the resonance frequency over a 6 second time range. It is important to note that the magnetically-induced 50Hz interference signal was suppressed by a notch filter. The input optical power was 20μW and the vapour cell temperature was 48 ℃. The HWHM bandwidth is highlighted for each measured output signal.

Fig.5.13 (a) and (b) show, respectively, the in-phase and quadrature components of the lock-in amplifier output versus the normalised frequency, predicted by Equations (3.11) and (3.12). Fig.5.13 (c) shows the phase shift between the photodiode output and the driving rf magnetic field, B_{rf}, predicted by Equation (3.13). All signals in Fig.5.13 (a-c) were measured in a magnetically unshielded environment by continuously sweeping the driving rf frequency along the resonance frequency over a 6 second time range. It is important to note that the magnetically-induced 50Hz interference signal was suppressed by using a notch filter. It is obvious from Fig.5.13 (a-c) that the HWHM bandwidths of both the in-phase signal, $\Delta\nu_X$, and the quadrature signal, $\Delta\nu_Y$, are equal to each other and smaller than the HWHM bandwidth, $\Delta\nu$, of the phase-shift signal. This agrees with the theoretical prediction using Equations (11-13). In fact, the phase shift is the only signal that is not dependent on the rf magnetic field. Therefore, for the accurate evaluation of the bandwidth of the magnetometer, f_{bw}, it is important to use in Equation (3.15) the HWHM bandwidth, $\Delta\nu$, measured from the phase shift rather than the HWHM bandwidths, $\Delta\nu_X$ and $\Delta\nu_Y$, measured from the in-phase and quadrature components, respectively.

Fig.5.14 shows the magnetometer bandwidth versus cell temperature for input optical power levels of 10μW, 15μW and 20μW. The bandwidth exhibits a similar trend for all input optical power levels, initially decreasing with increasing cell temperature until reaching its minimum around 45°C. Subsequently, the bandwidth increases with increasing cell temperature. Typically, the bandwidth depends on the transverse relaxation time Γ_2, as evident from Equations (3.13) and (3.15). An increase in the cell temperature increases the vapour pressure, which results in a larger number of atoms interacting with the light, leading to a longer relaxation time (smaller bandwidth). However, at high temperatures, the number of collisions between atoms or with the walls of the cell increases significantly, leading to a shorter relaxation time and hence a larger bandwidth. This explains the existence of a critical temperature (around 45°) at which the intrinsic bandwidth is minimum.

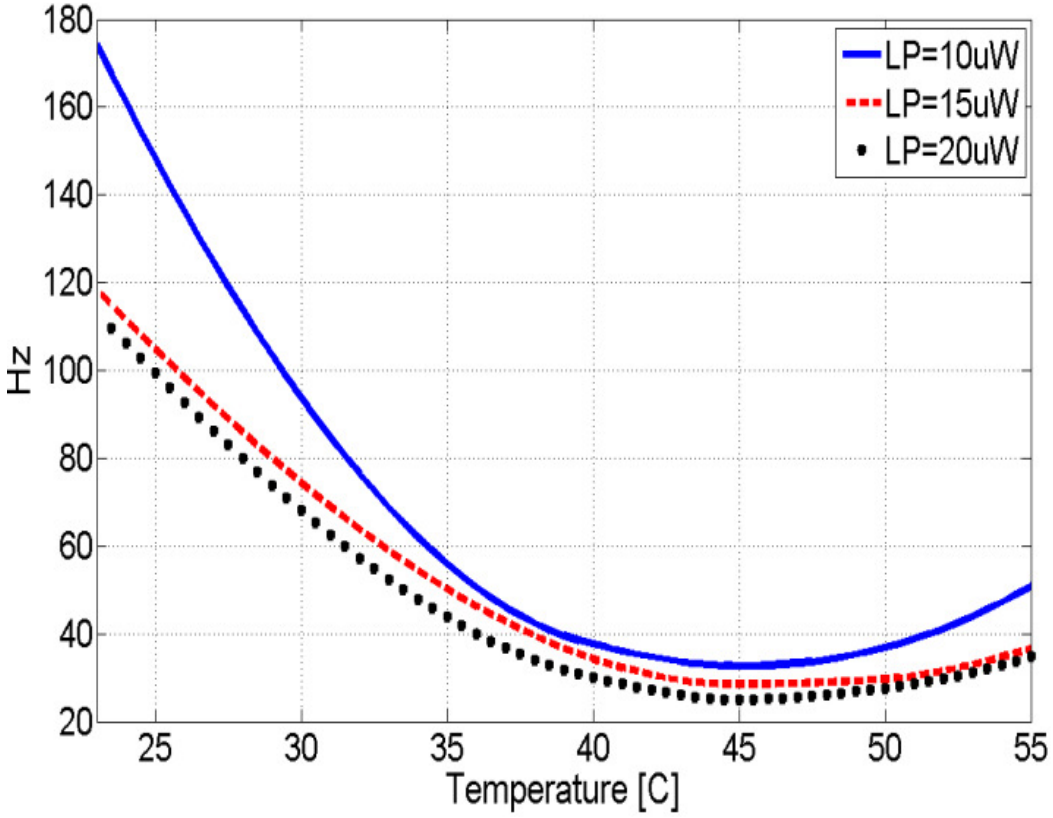

Fig.5.14: Intrinsic bandwidth versus cell temperature for an input optical light power of 10μW, 15μW and 20μW.

In the experiments, the measured maximum bandwidth was 175Hz, obtained at room temperature (23°C) with an input optical power of 10μW (blue curve in Fig.5.14), while the minimum bandwidth was 25Hz, obtained with an input optical power of 20μW at a temperature of 45°C (black curve in Fig.5.14).

5.5 Low amplitude magnetic field measurement

The ultimate intrinsic sensitivity of the magnetometer can be calculated using the bandwidth calculated with Equation (3.15) in Equation (3.14). The best performance of the magnetometer was obtained for an input optical power of 20μW at cell temperature of 48°C; the ultimate intrinsic sensitivity was 327fT/Hz$^{1/2}$, over a bandwidth of 26Hz. However, the external magnetic noise generated by power lines and surrounding equipment caused the actual ultimate sensitivity of the magnetometer to drop to 130pT/Hz$^{1/2}$, over a bandwidth of 26Hz.

The magnetometer in its optimal configuration (input optical power of 20μW at cell temperature of 48°C) was then used to measure an applied small-signal sinusoidal magnetic field of amplitude 15pT oscillating at 25Hz, which was generated by a test coil placed at a distance of 6cm from the vapour cell. For this measurement, the uniform dc magnetic field was 13μT, corresponding to a Larmor frequency of 45.5kHz. The frequency of the rf magnetic field was then set at 45.5kHz resulting in a phase shift of -90 degrees between the photodiode output and the driving rf signal, as predicted by Equation (3.13), and verified experimentally by the result shown in Fig.5.13 (c). When another 25Hz small-amplitude magnetic field was applied in addition to the dc and rf magnetic fields, the Larmor frequency changed and no more resonance occurred, causing the phase shift between the photodiode output and the driving rf signal to oscillate around -90 degrees at 25Hz. This enabled the measurement of the new Larmor frequency, and hence the calculation of the magnitude of the 25Hz small-amplitude magnetic field, which is proportional to the new Larmor frequency.

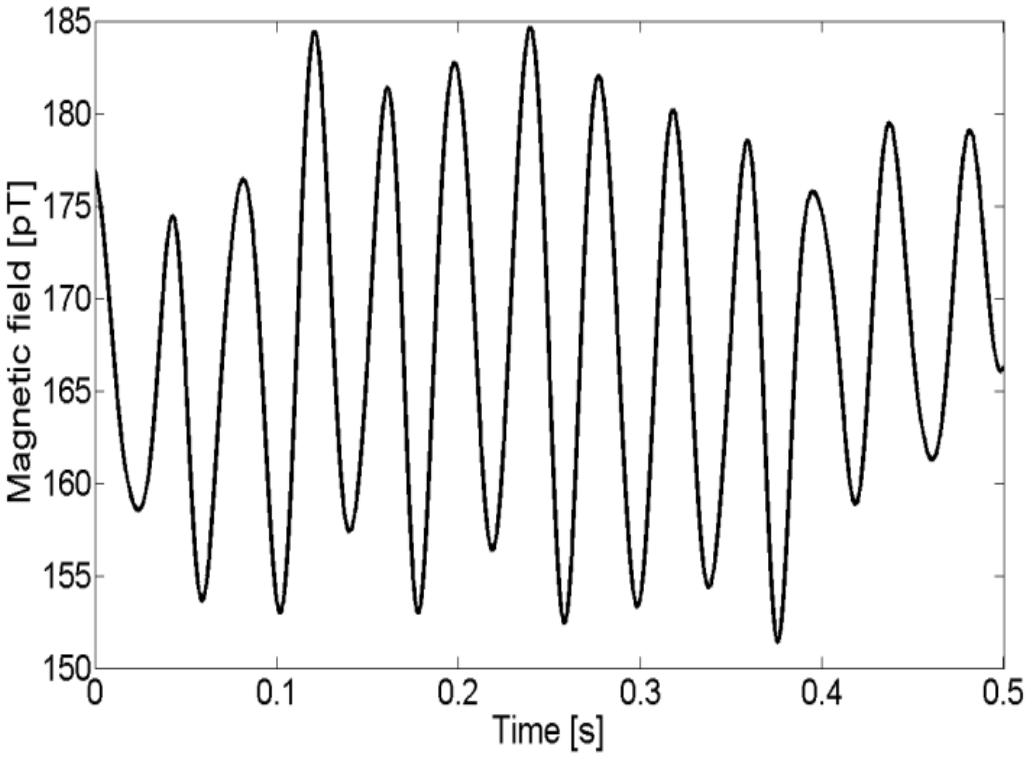

Fig.5.15: Measured 15pT peak oscillating field at frequency of 25Hz filtered with a lowpass filter with cutoff frequency of 50Hz.

Fig.5.15 shows the magnetic field calculated from the measurement of the Larmor frequency after a 25Hz 15pT magnetic field was applied. A lowpass filter with a cutoff frequency of 50Hz was used after the lock-in amplifier in order to remove the power line noise (at 50Hz and its harmonics) as well as all high frequency noise. It is evident from Fig.5.15 that the small-signal 25Hz magnetic field could be detected (peak-to-peak magnitude is around 33pT), demonstrating the capability of the optical Mx magnetometer to measure ultra-low-amplitude magnetic fields.

5.6 Summary

In this chapter the experimental setting of the developed optically-pumped quantum magnetometer has been described. In particular, the main blocks of the magnetometer have been discussed in detail. In addition, the experimental results, regarding both the dependence of the sensitivity and the frequency bandwidth of the instrument on the laser light power and vapour cell temperature, have been presented and discussed. Experimental results have shown that the best performance of the magnetometer is obtained with an input optical power of 20μW and a cell temperature of 50°C. A measured intrinsic SNR of 5000 and an intrinsic sensitivity of 63fT/Hz$^{1/2}$ have been achieved. In addition, it has been shown that environmental noise reduces the output signal level, thus dropping the actual SNR to 11.6 and the actual sensitivity to 27pT/Hz$^{1/2}$. At room temperature (23°C), an actual SNR of 14.5 and an actual sensitivity of 21pT/Hz$^{1/2}$ have been measured. Moreover, experimental results have shown that for input optical power of 10μW the maximum bandwidth of the magnetometer at room temperature (23°C) is 175Hz, and 25Hz for an input optical power of 20μW and at a temperature of 45°C. Finally, a small-signal 25Hz magnetic field of 33pT peak-to-peak magnitude has been experimentally measured, demonstrating the capability of the optical Mx magnetometer to measure ultra-low-amplitude magnetic fields.

Chapter 6

Adaptive Noise Cancellation Results

Chapter 6 presents the signals recovered by the adaptive noise cancellation system employing the algorithms introduced in Chapter 4, namely, the Least-Mean Squares (LMS) algorithm, the normalised LMS, the Genetic Algorithms and the Particle Swarm Optimization. Heart signals are extracted from simulated signals as well as from signals experimentally measured by an array configuration of the optical magnetometer optimized in Chapter 5. The experimental results and the simulation results are then compared and discussed.

6.1 Introduction

The algorithms described in Chapter 4, namely Least-Mean Squares (LMS) Algorithm, the normalised LMS (nLMS) Algorithm, the Genetic Algorithms (GA) and the Particle Swarm Optimization (PSO) Algorithm, are demonstrated in this chapter through simulation as well as experimental results. The adaptive noise canceller, shown in Fig.6.1, requires two measured input signals for recovering a weak heart signal from a much stronger noise.

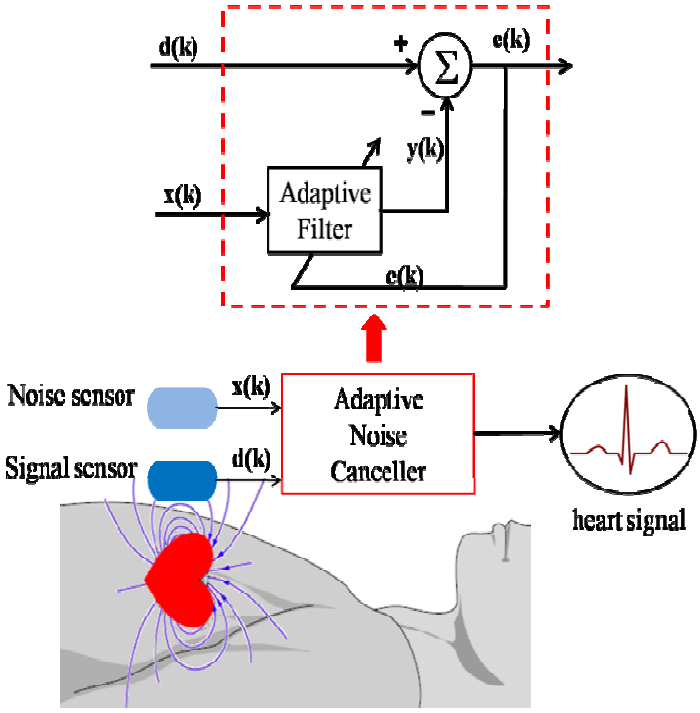

Fig.6.1: Typical block diagram of an adaptive noise canceller applied to a general magnetocardiographic system.

For the simulations, measured cardiac signals were taken from the MIT-BIH Arrhythmia Database [117, 118] and added to the environmental noise to produce the input signal of the noise canceller (signal *d(k)* of Fig.6.1). These cardiac signals were captured by electrodes placed on the surface of a patient chest. Since the magnetic field and the electric field generated by human heart have similar waveforms [119]; it is accurate to assume that the measured MCG signal has similar shape as the measured ECG signal but with amplitude of 100pT, which corresponds to a typical amplitude of a heart-generated magnetic signal. The

environmental noise was initially simulated with different intensity to test the performance of the adaptive noise canceller respect to different values of initial signal-to-noise ratio (SNR) and subsequently measured in our laboratory using a 2-axis magnetic sensor Honeywell. The noise was then linearly filtered to produce a correlated noise, which was used as the reference signal input to the noise canceller (signal *x(k)* in Fig.6.1). The simulation results were compared with experimental results, where signals measured by the optically-pumped quantum magnetometer described in Chapter 5 were used as inputs to the adaptive noise canceller.

6.2 Simulation results achieved from real cardiac signal and simulated environmental noise

6.2.1 Adaptive noise canceller input data set

The cardiac signal used was the recording 234.dat of the MIT-BIH Arrhythmia Database; it is digitized at 360 samples per second per channel with 11 bit resolution. Fig.6.2 (a) and (b), respectively, show the cardiac signal and its spectrum, which is mainly spread over low frequencies.

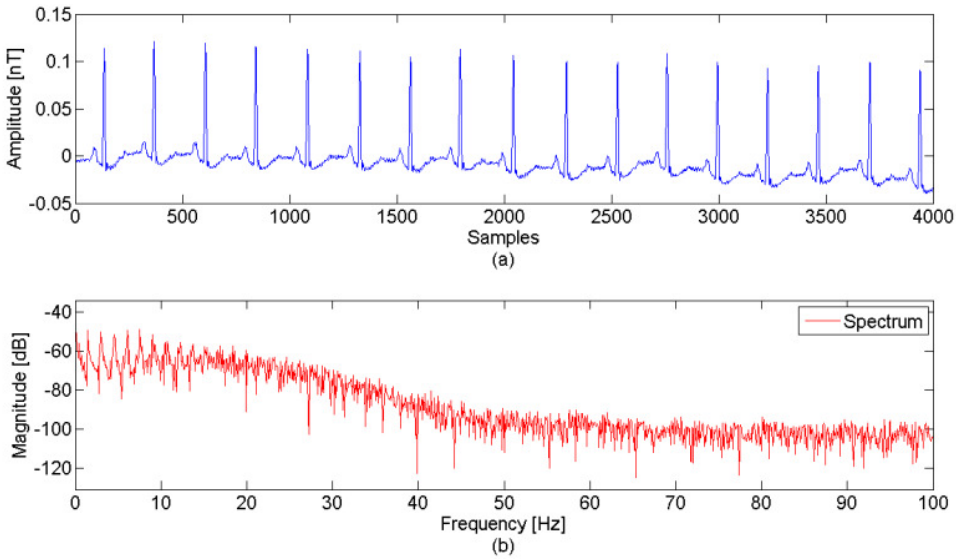

Fig.6.2: (a) Original cardiac signal 234.dat, scaled to fit a typical magnetocardiogram intensity, and (b) cardiac signal spectrum.

The noise signal was simulated as the sum of two components, namely, a sinusoid of 60Hz frequency, which accounts for the power line interference, and a random noise with a standard uniform distribution, which accounts for white noise attributed to the noise generated by electronic devices and other wireless-related noise sources. This noise was linearly filtered to produce a correlated noise which was used as the reference signal input to the noise canceller, shown in Fig.6.1.

Three techniques, namely, LMS, nLMS and GA, were investigated and compared to one another on the basis of: (i) signal-to-noise ratio (SNR) improvement; (ii) 60Hz noise cancellation and (iii) ability to detect peaks. The SNR improvement was calculated for three SNR initial values: (i) -9.2913dB, which is the typical value of ECG noise cancellation, (ii) -29.291 and (iii) -49.291, which are SNR values compatible with MCG applications. In our simulations, we used 4000 samples to represent the cardiac signal and the noise. The order of the FIR filter used was 7; the step size was 0.001 for LMS and 1 for nLMS.

6.2.2 Simulation results

The performances of the algorithms were firstly compared on the basis of SNR improvement. The difference between the SNR calculated before the noise canceller and the SNR calculated after noise cancellation was considered as the improvement factor that results from the noise canceller. This improvement factor varied depending on the techniques used for filter coefficients adaption. Fig.6.3 shows the improvement in the SNR after the adaptive noise canceller based on each algorithm calculated for three different input SNR values. For a starting input SNR of -9.29dB, LMS and nLMS achieved improvement factors of 36.099dB and 35.627dB respectively, whereas the GA resulted in an improvement factor of 20.196dB. As the noise increased the improvement factors of the LMS and nLMS algorithms dropped, while the GA algorithm attained better improvement factor. For a starting SNR value of -49.291 dB, the LMS and nLMS algorithms provided negative SNR values after the adaptive noise cancellation. However, the improvement factor was around 36dB for both algorithms, whereas the GA

exhibited an improvement factor of 51.155dB with the SNR of 1.8645dB after filtering.

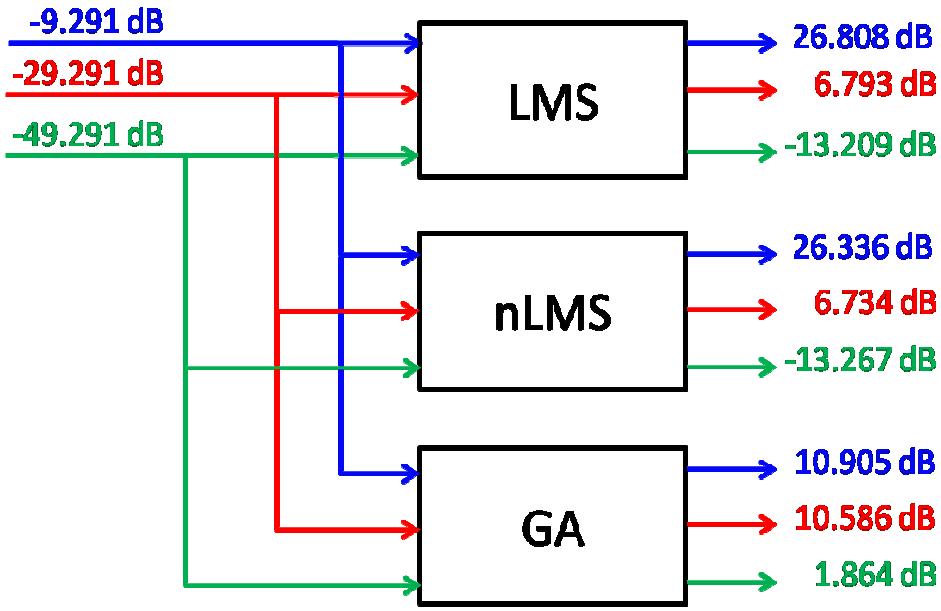

Fig.6.3: SNR improvement factors achieved by the adaptive noise canceller based on the different algorithms: LMS, nLMS and GA. In the top left the three starting SNR values are listed in different colours, in the right the improvement factors are listed for each algorithm.

The three algorithms were then tested in their ability of cancelling the 60Hz noise component when the SNR measured at the input of the adaptive noise canceller was -49.291dB. Fig.6.4 (a) shows the spectrum of the noisy cardiac signal, where the noise component at 60Hz is clearly visible. Fig.6.4 (b), (c) and (d) show the spectra of signals after noise cancellation using the LMS, nLMS and GA techniques respectively. Comparing these signal spectra with the signal spectrum in Fig.6.2 (b), it is clearly seen that the component at 60Hz was not completely suppressed by either the LMS algorithm or nLMS algorithm; however, it was suppressed by the GA algorithm, which provided the best performance for removing the noise sources at 60Hz and at low frequencies.

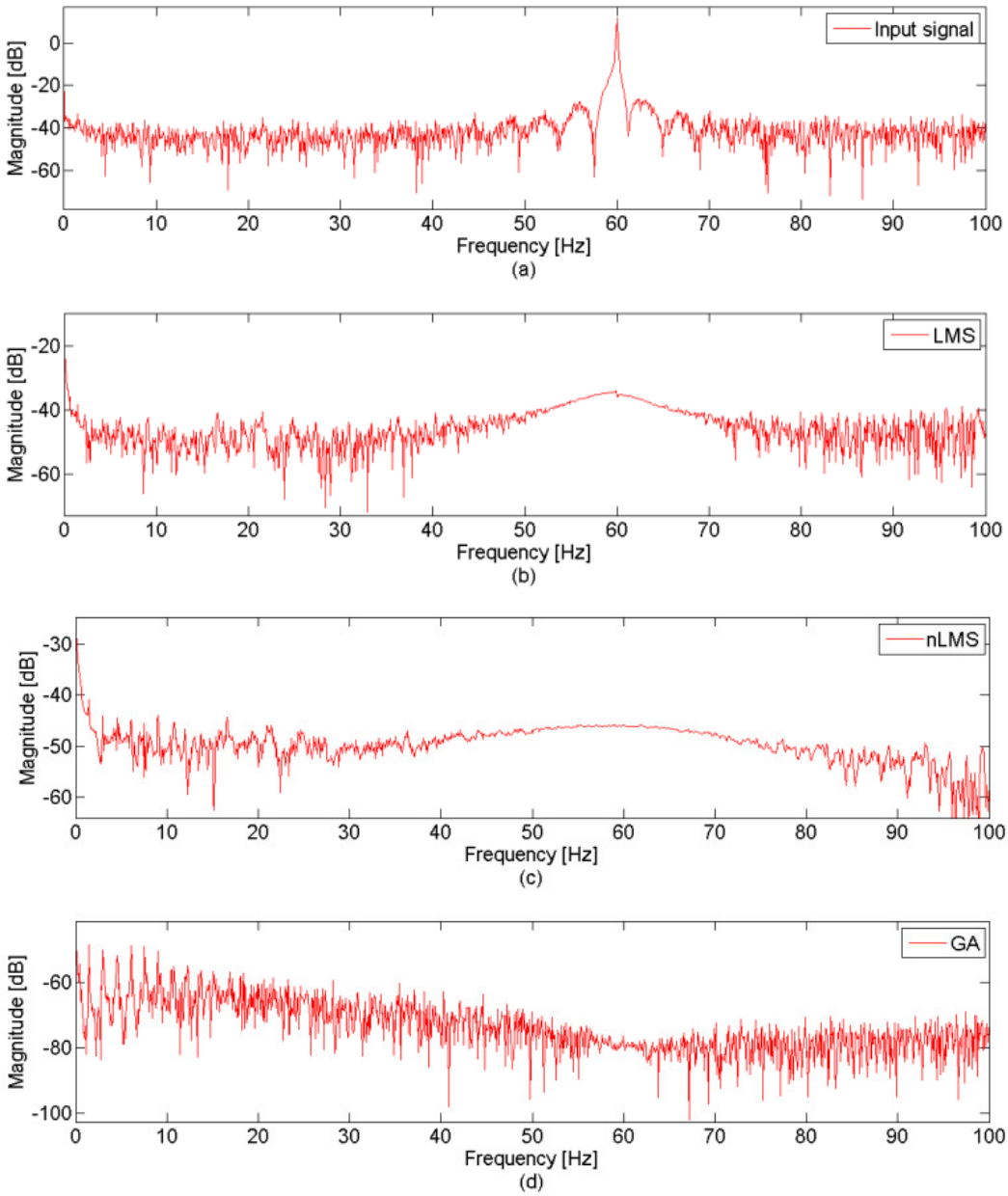

Fig.6.4: (a) Spectrum of corrupted signal before filtering. Spectra of signals after the adaptive noise cancellation based on (b) LMS, (c) nLMS and (d) GA.

Finally, Fig.6.5 (a-c) show the signals recovered using the noise canceller for all adaptive techniques when the SNR measured at the input of the adaptive noise canceller was -49.291dB to compare their capability of detecting peaks. It is obvious that the LMS algorithm is not suitable for peak detection, whereas both the nLMS and GA algorithms can recover the signal peaks, and hence they can perform peak detection which allows accurate calculation of the heart rate.

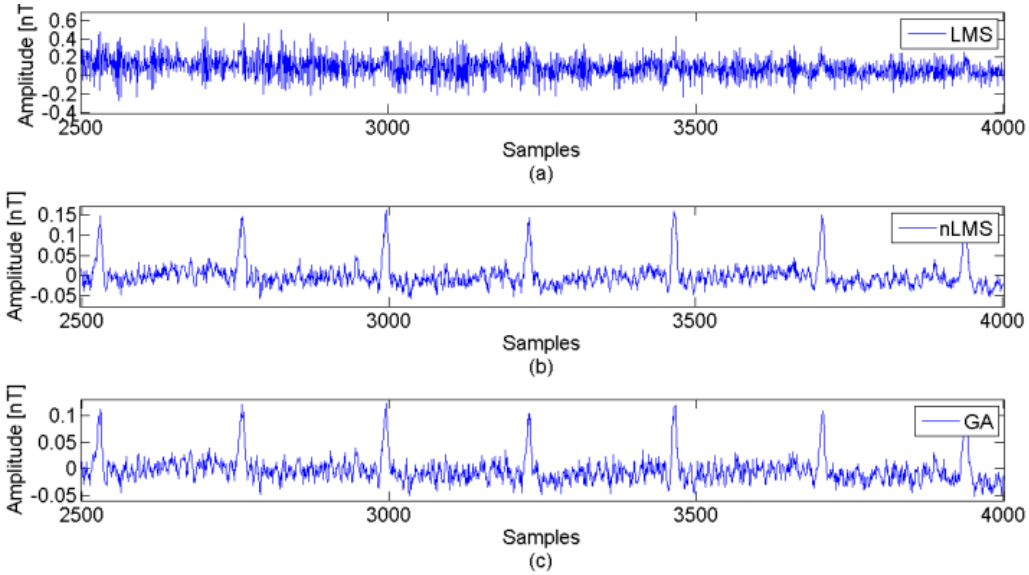

Fig.6.5: Signals de-noised by (a) LMS, (b) nLMS and (c) GA.

6.3 Simulation results achieved from real cardiac signal and measured environmental noise

6.3.1 Adaptive noise canceller input data set

The cardiac signal used was the recording 220.dat of the MIT-BIH Arrhythmia Database; digitized at 360 samples per second per channel with 11 bit resolution. Fig.6.6 (a) shows the heart signal with the typical cardiac features, namely, P wave, QRS complex and T wave, which correspond to atrial depolarization, ventricular depolarization and ventricular repolarization, respectively. The environmental magnetic noise was measured in our laboratory. The measured environmental noise was due to two main sources, namely, the dc magnetic field of the earth and the magnetic noise caused by alternating signals generated by surrounding equipment in the laboratory. It is also noted that the magnetic noise is more than 10 times higher than the heart signal shown in Fig.6.6 (a). The signal-to-noise ratio (SNR) was -35.8dB, calculated by integrating the measured signal and noise powers over several signal periods. The environmental magnetic noise was added to the heart signal to produce the input signal of the noise canceller. This signal is shown in Fig.6.6 (b). The environmental magnetic

noise was also linearly filtered to produce a correlated noise which was used as the reference signal input to the noise canceller, as illustrated in Fig.6.1.

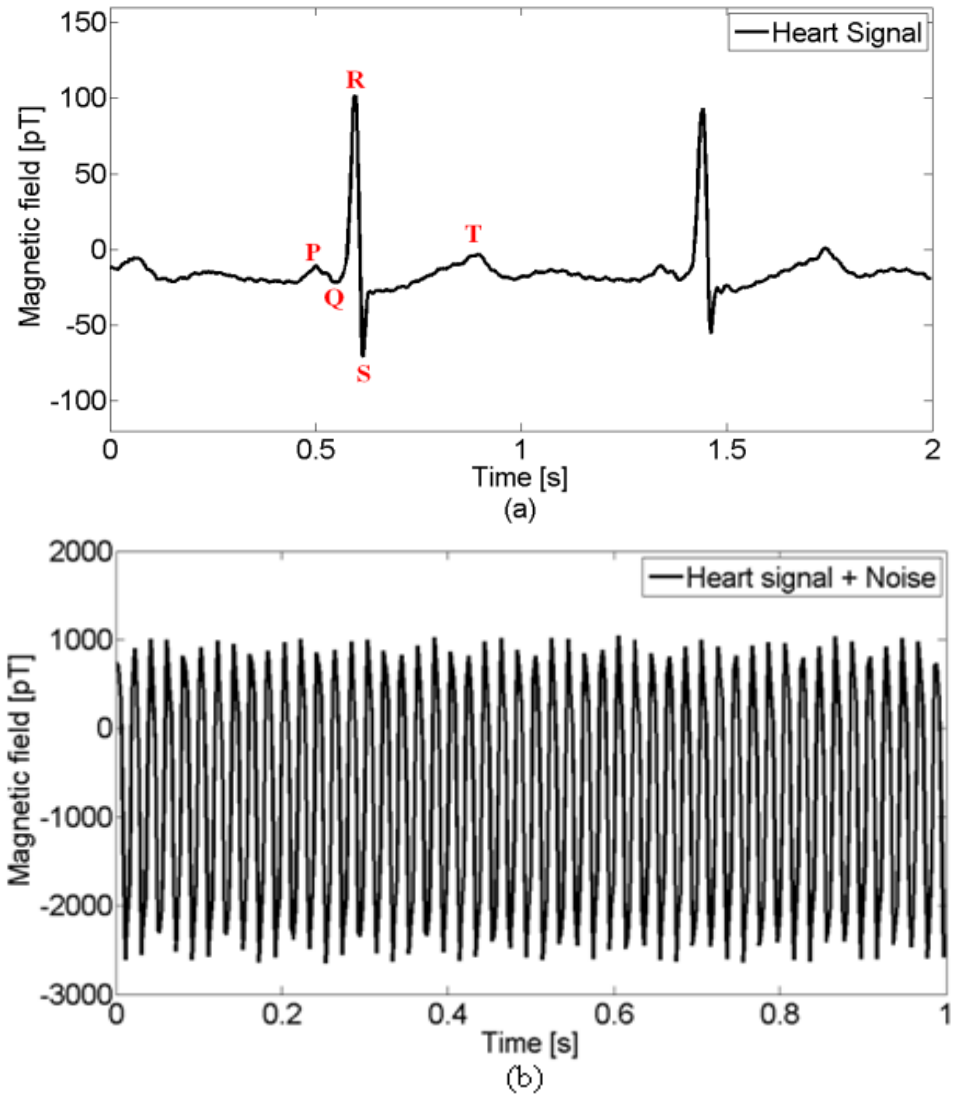

Fig.6.6: (a) Measured heart signal showing the typical P wave, QRS complex and T wave, which correspond to atrial depolarization, ventricular depolarization and ventricular repolarization, respectively; (b) Input signal of the noise canceller obtained by adding the heart signal to the environmental magnetic noise measured inside the laboratory.

Fig.6.7 (a) shows the cardiac spectrum that is mainly spread over low frequencies, while Fig.6.7 (b) shows the spectrum of the input signal of the noise canceller. It is noticed that the heart spectrum was completely encircled by the

noise; particularly strong noise peaks were exhibited at dc and 50 Hz whereas the other dominant peaks at the 60 Hz, 100 Hz and 150 Hz had lower levels.

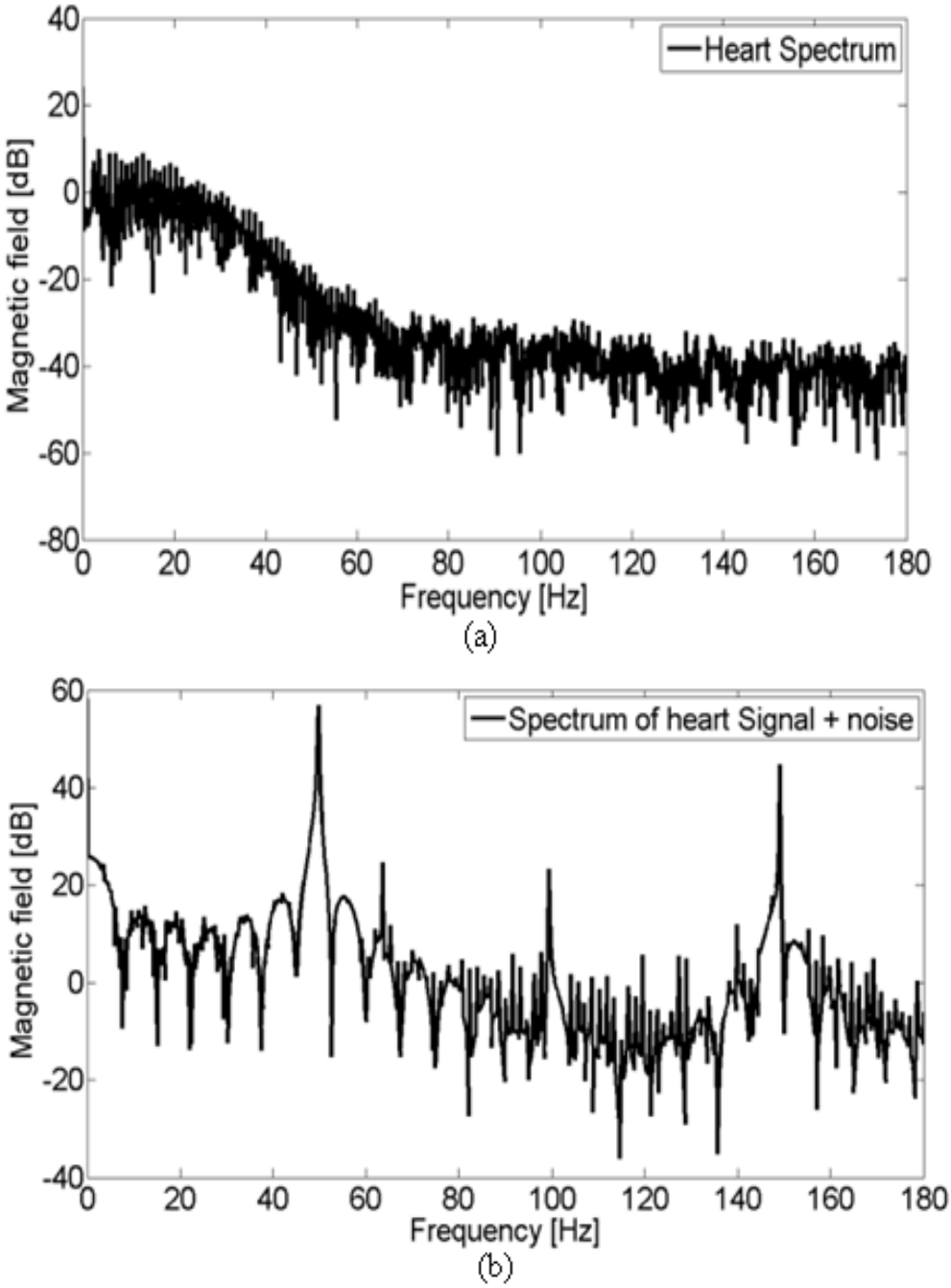

Fig.6.7: (a) Spectrum of the heart signal; (b) Spectrum of the input signal of the noise canceller, exhibiting a strong peak at 50 Hz and weaker peaks at 60 Hz 100 Hz and 150 Hz.

6.3.2 Simulation results

The simulated heart signals and the measured magnetic noise described in the previous paragraph are then used to compare the performances of adaptive noise canceller employing LMS and GA algorithms in terms of SNR improvement and heart peaks reconstruction.

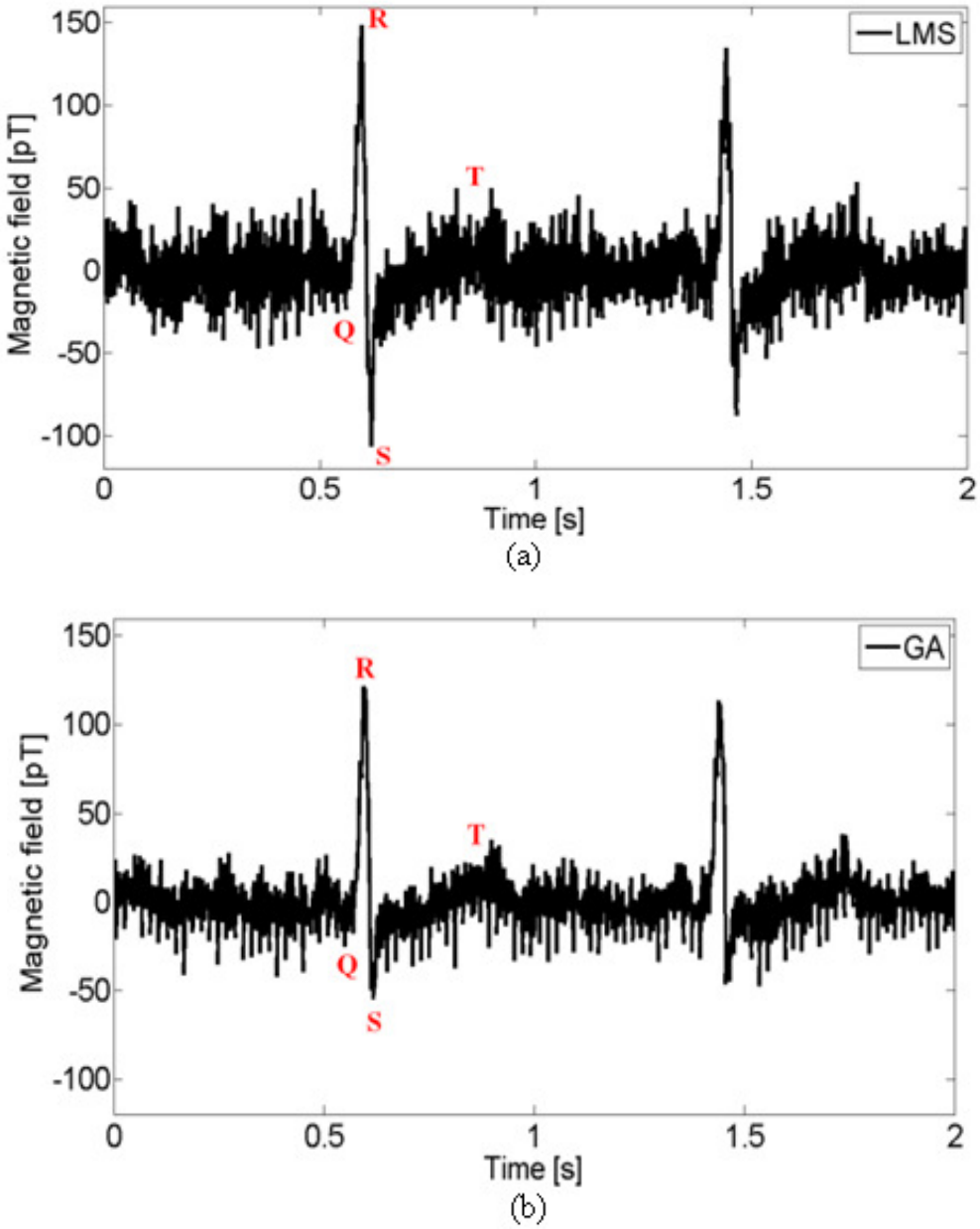

Fig.6.8: (a) Heart signal recovered by LMS algorithm, calculated SNR improvement factor was 33dB;(b) Heart signal recovered by GA algorithm, calculated SNR improvement factor was 37.4dB.

The LMS algorithm produced a SNR improvement of around 33dB while for the GA algorithm the improvement in SNR was 37,4dB. Fig.6.8 (a) and (b) show the heart magnetic signal recovered using the LMS and GA algorithms, respectively. It is obvious that for both recovered signals the QRS and T features are noticeable, whereas the heart magnetic signal recovered by the LMS algorithm is noisier, making the QRS complex and the T wave hardly detectable.

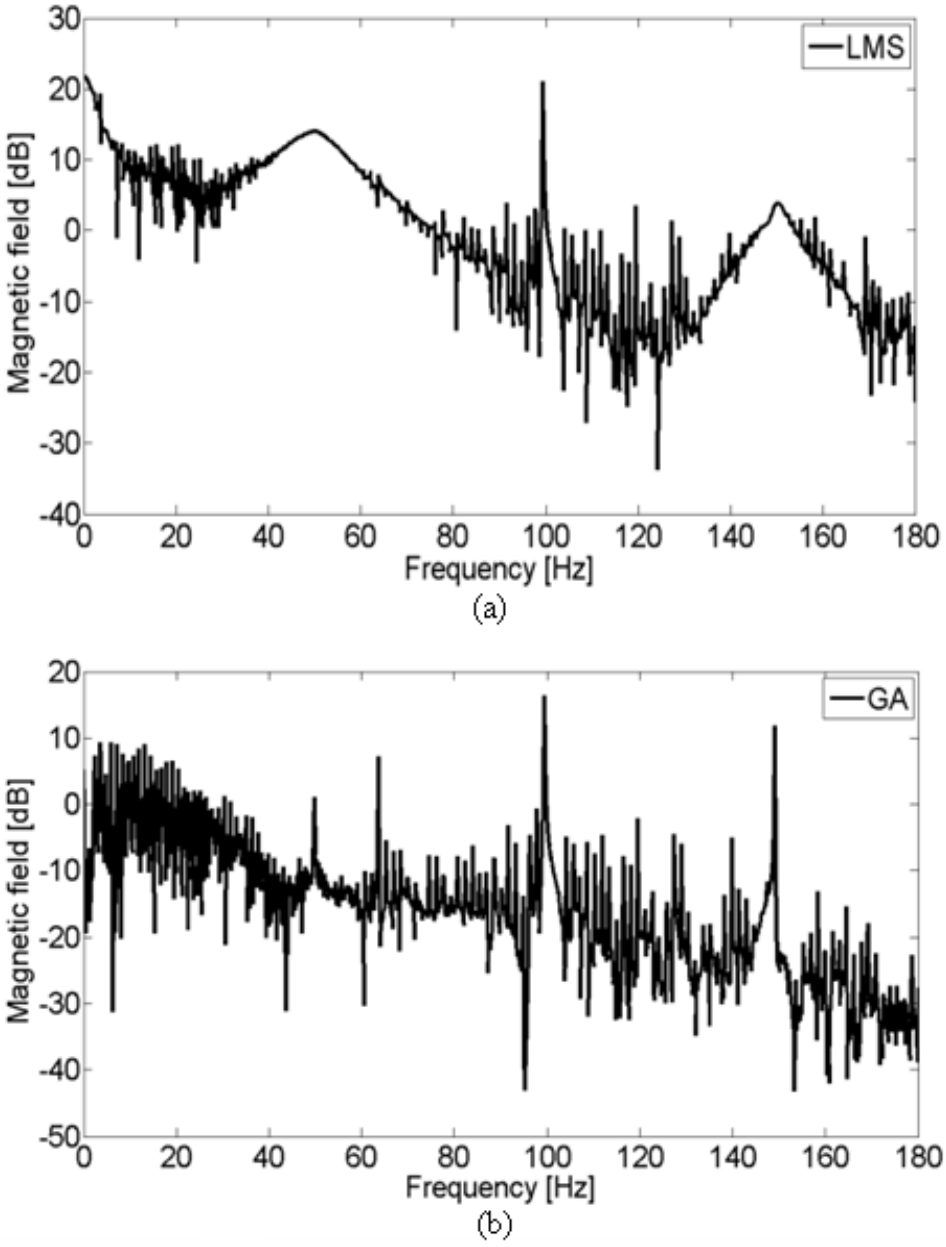

Fig.6.9: (a) Spectrum of the heart signal recovered by the LMS algorithm;(b) Spectrum of the heart signal recovered by the GA algorithm.

Fig.6.9 (a) and (b) show the spectra of the heart magnetic signals recovered by the LMS and GA algorithms, respectively. As seen from the results, the GA algorithm outperformed the LMS algorithm at low frequencies, strongly reducing the noise. It is also important to notice that both algorithms were unable to completely cancel the noise at high frequencies; however, this is not crucial as most of the signal information lies in the low-frequencies range.

6.3.3 Adaptive noise cancellation based on heuristic algorithms: genetic algorithms versus particle swarm optimization.

Since the adaptive noise canceller based on a heuristic algorithm (Genetic Algorithm) was shown from previous results to be more efficient in 50Hz component interference suppression and cardiac peaks detection respect to adaptive noise cancellation employing LMS based algorithms, another heuristic technique, namely Particle Swarm Optimization (PSO), was investigated. Simulated and measured heart signals and magnetic noise were used to compare the performances of both PSO and GA algorithms in terms of SNR improvement and CPU utilization time.

The simulated heart signal and measured environmental noise, described in paragraph 6.3.1 and shown in Fig.6.6 (a and b), were used to investigate the behaviour of both algorithms at the varying of two parameters, namely, the maximum number of iterations and the population size. In our simulations, 2000 samples were used for the representation of the cardiac signal and the magnetic noise and a 6^{th} order Finite Impulse Response (FIR) adaptive filter was used in the adaptive noise cancellation. Since both GA and PSO are heuristic algorithms and they do not provide identical results after all simulation runs, 100 simulations were carried out and the results were averaged to minimize the simulation errors.

The mean values and the standard deviations of the simulated SNR improvement factor versus the number of iterations for different population sizes are shown for both the PSO and GA algorithms in Fig.6.10 (a and b) and Fig.6.10 (c and d), respectively. It is obvious that, the PSO algorithm produces higher SNR improvement (almost 40 dB) than that of the GA algorithm (less than 35 dB), after 150 iterations. In addition, the standard deviation of the SNR improvement

generated by the PSO algorithm is lower than that generated of the GA algorithm especially at iteration numbers exceeding 100, making the PSO algorithm more practical than the GA algorithm in extracting a small heart signal from a much-stronger magnetic noise.

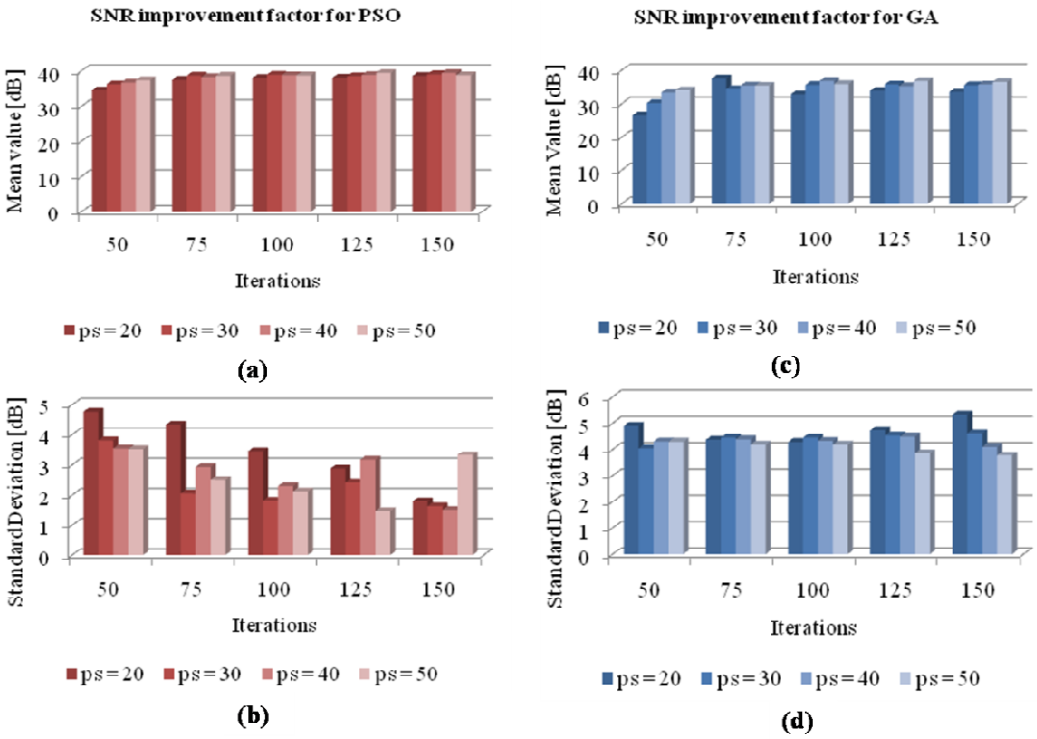

Fig.6.10: (a) Mean value and (b) standard deviation of SNR improvement versus number of iterations for different population sizes (ps), using the PSO algorithm. (c) Mean value and (d) standard deviation of SNR improvement versus number of iterations for different population sizes (ps), using the GA algorithm. Results were averaged over 100 simulation runs.

Fig.6.11 (a and b) show the measured average CPU utilization time for the PSO and the GA algorithms, respectively. For both algorithms, the CPU utilization time increases when the population size or the iterations number increase. However, the GA algorithm requires a CPU utilization time always higher than that of the PSO algorithm. This means that the use of the PSO algorithm leads to a higher convergence speed in comparison with the GA algorithm. This is also validated by investigating the mean squared error (MSE) of

the output signal versus the number of iterations generated by the PSO and GA algorithms, shown in Fig.6.12. For a population size of 30, the PSO algorithm finds an optimum value after 60 iterations, whereas the GA algorithm obtains an optimum solution exhibiting a higher MSE and hence a lower SNR improvement.

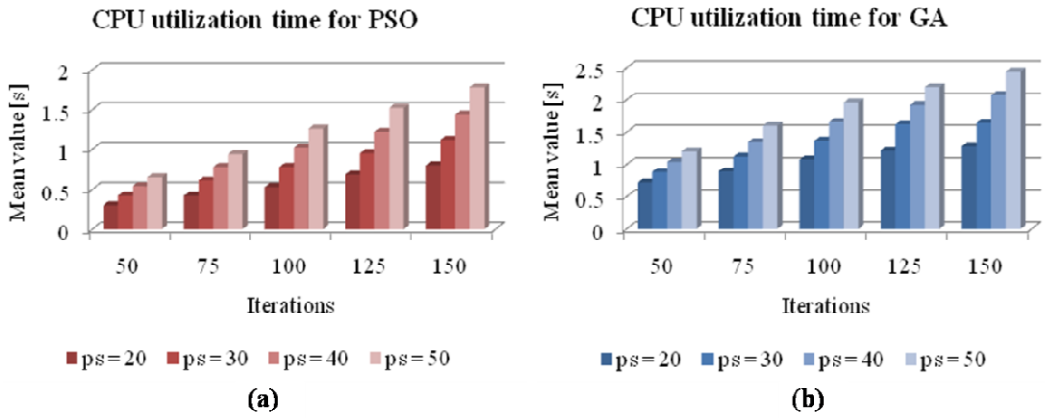

Fig.6.11. Mean value of CPU utilization time versus number of iterations for different population sizes (ps), using (a) the PSO and (b) the GA algorithms, respectively. Results averaged over 100 simulation runs.

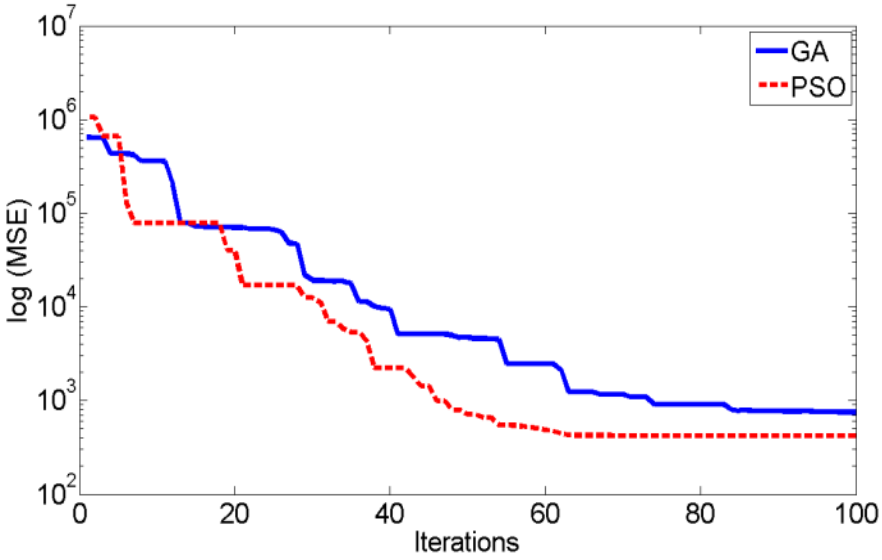

Fig.6.12. MSE versus iteration number for the GA and PSO algorithms for a population size of 30.

Fig.6.13 (a and b) show the heart magnetic signal recovered using the PSO and GA algorithms, respectively. It is obvious that for the signal recovered by the PSO algorithm, all P, QRS, and T features are detectable, whereas the heart magnetic signal recovered by the GA algorithm is more noisy, preventing the identification of the P wave, and hardly recognizing the QRS complex and the T wave. Fig.6.13 (c and d) show the spectra of the heart magnetic signals recovered by PSO and GA algorithms, respectively. It is important to notice that both algorithms are unable to completely cancel the noise at high frequencies; however, this is not crucial as most of the signal information lies in the low-frequencies range.

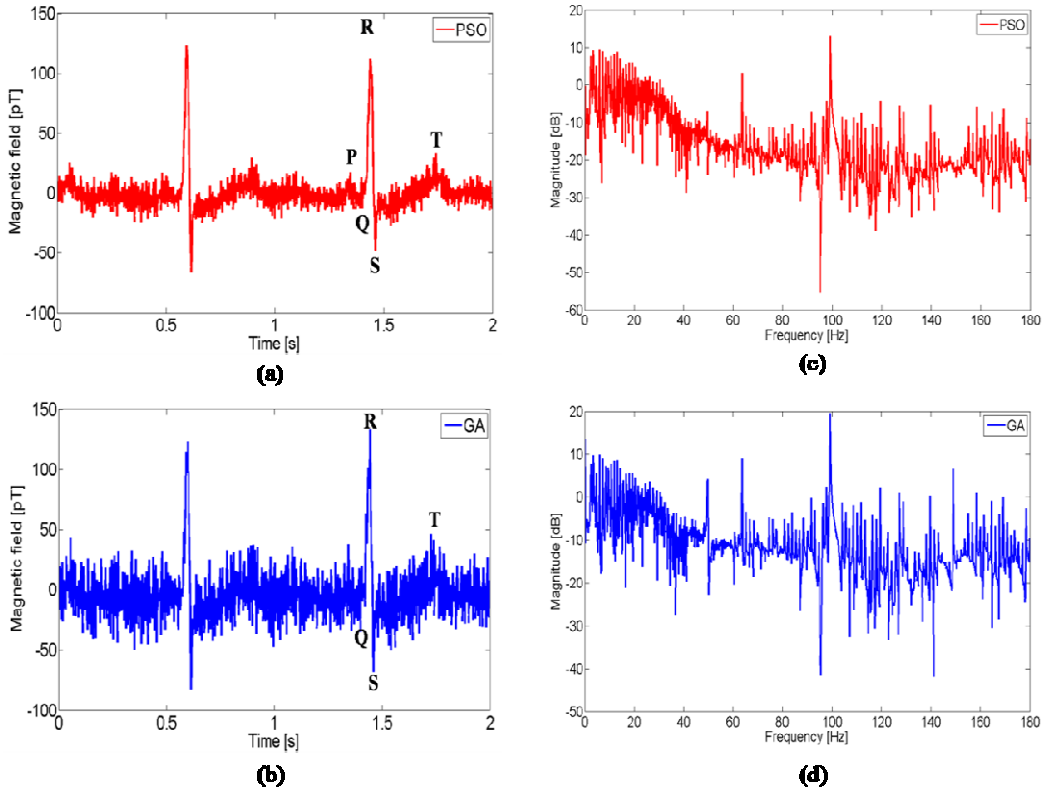

Fig.6.13: (a) Heart signal recovered by PSO algorithm (calculated SNR improvement factor was 38.4 dB); (b) heart signal recovered by GA algorithm (calculated SNR improvement factor was 36.3 dB); (c) spectrum of the heart signal recovered by the PSO algorithm and (d) spectrum of the heart signal recovered by the GA algorithm. Population size = 30 and maximum number of iterations = 100.

6.4 Experimental results

6.4.1 Experimental setup

We adopted the Mx magnetometer configuration shown in Fig.6.14, through an experimental setup, which is similar to that described in Chapter 5 with the addition of one cell that senses the environmental noise.

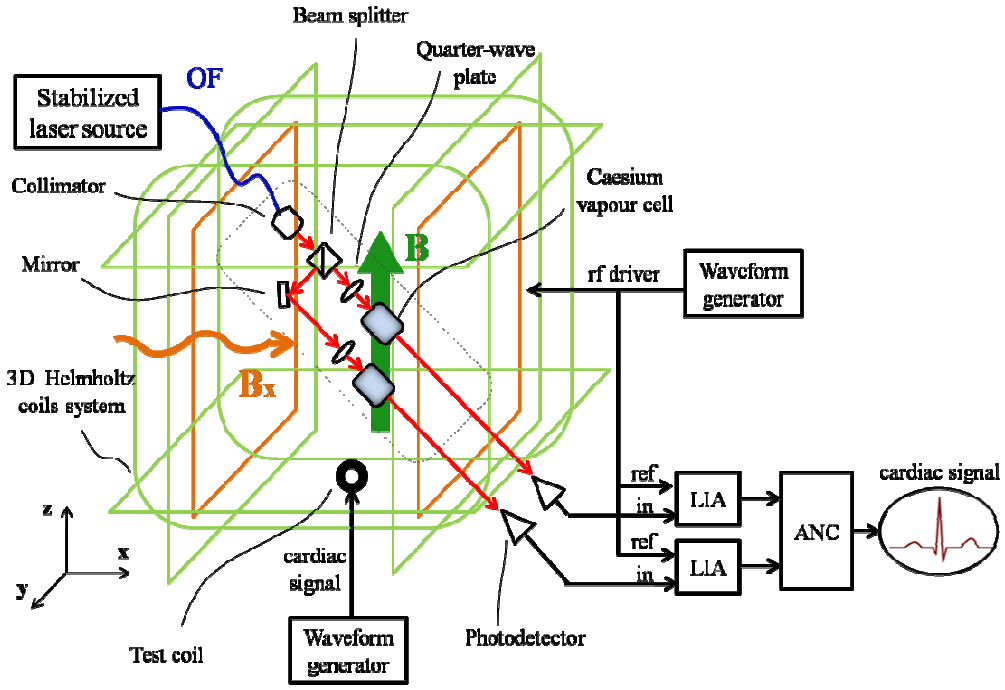

Fig.6.14: Experiment setup used to demonstrate the principle of the proposed optical magnetometer.

A test coil was placed inside the electromagnet system to simulate the human heart activity. The distance between the test coil and the centre of the vapour cell was 5cm. A waveform generator was used to produce a cardiac signal and drive the test coil. The distance between the cells was made 10cm to assure that the reference cell is not affected by the cardiac signal. The temperature of the vapour cells was increased to 37°C, which corresponds to the typical human body temperature. The frequency of the generated cardiac test field was 1.2Hz, which corresponds to the typical human heart rate of 70 beats per minute.

It is important to mention that all the experimental results reported below were performed in laboratory environment without any magnetic shield. Typical optical magnetometers operate in phase-locked modes with a feedback loop implemented between the lock-in amplifier phase output and the driver of the ac coils. Specifically, the rf frequency is locked to the cell that measures the environmental noise [120]. This approach enables the signal measured by the close-to-the-heart cell to sense the change due to the heart field only with minimum noise contamination. Our novel approach is based on operating the Mx magnetometer in a free-running mode without the use of feedback between the lock-in amplifier and rf driver, thus maintaining a high-level of correlation between the noisy signal and noise reference, and making noise cancellation more efficient in accurately recovering the heart signal. A heart signal typically spreads over a bandwidth of at least 60Hz. The main problem in the proposed free-running mode configuration of the Mx magnetometer was the limited bandwidth of the magnetometer. This issue was overcome by setting the time constant of the output filter of the lock-in amplifier to 1 second. The process that was used for the extraction of the heart signal from the noise was based on (i) recording the phase shift signals from the lock-in amplifiers over a period of around 5 seconds, (ii) processing the recorded signals offline using the different algorithms to recover the heart signal, (iii) repeating steps (i) and (ii) for different time periods (more than 50 times), and (iv) calculating the average of the extracted signals to obtain the final heart signal.

6.4.2 Measured signal and noise

Fig.6.15 (a) shows the waveform of the generated heart signal where the typical cardiac features are clearly displayed, namely, P wave, QRS complex and T wave, which correspond to atrial depolarization, ventricular depolarization and ventricular repolarization, respectively. Fig.6.15 (b) shows the spectrum of the cardiac signal that typically spreads over low frequencies, exactly between DC to 60Hz. Fig.6.15 (c and d) show the waveform and corresponding spectrum of the signal detected by the sensor that was close to the heart, named Signal Sensor in

Fig.6.1. Fig.6.15 (e and f) display the waveform and corresponding spectrum of the reference noise detected by the other sensor, named Noise Sensor in Fig.6.1.

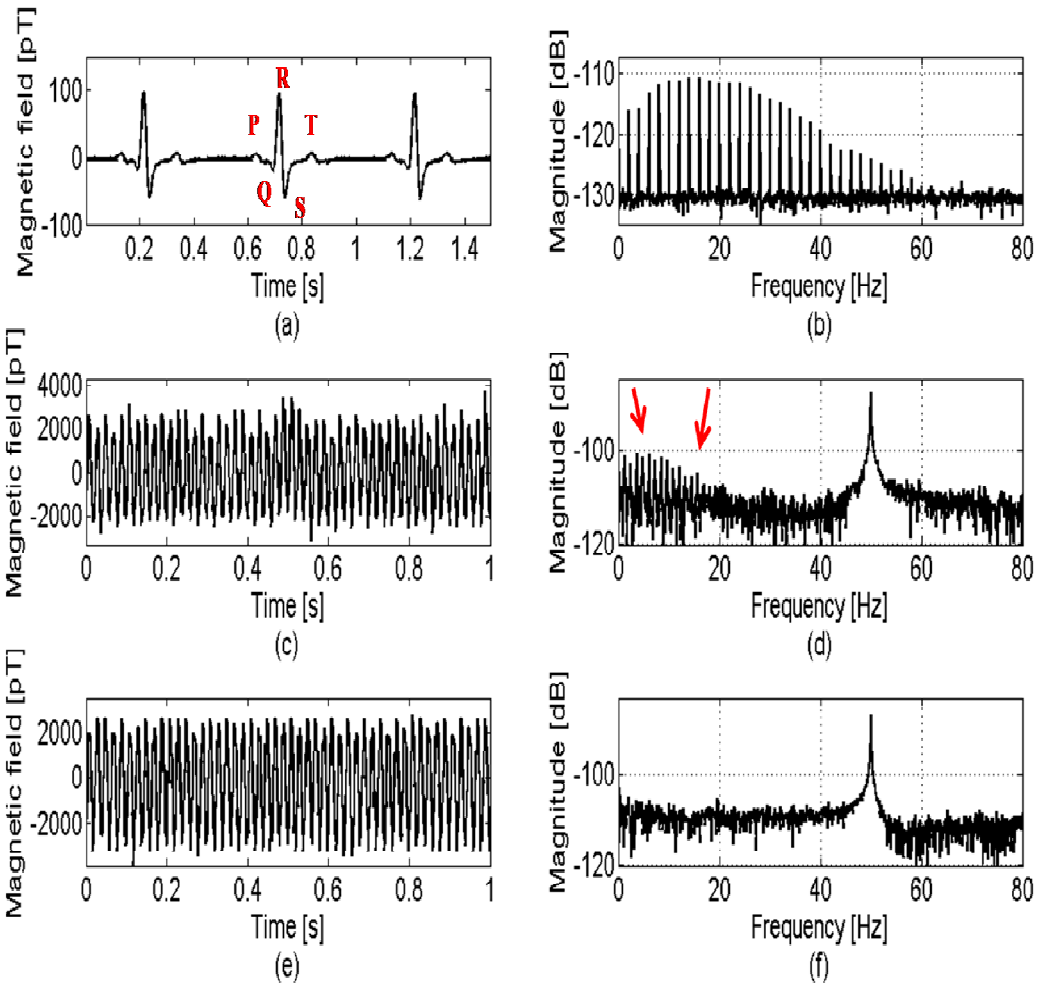

Fig.6.15: (a) Heart signal generated using a heart waveform generator. The typical P wave, QRS complex and T wave, are clearly displayed, which correspond to atrial depolarization, ventricular depolarization and ventricular repolarization, respectively; (b) spectrum of the generated heart signal, which is mainly concentrated at low frequencies (from DC to 60Hz); (c) signal measured by the sensor close to the heart; (d) spectrum of the signal measured by the sensor closest to the heart (red arrows point to the low-frequency components of the heart signal); (e) noise measured by the reference sensor and (f) spectrum of the noise measured by the reference sensor.

The waveforms shown in Fig.6.15 (c and e) are the main input signals needed to recover the heart signal by the noise cancellation algorithm. From Fig.6.15 (c), it is obvious that the noise is much stronger than the heart signal, making the heart beat unremarkable. As shown in Fig.6.15 (d and f), the main source of noise in the frequency range of interest is the interference at 50 Hz produced by power lines. However, the low-frequency components of the heart signal are clearly seen in Fig.6.15 (d) (pointed to by the red arrows). Since the heart signal is concentrated in the DC-60Hz range, both inputs of the noise canceller were filtered using a low pass filter with a cutoff frequency of 90 Hz.

6.4.3 Signals recovered by the noise canceller employing LMS based algorithms

The cardiac signal was initially recovered from the measured noisy signal by the adaptive noise canceller using the LMS and normalised LMS algorithms. The two algorithms are tested and compared on their ability to suppress the interference at 50Hz and on their capability to identify all the cardiac features, namely, the P wave, the QRS complex and the T wave.

Fig.6.16 (a and b) show the cardiac signal extracted from the signals displayed in Fig.6.15 (c and e) using the adaptive noise canceller based, respectively, on (a) LMS algorithm and (b) normalised LMS algorithm. It is important to note that the results shown in Fig.6.16 were averaged over 50 measurements. Both the LMS algorithm and the normalised LMS algorithm were capable of clearly detecting the QRS complex, enabling the prediction of the heart rate. Note that the P and T waves were better identified with the normalised LMS algorithm.

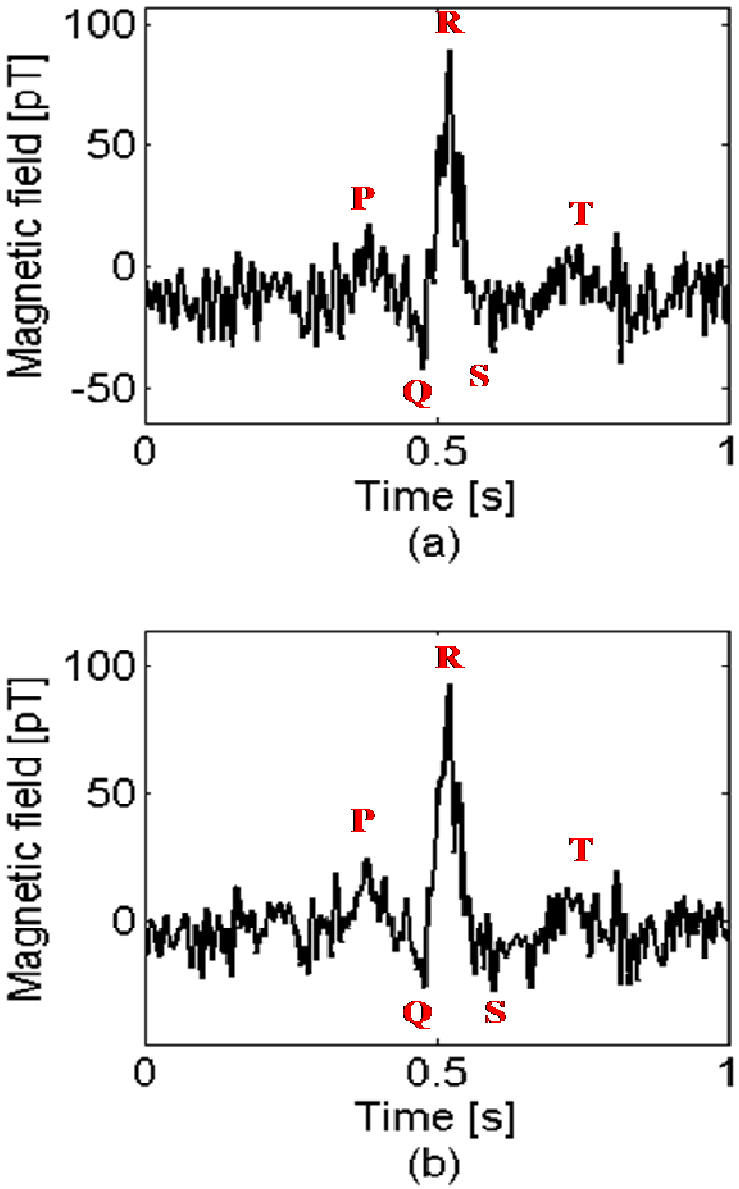

Fig.6.16: Magnetic heart signals extracted by (a) LMS algorithm and (b) normalised LMS algorithm.

Fig.6.17 (a and b) show the spectra of the heart signals recovered by the LMS algorithm and the normalised LMS algorithm, respectively. It is obvious that while both algorithms successfully recovered the heart waveform, the normalised LMS algorithm outperformed the LMS algorithm in cancelling the noise component at 50Hz.

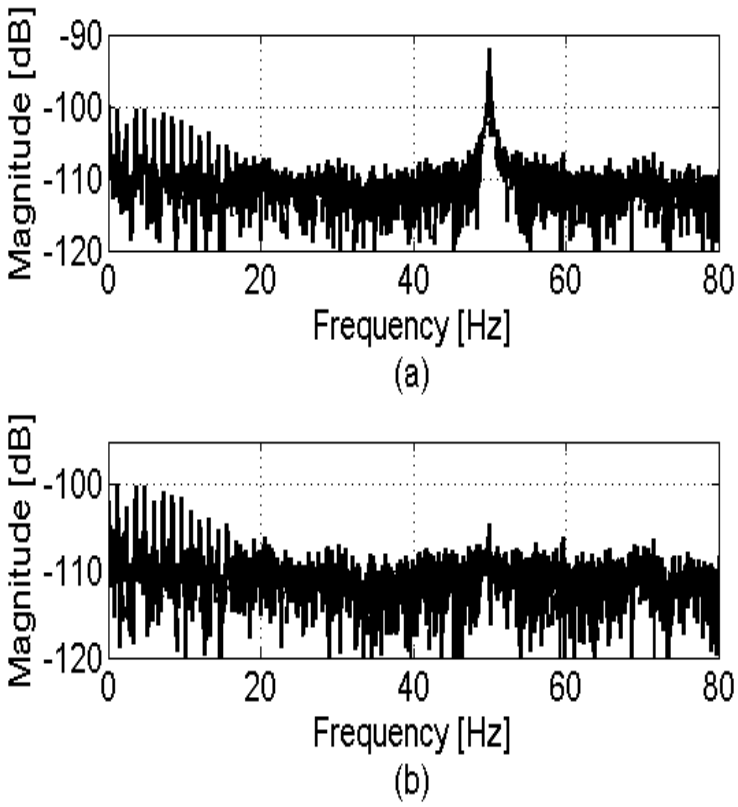

Fig.6.17: Spectrum of the heart signal extracted by (a) LMS algorithm and (b) normalised LMS algorithm.

6.4.4 Signals recovered by the noise canceller based on heuristic algorithms

The performance of the heuristic algorithms were compared on the basis of minimum MSE achieved, the number of iterations and the CPU processing time for several population size. It is important to notice that all the following results were averaged over 100 measurements.

Fig.6.18 (a and b) show the minimum MSE achieved by PSO algorithm and GA algorithm, respectively, versus the population size. Both the algorithms achieved better results (lower MSE) as the population size increases. Especially PSO algorithm shows a linear dependence between the population size and the minimum MSE, while the minimum MSE achieved by GA algorithm starts to decrease slower after a population size of 30. Moreover, it obvious from Fig.6.18 (a and b) that the minimum MSE attained by the PSO algorithm is generally lower than that achieved by the GA algorithm.

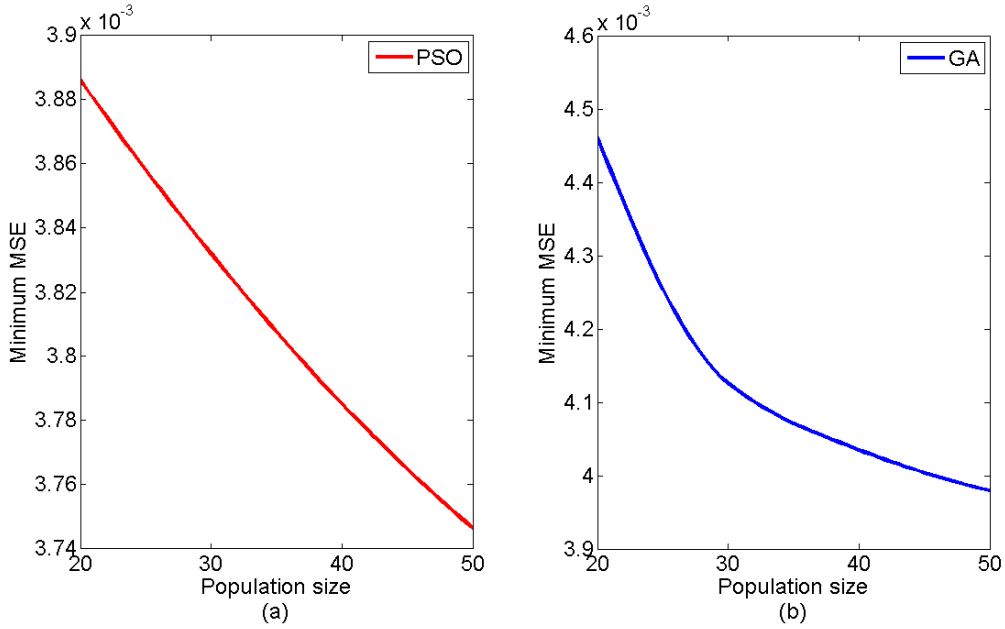

Fig.6.18: Minimum MSE versus population size for (a) PSO and (b) GA.

Since the objective of the PSO and GA algorithms is to minimize the MSE of the noise canceller, results shown in Fig.6.18 (a and b) suggests to use a high population size in order to maximize the noise suppression. However, to choose the more appropriate population size the number of iterations and the CPU processing time must be taken into account. Fig.6.19 (a and b) show the number of iterations versus the population size for the PSO algorithm and the GA algorithm, respectively. The number of iterations of the GA algorithm varies between 23.6 and 21.6 and remains constant after a population size of 40, while for the PSO algorithm the number of iterations is generally higher, between 155 and 125, and decreases with increasing population size. On the other hand, the processing time show an opposite trend respect to the number of iterations. In fact, as shown in Fig.6.20 (a and b), the processing time increases with increasing population size, particularly after a population size of 30 it grows exponentially for both algorithms. However, the GA algorithm shows a generally lower processing time (between 0.11 and 0.16 seconds) respect to the processing time of the PSO algorithm (between 0.8 and 1.4 seconds). This results in a longer convergence time of the PSO algorithm respect to the GA algorithm.

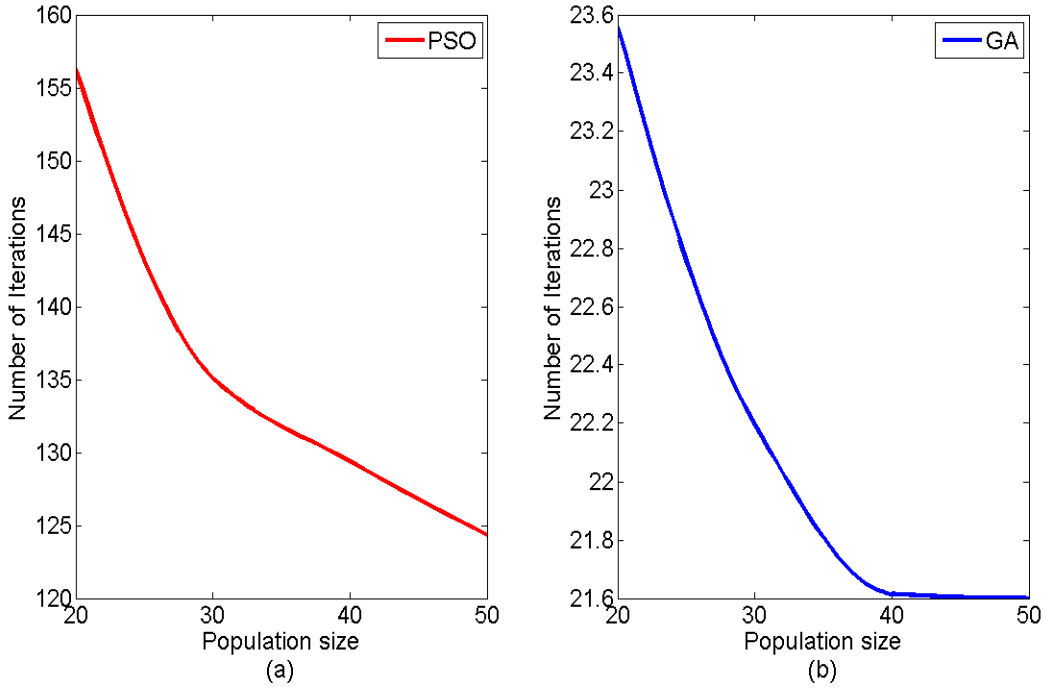

Fig.6.19: Number of iterations versus population size for (a) PSO and (b) GA.

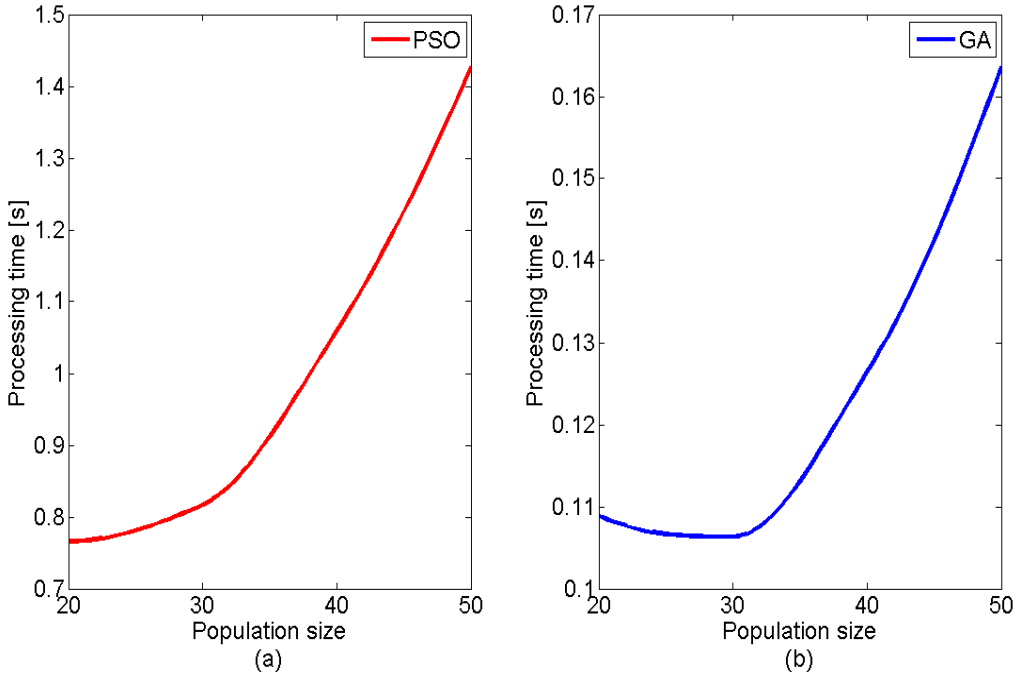

Fig.6.20: Processing time versus population size for (a) PSO and (b) GA.

In order to maintain the processing time of both heuristic algorithms low and hence guarantee a fast convergence, the population size was set to 30 for the recovering of the weak magnetic heart signal from the magnetically noisy signals measured by the optical magnetometers, shown in Fig.6.15 (c and e).

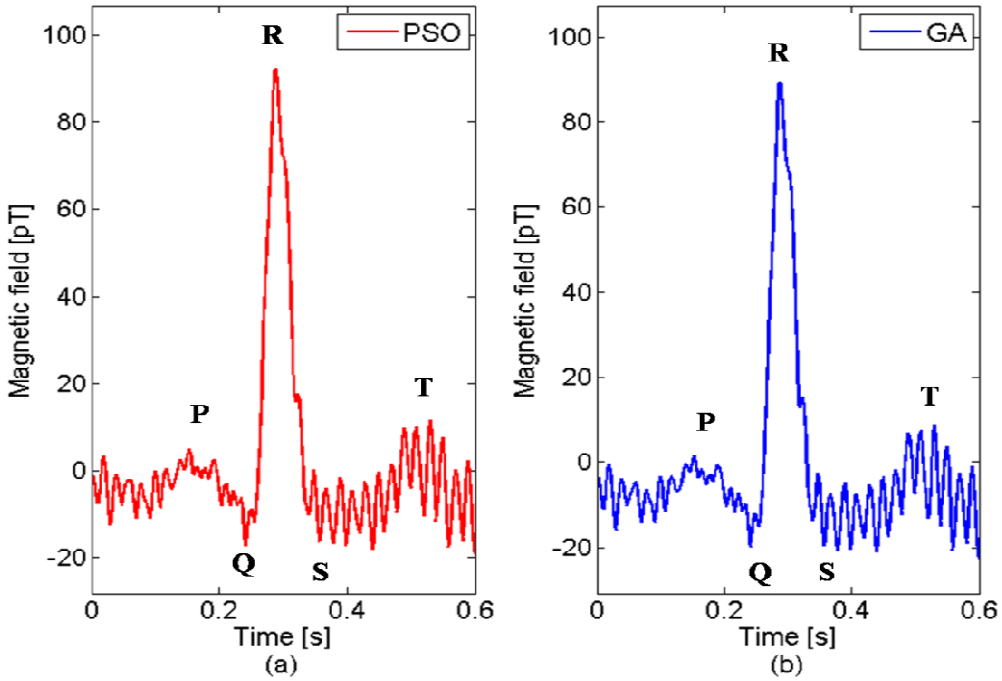

Fig.6.21: Heart signal recovered by (a) PSO and (b) GA algorithms from the noisy signals measured by the optical magnetometer. The detected P wave, QRS complex and T wave are highlighted. The population size is 30.

Fig.6.21 (a and b) show the heart signal recovered by the PSO algorithm and the GA algorithm, respectively. Both algorithms detected the P wave and the QRS complex clearly, while the T wave resulted noisier. Comparing these signals with the heart signals recovered by LMS and nLMS algorithms, shown in Fig.6.16 (a and b), respectively, it is noticed that the QRX complex and the P wave are more clearly defined in the signals recovered by the heuristic algorithms. However, the nLMS algorithm outperforms the heuristic algorithms in suppressing the noise interference at 50Hz. In fact both the PSO algorithm and the GA algorithm maintained a strong component at 50Hz, as shown in Fig.6.22 (a and b),

respectively. On the other hand, the normalised LMS algorithm was capable of completely remove the 50Hz component, as shown in Fig.6.17 (b).

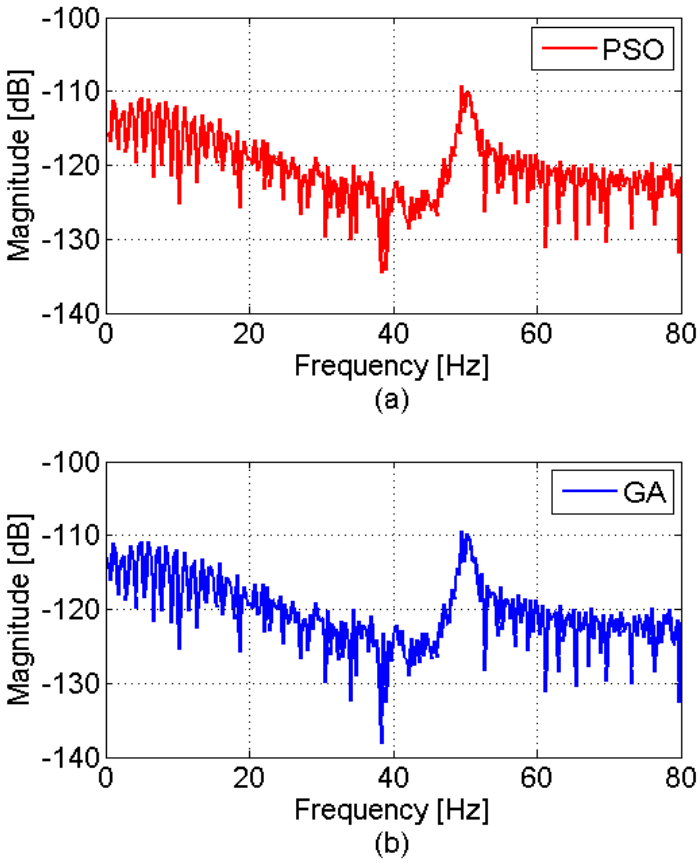

Fig.6.22: Spectrum of the heart signal recovered by (a) PSO and (b) GA algorithms from the noisy signals measured by the optical magnetometer. The component at 50Hz is not completely removed. The population size is 30.

6.5 Results discussion

The first simulation was used to investigate and compare the capability of the LMS algorithm, the normalised LMS algorithm and the GA algorithm to improve the signal-to-noise ratio (SNR), cancelling the 60Hz interference and detecting peaks for different initial SNR. Simulation results have shown that for low SNR values, the GA technique outperforms the other techniques in noise cancellation; however, its convergence time was longer.

This conclusion was validated by the second simulation that used simulated heart signals and a measured magnetic noise to compare the performances of both LMS and GA algorithms in terms of SNR improvement and heart peaks reconstruction. Simulation results have shown that the GA algorithm attains better SNR improvement than the LMS algorithm. A measured heart signal has been recovered by the GA algorithm with a SNR improvement of 37.4dB and the QRS complex and T wave have successfully been detected. The LMS algorithm has also recovered the input signal, however, with a lower SNR improvement of 33dB and noisy QRS complex and T wave.

Since the simulation results have demonstrated that techniques based on optimal search have the potential for noise cancellation in applications where the signal to noise ratio is much lower than unity, the use of PSO and GA algorithms have been investigated for adaptive noise suppression and the recovering of heart signals in a magnetically-unshielded environment. Simulated heart signals and measured magnetic noise have therefore been used to compare the performances of both PSO and GA algorithms in terms of SNR improvement and CPU utilization time. Simulation results have shown that for high iteration numbers the PSO algorithm attains better SNR improvement; however it requires higher CPU utilization time to find an optimum solution than the GA algorithm. For a population size of 30 individuals and a number of iterations equals to 100, a measured heart signal has successfully been recovered by the PSO algorithm with an SNR improvement of 38.4dB and all P, QRS, and T features have successfully been detected. The GA algorithm has also recovered the input signal, however, with a lower SNR improvement of 36.3dB, undetectable P wave, and noisy QRS complex and T wave.

The simulation results have also been validated by experimental results. The Mx-configuration-based optically-pumped quantum magnetometer employing two sensing cells has been used in a magnetically-unshielded environment to capture the two signals to be fed as inputs of the adaptive noise canceller. The LMS, normalised LMS, GA and PSO algorithms have been investigated for suppressing the power line generated 50Hz interference and recovering of heart signals. As predicted by the simulations, the PSO and GA algorithms have clearly detected

the P wave, QRS complex, and T wave, while the heart signal recovered by the LMS based algorithms presented nosier features. However, the normalised LMS algorithm has outperformed the other algorithms in the cancellation of 50Hz noise component. Moreover, the heuristic algorithms have been compared with each other in terms of MSE minimization capability, number of iterations and processing time yielding the same results of simulations. Experimental results have shown that the PSO algorithm outperforms the GA algorithm in MSE minimization but has a longer convergence time and requires a higher number of iterations.

The adaptive noise cancellation system employing different optimization algorithms has been capable of recovery the heart signal and the cardiac features from the original noisy signal, hence enhancing the magnetometer's sensitivity, which reaches $10pT/Hz^{1/2}$.

6.6 Summary

In this chapter, the techniques of adaptive noise canceller based on the Least-Mean Squares, normalised Least-Mean Squares, Genetic Algorithm and Particle Swarm Optimization, described in Chapter 4, have been experimentally investigated to demonstrate their applicability to magnetocardiography in a magnetically-unshielded environment. The algorithms have been firstly tested over simulated signals, then experimentally validated with signals measured using an array of optical magnetometer elements that were optimized in Chapter 5. Substantial agreement between simulation and experimental result has been observed. The results shown in this chapter are useful for signal processing in magnetocardiographic system operating in a magnetically-unshielded environment.

Chapter 7

Conclusion and future work

In this chapter, we conclude the work which has been undertaken in this project. We also discuss some possible applications and future research directions involving the measurements of a very weak magnetic field in an electromagnetically noisy environment.

7.1 Conclusion

This thesis has presented a theoretical and experimental investigation of a magnetocardiographic system employing an array of optically-pumped quantum magnetometers and an adaptive noise cancellation system capable of recovering a weak magnetic heart signal from a much higher electromagnetic environmental noise. A comprehensive literature review has been conducted providing an overview of the existing techniques for heart signal monitoring followed by an introduction outlining the fundamentals and the diverse operational modes of optical magnetometers and highlighting their advantages and disadvantages. In addition, electromagnetic environmental noise problems have been discussed through an overview of noise suppression techniques, which are currently used in unshielded magnetocardiography. Chapter 3 and 4, respectively, have provided a detailed description of the working principle of the developed optical magnetometer and the adaptive noise canceller based on Least-Mean Squares algorithms as well as heuristic techniques. In Chapter 5, all the components of the developed optically-pumped quantum magnetometer have been described in detail. In particular, the dependence of the sensitivity and the frequency bandwidth of the instrument on the laser light power and vapour cell temperature has been theoretically discussed (in Chapter 3) and experimentally demonstrated (in Chapter 5). The resulting optimized magnetometer has been used in an array configuration in order to measure noise corrupted heart magnetic signals and the environmental magnetic noise. These signals have been used to compare the performances of adaptive noise canceller employing technique based on the Least-Mean Squares, normalised Least-Mean Squares, Genetic Algorithms and Particle Swarm Optimization, in terms of SNR improvement, 60Hz interference suppression and heart peak reconstruction. Simulation and experimental results have been presented, showing the capability of the developed magnetocardiographic system, which combines optical magnetometry and adaptive noise cancellation, to recover very weak magnetic heart signals from a much stronger electromagnetic noise in a magnetically-unshielded environment.

The following objectives have been reached during this project:

- Design and development of a high-sensitivity optically-pumped quantum magnetometer;
- Magnetometer's sensitivity and frequency bandwidth characterization and optimization;
- Development of a two dimensional array of characterized magnetometer for adaptive noise cancellation applications;
- Experimental demonstration of a weak magnetic field, differentiated from a much higher noise by means of adaptive noise cancellation based on Least Mean Squares (LMS) algorithm and normalised LMS algorithm.
- Experimental demonstration of the capability of the adaptive noise canceller based on heuristic techniques, namely, Genetic Algorithms (GA) and Particle Swarm Optimization (PSO), of suppressing the noise in case of a very low initial Signal-to-Noise Ratio.
- Experimental demonstration of the proof of concept of the magnetocardiographic system based on optical magnetometry and employing adaptive noise cancellation of recovering a weak magnetic heart signal, with clear identification of typical heart features, from a much stronger environmental electromagnetic noise, into a magnetically-unshielded environment.

7.2 Future work

In future, further research investigations are needed for the design and development of advanced unshielded optical magnetometry systems that can find application in magnetocardiography. The principal significance of the developed optical magnetometer employing the noise cancellation system is its experimentally-demonstrated ability of measuring very weak magnetic signals in an unshielded environment, where the electromagnetic noise is much stronger than the signal. By reducing the dimensions of the magnetometers and developing faster adaptive noise cancellation systems, portable magnetocardiography system

can be developed. Moreover, by adding more sensors and averaging the measured signals the performance of the system can be improved significantly.

It is worthwhile investigating the applicability of optically-pumped quantum magnetometers based on the use of an array configuration and an adaptive noise cancellation system in foetal magnetocardiography; magnetoencephalography and magnetorelaxometry, as described below.

7.2.1 Foetal magnetocardiography

The developed optical cardiomagnetometer employing adaptive noise cancellation can be easily applied to foetal magnetocardiography. The foetal magnetocardiography is a non-invasive and completely harmless diagnostic tool that aims to evaluate the electrical activity of the foetal heart by measuring the magnetic field over the abdomen of a pregnant woman. Since the amniotic fluid that surrounds the foetus has high impedance, only a few part of electric current generated from heart cells reaches the surface of the maternal abdomen, a loss of information affects the foetal ECG data. Moreover, after the 28^{th} week of gestation the foetus is completely surrounded by vernix caseosa that has high impedance and so creates an insulation effect against electric currents that, therefore, cannot reach the surface of the abdomen [121]. At the same time, all these currents also give rise to a really weak magnetic field, which can be measured by high sensitivity magnetometers.

7.2.2 Magnetoencephalography

Magnetoencephalography (MEG) aims to monitoring the human brain activity by measuring the magnetic field generated by the electrical currents associated with natural brain activity. Fig.7.1 shows the origins of the brain magnetic signals.

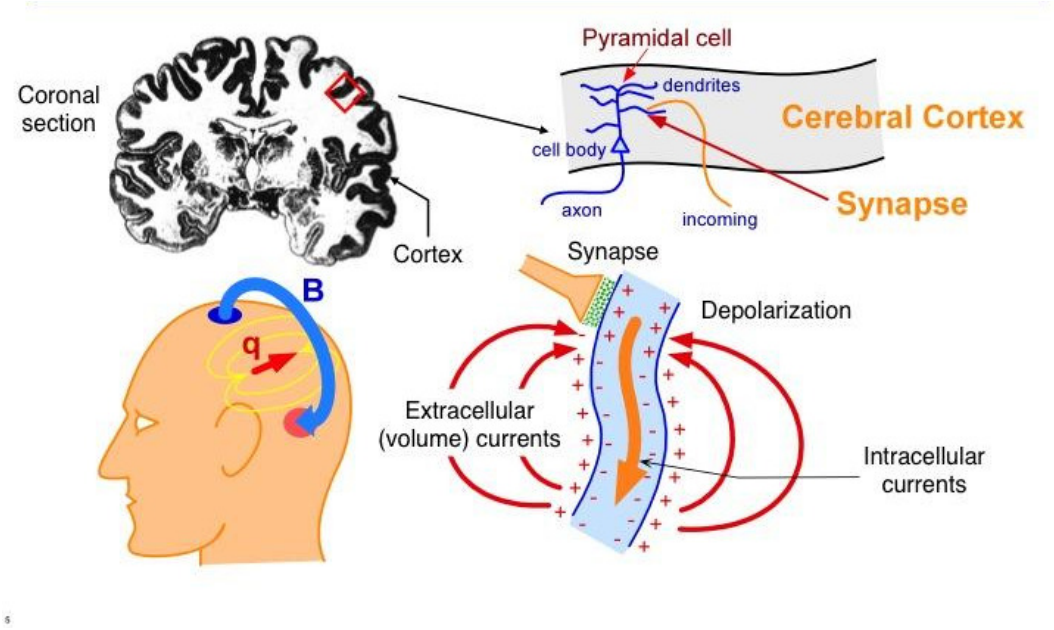

Fig.7.1: The principle of Magnetoencephalography and illustration of the origins of the brain magnetic signals (from [122]).

The magnetic field produced by the brain activity is much weaker than the heart generated magnetic field, of order of fT. For this reason, at present only SQUID based magnetometers are used for Magnetoencephalography [123-125]. By further increasing the sensitivity of optical magnetometers, they can substitute SQUID-based magnetometers, bringing all the advantages that were discussed in Chapter 1, especially, the absence of a cumbersome and expensive cooling system.

7.2.3 Magnetorelaxometry

The principle of Magnetorelaxometry, as illustrated in Fig.7.2, is based on the fact that a magnetic nanoparticle (MNP) relaxes after being aligned by a magnetic field, generating a magnetic field with characteristic parameters, such as relaxation amplitude and relaxation time.

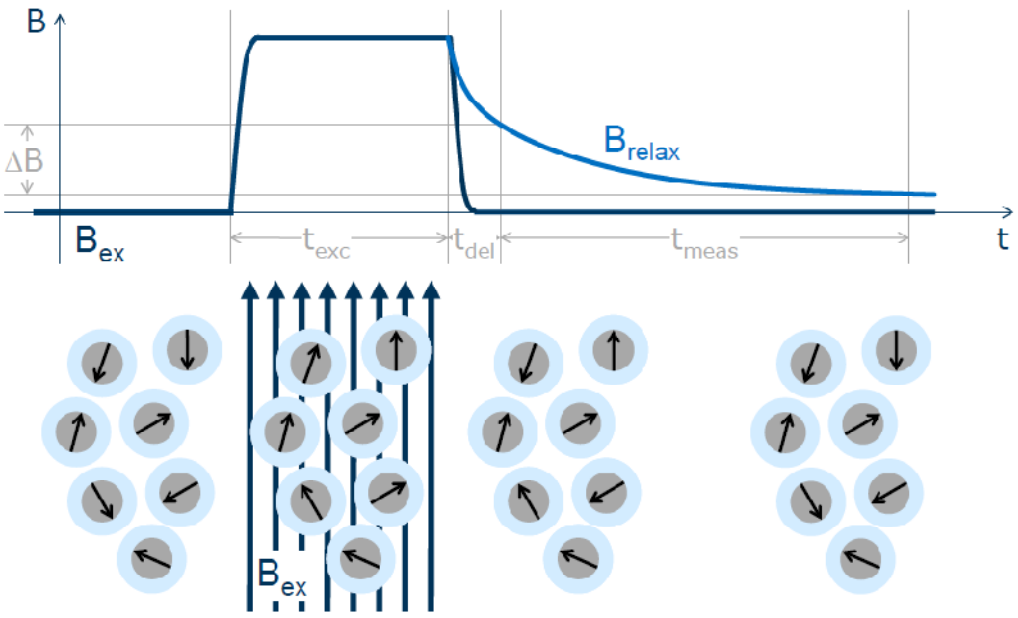

Fig.7.2: Illustration of the principle of Magnetorelaxometry (from http://gast.tu-ilmenau.de/wpcontent/uploads/Daniel_Baumgarten__Magnetic_nanoparticle_imaging.pdf)

Magnetorelaxometry applications include (i) localization and quantification of magnetic nanoparticles for control of heat generation in the treatment of cancer cells [126]; (ii) detection and quantification of specific biological targets [127, 128]; (iii) determination of the binding of antibodies to their antigens [129]; and (iv) contrast enhancement in magnetic resonance imaging of biological tissue [130].

To date, experiments on magnetorelaxometry were performed using SQUID-based magnetometers or fluxgate magnetometers. The use of optical magnetometers in magnetorelaxometry leads to advantages in comparison with SQUID and fluxgate sensors, because optical magnetometers do not require cooling and are more sensitive than fluxgate magnetometers.

Publications

Peer-Reviewed Journals

- V. Tiporlini and K. Alameh, "Optical Magnetometer Employing Adaptive Noise Cancellation for Unshielded Magnetocardiography," Universal Journal of Biomedical Engineering, vol. 1, p. 5, 2013.
- V. Tiporlini and K. Alameh, "High Sensitivity Optically Pumped Quantum Magnetometer," The Scientific World Journal, vol. 2013, p. 8, 2013.
- V. Tiporlini, H. N. Nguyen, and K. Alameh, "Noise Cancellation in Unshielded Magnetocardiography based on Least Mean Squared Algorithms and Genetic Algorithms," Nano Systems: Physics, Chemistry and Mathematics, vol. 4, p. 7, 2013.

International Conferences Proceedings

- V. Tiporlini, H. N. Nguyen, and K. Alameh, "Noise Suppression in Unshielded Magnetocardiography: Least-Mean Squared Algorithm versus Genetic Algorithm," in International Symposium on Macro and Supramolecular Architectures and Materials, MAM-12, Coimbatore, India, 2012.
- V. Tiporlini, H. N. Nguyen, and K. Alameh, "Adaptive noise canceller for magnetocardiography," in High Capacity Optical Networks and Enabling Technologies (HONET), 2011, pp. 359-363.
- S. Silva, H. N. Nguyen, V. Tiporlini, and K. Alameh, "Web based water quality monitoring with sensor network: Employing ZigBee and WiMax technologies," in High Capacity Optical Networks and Enabling Technologies (HONET), 2011, pp. 138-142.

References

[1] I. R. Hanna and M. E. Silverman, "A history of cardiac auscultation and some of its contributors," *The American Journal of Cardiology,* vol. 90, pp. 259-267, 2002.

[2] A. Roguin, *Rene Theophile Hyacinthe Laënnec (1781-1826): the man behind the stethoscope* vol. 4, 2006.

[3] J. Hope, *A treatise on the diseases of the heart and great vessels*, 1832.

[4] M. E. Silverman, "Charles J. B. Williams: English Pioneer in Auscultation," *Clinical Cardiology,* vol. 30, pp. 532-534, 2007.

[5] I. Edler and C. H. Hertz, "The Use of Ultrasonic Reflectoscope for the Continuous Recording of the Movements of Heart Walls," *Clinical Physiology and Functional Imaging,* vol. 24, pp. 118-136, 2004.

[6] A. D. Waller, "A Demonstration of Man of Electromotive Changes Accompanying the Heart's Beat," *Annals of Noninvasive Electrocardiology,* vol. 9, pp. 189-191, 2004.

[7] M. Rivera-Ruiz, C. Cajavilca, and J. Varon, "Einthoven's string galvanometer - The first electrocardiograph," *Texas Heart Institute Journal,* vol. 35, pp. 174-178, 2008.

[8] J. W. Hurst, *Naming of the Waves in the ECG, With a Brief Account of Their Genesis*.

[9] W. B. Fye, "A History of the origin, evolution, and impact of electrocardiography," *The American Journal of Cardiology,* vol. 73, pp. 937-949, 1994.

[10] R. Oweis and L. Hijazi, "A computer-aided ECG diagnostic tool," *Comput Methods Programs Biomed,* vol. 81, pp. 279-84, 2006.

[11] M. Sandstrom*, et al.*, "Holter ECG monitoring in patients with perceived electrical hypersensitivity," *Int J Psychophysiol,* vol. 49, pp. 227-35, 2003.

[12] G. Baule and R. McFee, "DETECTION OF THE MAGNETIC FIELD OF THE HEART," *American heart journal,* vol. 66, pp. 95-96, 1963.

[13] G. Baule and R. McFee, "Theory of Magnetic Detection of the Heart's Electrical Activity," *Journal of Applied Physics,* vol. 36, pp. 2066-2073, 1965.

[14] Y. D. Safonov, V. M. Provotorov, V. M. Lubé, and L. I. Yakimenkov, "Method of recording the magnetic field of the heart (magnetocardiography)," *Bulletin of Experimental Biology and Medicine,* vol. 64, pp. 1022-1024, 1967/09/01 1967.

[15] D. Cohen, E. A. Edelsack, and J. E. Zimmerman, "MAGNETOCARDIOGRAMS TAKEN INSIDE A SHIELDED ROOM WITH A SUPERCONDUCTING POINT‐CONTACT MAGNETOMETER," *Applied Physics Letters,* vol. 16, pp. 278-280, 1970.

[16] R. Fagaly, "Superconducting quantum interference device instruments and applications," *Review of Scientific Instruments,* vol. 77, p. 101101, 2006.

[17] Y. Hong-Chang*, et al.*, "High-<equation>T_c</equation> superconducting quantum interference devices: Status and perspectives," *Journal of Applied Physics,* vol. 104, pp. 011101-011101-12, 2008.

[18] H. Koch, "SQUID magnetocardiography: status and perspectives," *Applied Superconductivity, IEEE Transactions on,* vol. 11, pp. 49-59, 2001.

[19] A. Tsukamoto*, et al.*, "Development of high-temperature superconducting SQUID system for magnetocardiography," *Electronics and Communications in Japan (Part II: Electronics),* vol. 90, pp. 46-55, 2007.

[20] C. Parasakthi*, et al.*, "Establishment of 37 channel SQUID system for magnetocardiography," *AIP Conference Proceedings,* vol. 1447, pp. 871-872, 2012.

[21] Y. Hong-Chang*, et al.*, "Scanning high- T c SQUID imaging system for magnetocardiography," *Superconductor Science and Technology,* vol. 19, p. S297, 2006.

[22] Y. V. Maslennikov*, et al.*, "The DC-SQUID-based Magnetocardiographic Systems for Clinical Use," *Physics Procedia,* vol. 36, pp. 88-93, 2012.

[23] Y. H. Lee, *et al.*, "64-Channel Second-Order Planar Gradiometer System for Magnetocardiograms," *Applied Superconductivity, IEEE Transactions on,* vol. 17, pp. 831-834, 2007.

[24] Y. Zhang, *et al.*, "Foetal magnetocardiography with a multi-channel HTS rf SQUID gradiometer," *Superconductor Science and Technology,* vol. 19, p. S266, 2006.

[25] J. F. Strasburger, B. Cheulkar, and R. T. Wakai, "Magnetocardiography for fetal arrhythmias," *Heart rhythm : the official journal of the Heart Rhythm Society,* vol. 5, pp. 1073-6, Jul 2008.

[26] D. Brisinda, *et al.*, "Multichannel mapping of fetal magnetocardiogram in an unshielded hospital setting," *Prenatal Diagnosis,* vol. 25, pp. 376-382, 2005.

[27] M. N. Livanov, *et al.*, "Record of the human magnetocardiogram by the quantum gradiometer with optical pumping," *Advances in cardiology,* vol. 28, pp. 78-80, 1981.

[28] G. Bison, R. Wynands, and A. Weis, "Optimization and performance of an optical cardiomagnetometer," *J. Opt. Soc. Am. B,* vol. 22, pp. 77-87, 2005.

[29] K. Kamada, Y. Ito, and T. Kobayashi, "Human MCG measurements with a high-sensitivity potassium atomic magnetometer," *Physiological Measurement,* vol. 33, p. 1063, 2012.

[30] G. Bison, *et al.*, "A room temperature 19-channel magnetic field mapping device for cardiac signals," *Applied Physics Letters,* vol. 95, pp. 173701-3, 2009.

[31] V. Shah, S. Knappe, P. D. D. Schwindt, and J. Kitching, "Subpicotesla atomic magnetometry with a microfabricated vapour cell," *Nat Photon,* vol. 1, pp. 649-652, 2007.

[32] L.-A. Liew, *et al.*, "Microfabricated alkali atom vapor cells," *Applied Physics Letters,* vol. 84, pp. 2694-2696, 2004.

[33] M. Reta-Hernández and G. G. Karady, "Attenuation of low frequency magnetic fields using active shielding," *Electric Power Systems Research,* vol. 45, pp. 57-63, 1998.

[34] R. Plonsey, "Capability and Limitations of Electrocardiography and Magnetocardiography," *Biomedical Engineering, IEEE Transactions on,* vol. BME-19, pp. 239-244, 1972.

[35] T. Oostendorp, J. Nenonen, and G. Huiskamp, "Comparison of inverse solutions obtained from ECG and MCG data," in *Engineering in Medicine and Biology Society, 1996. Bridging Disciplines for Biomedicine. Proceedings of the 18th Annual International Conference of the IEEE*, 1996, pp. 1427-1428 vol.4.

[36] H. Kwon*, et al.*, "Non-invasive magnetocardiography for the early diagnosis of coronary artery disease in patients presenting with acute chest pain," *Circulation journal : official journal of the Japanese Circulation Society,* vol. 74, pp. 1424-30, Jul 2010.

[37] F. E. Smith*, et al.*, "Comparison of magnetocardiography and electrocardiography: a study of automatic measurement of dispersion of ventricular repolarization," *Europace,* vol. 8, pp. 887-893, Oct 2006.

[38] J. Wikswo, "Biomagnetic Sources and Their Models," in *Advances in Biomagnetism*, S. Williamson*, et al.*, Eds., ed: Springer US, 1990, pp. 1-18.

[39] D. P. Zipes and J. Jalife, *Cardiac electrophysiology : from cell to bedside*. Philadelphia: Saunders.

[40] H. J. Wellens, "Cardiac Electrophysiology: From Cell to Bedside, Fourth Edition," *Circulation,* vol. 110, p. e453, October 26, 2004 2004.

[41] D. Budker and M. Romalis, "Optical magnetometry," *Nat Phys,* vol. 3, pp. 227-234, 2007.

[42] H. G. Dehmelt, "Slow Spin Relaxation of Optically Polarized Sodium Atoms," *Physical Review,* vol. 105, pp. 1487-1489, 1957.

[43] H. G. Dehmelt, "Modulation of a Light Beam by Precessing Absorbing Atoms," *Physical Review,* vol. 105, pp. 1924-1925, 1957.

[44] F. Bloch, W. W. Hansen, and M. Packard, "The Nuclear Induction Experiment," *Physical Review,* vol. 70, pp. 474-485, 1946.

[45] F. Bloch, "Nuclear Induction," *Physical Review,* vol. 70, pp. 460-474, 1946.

[46] W. E. Bell and A. L. Bloom, "Optically Driven Spin Precession," *Physical Review Letters,* vol. 6, pp. 280-281, 1961.

[47] A. L. Bloom, "Principles of Operation of the Rubidium Vapor Magnetometer," *Applied Optics,* vol. 1, pp. 61-68, 1962/01/01 1962.

[48] W. E. Bell and A. L. Bloom, "Optical Detection of Magnetic Resonance in Alkali Metal Vapor," *Physical Review,* vol. 107, pp. 1559-1565, 1957.

[49] E. B. Alexandrov, M. V. Balabas, A. K. Vershovski, and A. S. Pazgalev, "Experimental demonstration of the sensitivity of an optically pumped quantum magnetometer," *Technical Physics,* vol. 49, pp. 779-783, 2004/06/01 2004.

[50] S. Groeger, G. Bison, J. L. Schenker, R. Wynands, and A. Weis, "A high-sensitivity laser-pumped Mx magnetometer," *The European Physical Journal D - Atomic, Molecular, Optical and Plasma Physics,* vol. 38, pp. 239-247, 2006/05/01 2006.

[51] I. K. Kominis, T. W. Kornack, J. C. Allred, and M. V. Romalis, "A subfemtotesla multichannel atomic magnetometer," *Nature,* vol. 422, pp. 596-599, 2003.

[52] M. Rosenbluh, V. Shah, S. Knappe, and J. Kitching, "Differentially detected coherent population trapping resonances excited by orthogonally polarized laser fields," *Optics Express,* vol. 14, pp. 6588-6594, 2006/07/24 2006.

[53] J. Kitching*, et al.*, "Microwave frequency reference based on VCSEL-driven dark-line resonances in Cs vapor," in *Frequency Control Symposium and Exhibition, 2000. Proceedings of the 2000 IEEE/EIA International*, 2000, pp. 687-693.

[54] F. X. Esnault*, et al.*, "Cold-atom double-Λ coherent population trapping clock," *Physical Review A,* vol. 88, p. 042120, 2013.

[55] A. Nagel*, et al.*, "Experimental realization of coherent dark-state magnetometers," *EPL (Europhysics Letters),* vol. 44, p. 31, 1998.

[56] C. Andreeva*, et al.*, "Two-color coherent population trapping in a single Cs hyperfine transition, with application in magnetometry," *Applied Physics B,* vol. 76, pp. 667-675, 2003/06/01 2003.

[57] J. Belfi, G. Bevilacqua, V. Biancalana, Y. Dancheva, and L. Moi, "All optical sensor for automated magnetometry based on coherent population trapping," *Journal of the Optical Society of America B,* vol. 24, pp. 1482-1489, 2007/07/01 2007.

[58] J. Belfi*, et al.*, "Cesium coherent population trapping magnetometer for cardiosignal detection in an unshielded environment," *Journal of the Optical Society of America B,* vol. 24, pp. 2357-2362, 2007/09/01 2007.

[59] D. Budker, D. F. Kimball, S. M. Rochester, V. V. Yashchuk, and M. Zolotorev, "Sensitive magnetometry based on nonlinear magneto-optical rotation," *Physical Review A,* vol. 62, p. 043403, 2000.

[60] P. D. D. Schwindt, L. Hollberg, and J. Kitching, "Self-oscillating rubidium magnetometer using nonlinear magneto-optical rotation," *Review of Scientific Instruments,* vol. 76, pp. -, 2005.

[61] J. C. Allred, R. N. Lyman, T. W. Kornack, and M. V. Romalis, "High-Sensitivity Atomic Magnetometer Unaffected by Spin-Exchange Relaxation," *Physical Review Letters,* vol. 89, p. 130801, 2002.

[62] R. Wyllie, M. Kauer, G. S. Smetana, R. T. Wakai, and T. G. Walker, "Magnetocardiography with a modular spin-exchange relaxation-free atomic magnetometer array," *Physics in Medicine and Biology,* vol. 57, May 2012.

[63] S. Groeger, A. S. Pazgalev, and A. Weis, "Comparison of discharge lamp and laser pumped cesium magnetometers," *Applied Physics B,* vol. 80, pp. 645-654, 2005/05/01 2005.

[64] S. Odawara*, et al.*, "Conditions of Exciting Coils Used in Evaluation of Shielding Factor of Magnetically Shielded Rooms for Uniform Magnetic Field," *Ieee Transactions on Magnetics,* vol. 47, pp. 4274-4277, Oct 2011.

[65] H. Nakane, H. Maruyama, S. Omori, and I. Yokoshima, "EFFECT OF SHIELDED ROOM ON STANDARD MAGNETIC-FIELD," *IEEE Transactions on Instrumentation and Measurement,* vol. 31, pp. 269-273, 1982.

[66] K. Hirao, K. Tsuruda, I. Aoyama, and T. Saito, "LARGE SPHERICAL MAGNETIC-SHIELD ROOM," *Journal of Geomagnetism and Geoelectricity,* vol. 37, pp. 581-588, 1985.

[67] K. Kobayashi, A. Kon, M. Yoshizawa, and Y. Uchikawa, "Active Magnetic Shielding Using Symmetric Magnetic Field Sensor Method," *Ieee Transactions on Magnetics,* vol. 48, pp. 4554-4557, Nov 2012.

[68] I. M. V. Caminiti, A. Formisano, M. C. Lupoli, and R. Martone, "A New Approach to Design Flexible Magnetic Active Shielding," *Ieee Transactions on Magnetics,* vol. 49, pp. 791-794, Feb 2013.

[69] K. Gireesan*, et al.*, "Magnetocardiography Study of Cardiac Anomalies," in *17th International Conference on Biomagnetism Advances in Biomagnetism - Biomag2010*. vol. 28, S. Supek and A. Susac, Eds., ed, 2010, pp. 431-435.

[70] Y. Nakaya and H. Mori, "MAGNETOCARDIOGRAPHY," *Clinical Physics and Physiological Measurement,* vol. 13, pp. 191-229, Aug 1992.

[71] "A room temperature 19-channel magnetic field mapping device for cardiac signals," *Applied Physics Letter,* vol. 95, pp. 1-3, 2009.

[72] W. A. M. Aarnink*, et al.*, "Active noise compensation for multichannel magnetocardiography in an unshielded environment," *Applied Superconductivity, IEEE Transactions on,* vol. 5, pp. 2470-2473, 1995.

[73] F. Resmer, H. Nowak, F. Gießler, and J. Haueisen, "Development of an active magnetic screen to allow a biomagnetometer to be used in an unshielded environment," *Superconductor Science and Technology,* vol. 17, p. 1365, 2004.

[74] B. Hilgenfeld, E. Strähmel, H. Nowak, and J. Haueisen, "Active magnetic shielding for biomagnetic measurement using spatial gradient fields," *Physiological Measurement,* vol. 24, p. 661, 2003.

[75] K. Yamazaki*, et al.*, "MCG measurement in the environment of active magnetic shield," *Neurology & clinical neurophysiology : NCN,* vol. 2004, p. 40, 2004.

[76] D. Brisinda, A. M. Meloni, and R. Fenici, "First 36-channel magnetocardiographic study of CAD patients in an unshielded laboratory

for interventional and intensive cardiac care," presented at the Proceedings of the 2nd international conference on Functional imaging and modeling of the heart, Lyon, France, 2003.

[77] R. Fenici, D. Brisinda, J. Nenonen, and P. Fenici, "Phantom validation of multichannel magnetocardiography source localization," *Pace-Pacing and Clinical Electrophysiology,* vol. 26, pp. 426-430, Jan 2003.

[78] D. Brisinda and R. Fenici, "Noninvasive classification of ventricular preexcitation with unshielded magnetocardiography and transesophageal atrial pacing and follow-up (vol 30, pg S151, 2007)," *Pace-Pacing and Clinical Electrophysiology,* vol. 30, pp. 1427-1427, Nov 2007.

[79] D. Brisinda, R. Fenici, A. M. Meloni, and P. Fenici, "Multichannel magnetocardiographic mapping of small animals in an unshielded laboratory," *European Heart Journal,* vol. 24, pp. 306-306, Aug-Sep 2003.

[80] R. Fenici, D. Brisinda, A. R. Sorbo, and A. Venuti, "UNSHIELDED MAGNETIC SOURCE IMAGING OF FETAL CARDIAC ACTIVITY FOR ELECTROPHYSIOLOGIC FOLLOW-UP DURING PREGNANCY," *Journal of Cardiovascular Electrophysiology,* vol. 22, pp. S115-S115, Oct 2011.

[81] M. Bick*, et al.*, "SQUID gradiometry for magnetocardiography using different noise cancellation techniques," *Applied Superconductivity, IEEE Transactions on,* vol. 11, pp. 673-676, 2001.

[82] U. Schneider, J. Haueisen, M. Loeff, N. Bondarenko, and E. Schleussner, "Prenatal diagnosis of a long QT syndrome by fetal magnetocardiography in an unshielded bedside environment," *Prenatal Diagnosis,* vol. 25, pp. 704-708, Aug 2005.

[83] Y. Seki*, et al.*, "Unshielded fetal magnetocardiography system using two-dimensional gradiometers," *Review of Scientific Instruments,* vol. 79, pp. -, 2008.

[84] S. Comani, D. Mantini, G. Alleva, S. Di Luzio, and G. L. Romani, "Optimal filter design for shielded and unshielded ambient noise reduction in fetal magnetocardiography," *Physics in Medicine and Biology,* vol. 50, pp. 5509-5521, Dec 2005.

[85] S. J. Seltzer and M. V. Romalis, "Unshielded three-axis vector operation of a spin-exchange-relaxation-free atomic magnetometer," *Applied Physics Letters,* vol. 85, pp. 4804-4806, Nov 2004.

[86] D. A. Steck, "Title," unpublished.

[87] D. D. D. P. K. D. F. Budker, *Atomic physics : an exploration through problems and solutions*. Oxford: Oxford Univ. Press, 2008.

[88] D. Rife and R. R. Boorstyn, "Single tone parameter estimation from discrete-time observations," *Information Theory, IEEE Transactions on,* vol. 20, pp. 591-598, 1974.

[89] G. Bison, R. Wynands, and A. Weis, "Optimization and performance of an optical cardiomagnetometer," *Journal of the Optical Society of America B-Optical Physics,* vol. 22, pp. 77-87, Jan 2005.

[90] U. Mahbub, S. A. Fattah, and Ieee, *Gradient Based Adaptive Filter Algorithm for Single Channel Acoustic Echo Cancellation in Noise*, 2012.

[91] X. Y. Zhao, H. Y. Wang, D. Y. Fu, and H. S. Zhou, "The Adaptive Filtering Algorithms for Engine's Noise Cancellation in Speech Signals," in *Mechanical and Electronics Engineering Iii, Pts 1-5*. vol. 130-134, H. Zhao, Ed., ed, 2012, pp. 1323-1326.

[92] O. Sharifi-Tehrani and E. Ghafarioun, "Design and Implementation of Dual-Microphone Adaptive-Active Noise Cancellation System for De-Noising Speech Signal," *Przeglad Elektrotechniczny,* vol. 88, pp. 258-261, 2012.

[93] N. Sonbolestan, S. A. Hadei, and Ieee, *A Fast Affine Projection Algorithm Based on Matching Pursuit in Adaptive Noise Cancellation for Speech Enhancement*, 2010.

[94] V. Wu*, et al.*, "Adaptive Noise Cancellation to Suppress Electrocardiography Artifacts During Real-Time Interventional MRI," *Journal of Magnetic Resonance Imaging,* vol. 33, pp. 1184-1193, May 2011.

[95] B. F. Tian, J. Lin, Q. M. Duan, and C. D. Jiang, "Variable step adaptive noise cancellation algorithm for magnetic resonance sounding signal with

a reference coil," *Chinese Journal of Geophysics-Chinese Edition,* vol. 55, pp. 2462-2472, Jul 2012.

[96] K. B. Hu and Y. X. Liu, "Adaptive Noise Cancellation Method for Fiber Optic Gyroscope," in *2012 International Workshop on Information and Electronics Engineering*. vol. 29, H. Guo, Ed., ed, 2012, pp. 1338-1343.

[97] A. Singh and V. Lubecke, "Adaptive Noise Cancellation for Two Frequency Radar Using Frequency Doubling Passive RF Tags," *Ieee Transactions on Microwave Theory and Techniques,* vol. 61, pp. 2975-2981, Aug 2013.

[98] R. D. Yang and Y. L. Zhang, "Denoising of ECG Signal Based on Empirical Mode Decomposition and Adaptive Noise Cancellation," in *Advances in Science and Engineering, Pts 1 and 2*. vol. 40-41, Z. Zhilin and P. Wang, Eds., ed, 2011, pp. 140-145.

[99] C. H. Chang, K. M. Chang, and H. J. Ko, *Cancellation of High-Frequency Noise in ECG Signals Using Adaptive Filter without External Reference*, 2010.

[100] V. Hegde, R. Deekshit, and P. S. Satyanarayana, "Transform Domain Robust Variable Step Size Griffiths' Adaptive Algorithm for Noise Cancellation in ECG," in *2nd International Conference on Methods and Models in Science and Technology*. vol. 1414, R. B. Patel and B. P. Singh, Eds., ed, 2011.

[101] T. Washio, S. Kuriki, M. Fujita, and A. Hayashi, "Adaptive cancellation of line-frequency noise in magnetocardiogram measurements," in *Engineering in Medicine and Biology Society, 2001. Proceedings of the 23rd Annual International Conference of the IEEE*, 2001, pp. 2186-2189 vol.3.

[102] N. V. Thakor and Z. Yi-Sheng, "Applications of adaptive filtering to ECG analysis: noise cancellation and arrhythmia detection," *Biomedical Engineering, IEEE Transactions on,* vol. 38, pp. 785-794, 1991.

[103] M. Z. U. Rahman, R. A. Shaik, and R. K. Reddy, "Noise Cancellation in ECG Signals using Computationally Simplified Adaptive Filtering

Techniques: Application to Biotelemetry," *Signal Processing: An International Juornal,* vol. 3, pp. 120-131, 2009.

[104] S. Gholami-Boroujeny and M. Eshghi, "Efficient adaptive noise cancellation using genetic optimization," in *Signal Processing (ICSP), 2010 IEEE 10th International Conference on*, 2010, pp. 2596-2599.

[105] X. Liu, H. Gao, and J. Liu, "Adaptive noise canceller based on PSO algorithm," in *Automation and Logistics, 2008. ICAL 2008. IEEE International Conference on*, 2008, pp. 1759-1762.

[106] J. S. P. Syamala, R. K. Verma, P. Kumar, R. Siddavatam, and S. P. Ghrera, *An Evolutionary Approach to Image Noise Cancellation Using Adaptive Particle Swarm Optimization (APSO)*, 2010.

[107] R. K. Jatoth, S. Anoop, and C. M. Prabhu, *An Intelligent Adaptive Noise Cancellation System for the Extraction of Fetal ElectroCardioGram*, 2009.

[108] B. Widrow*, et al.*, "Adaptive Noise Cancelling: Principles and Applications," *Proceedings of the IEEE,* vol. 63, pp. 1692-1716, 1975.

[109] P. Diniz, *Adaptive Filtering: Algorithms and Practical Implementation*: Springer, 2010.

[110] D. E. Goldberg, *Genetic Algorithms in Search, Optimization, and Machine Learning*: Addison-Wesley pubblishing company, inc., 1989.

[111] A. Chipperfield, P. Fleming, H. Pohlheim, and C. Fonseca, "Genetic Algorithm Toolbox For Use with Matlab. User's Guide," version 1.2, 2005.

[112] J. Kennedy and R. C. Eberhart, *Swarm Intelligence*, 1st ed. San Diego, CA: Academic Press, 2001.

[113] A. Banks, J. Vincent, and C. Anyakoha, "A review of particle swarm optimization. Part I: background and development," *Natural Computing* vol. 6, pp. 467-484, 2007.

[114] B. Birge, "PSOt - a Particle Swarm Optimization Toolbox for use with Matlab," in *IEEE Proceedings of the Swarm Intelligence Symposium* 2003, pp. 182-186.

[115] B. Birge. *Particle Swarm Optimization Toolbox*. Available: http://www.mathworks.com/matlabcentral/fileexchange/

[116] D. W., "Doppler-free saturated absorption: Laser spectroscopy," *American Journal of Physics,* vol. 64, pp. 1432-1436, 1996.

[117] M. GB and M. RG, "The impact of the MIT-BIH Arrhythmia Database," *IEEE Engineering in Medicine and Biology,* vol. 20, pp. 45-50, 2001.

[118] *MIT-BIH Arrhythmia Database*. Available: http://physionet.org/physiobank/database/mitdb/

[119] J. Malmivuo and R. Plonsey, *Bioelectromagnetism. Principles and Applications of Bioelectric and Biomagnetic Fields*. New York Osford: Oxford University Press, 1995.

[120] "Atomic Vector Gradiometer System Using Caesium Vapour cells for magnetocardiography: Perspective on Practical Application," *IEEE Transactions on Instrumentation and Measurement,* vol. 56, pp. 458-462, 2007.

[121] P. Leeuwen, H. Bettermann, M. Schüßler, and S. Lange, "Magnetocardiography in the Determination of Fetal Heart Rate Complexity," in *Biomag 96*, C. Aine*, et al.*, Eds., ed: Springer New York, 2000, pp. 573-576.

[122] U. o. W. Institute for Learning and Brain Science. Available: http://ilabs.washington.edu/what-magnetoencephalography-meg

[123] A. N. Matlashov*, et al.*, "SQUID-based systems for co-registration of ultra-low field nuclear magnetic resonance images and magnetoencephalography," *Physica C-Superconductivity and Its Applications,* vol. 482, pp. 19-26, Nov 2012.

[124] M. I. Faley*, et al.*, "High-T-c DC SQUIDs for Magnetoencephalography," *Ieee Transactions on Applied Superconductivity,* vol. 23, Jun 2013.

[125] M. I. Faley*, et al.*, "Magnetoencephalography using a multilayer high-T-c DC SQUID magnetometer," in *Superconductivity Centennial Conference 2011*. vol. 36, P. H. Kes and H. Rogalla, Eds., ed, 2012, pp. 66-71.

[126] H. Richter*, et al.*, "Magnetorelaxometry for localization and quantification of magnetic nanoparticles for thermal ablation studies," *Physics in Medicine and Biology,* vol. 55, p. 623, 2010.

[127] F. Wiekhorst*, et al.*, "Quantification of magnetic nanoparticle concentration in pig lung tissue after magnetic aerosol drug targeting by magnetorelaxometry," in *4th European Conference of the International Federation for Medical and Biological Engineering*. vol. 22, J. Sloten*, et al.*, Eds., ed: Springer Berlin Heidelberg, 2009, pp. 2326-2329.

[128] Y. R. Chemla*, et al.*, "Ultrasensitive magnetic biosensor for homogeneous immunoassay," *Proc Natl Acad Sci U S A,* vol. 97, pp. 14268-72, 2000.

[129] J. Lange*, et al.*, "Magnetorelaxometry—a new binding specific detection method based on magnetic nanoparticles," *Journal of Magnetism and Magnetic Materials,* vol. 252, pp. 381-383, 2002.

[130] Q. A. Pankhurst, J. Connolly, S. K. Jones, and J. Dobson, "Applications of magnetic nanoparticles in biomedicine," *Journal of Physics D: Applied Physics,* vol. 36, p. R167, 2003.